Research supported by the
National Oceanic and Atmospheric Administration
through TOGA/COARE Grant NA37RJ0202.

THE BAROTROPIC RESPONSE OF THE GLOBAL ATMOSPHERE TO LARGE-SCALE TROPICAL CONVECTIVE FORCING

by

Katherine A. Harris

Wayne Schubert, PI

Colorado
State
University

LIBRARIES
FEB 22 1999
COLORADO STATE UNIVERSITY

DEPARTMENT OF ATMOSPHERIC SCIENCE

PAPER NO. 674

THE BAROTROPIC RESPONSE OF THE GLOBAL ATMOSPHERE TO LARGE-SCALE TROPICAL CONVECTIVE FORCING

by Katherine A. Harris

Department of Atmospheric Science
Colorado State University
Fort Collins, CO 80523

Spring 1999

Atmospheric Science Paper No. 674

U18401 6511221

71 88 COL 1919
XL1
03/99

QC
852
.C6
no. 674
ATMOS

ABSTRACT

THE BAROTROPIC RESPONSE OF THE GLOBAL ATMOSPHERE TO LARGE-SCALE TROPICAL CONVECTIVE FORCING

A nonlinear shallow water model on the sphere is used to study the effect of large-scale tropical convective forcing on the response of the global circulation. Both the spatial and temporal characteristics of the forcing are found to significantly affect the production of tropical and extratropical circulation anomalies.

The horizontal shape and location of the convective forcing determines the strength, stability, and symmetry of the upper tropospheric response, the proportion of energy transferred into westward- and eastward-dispersing Rossby modes, and the exact direction of energy propagation. Together, these effects produce teleconnection patterns similar to those observed in the atmosphere. The strongest eastward teleconnection patterns are produced when the convective forcing is meridionally elongated and/or centered off of the Equator.

The timescale of the convective forcing determines the distribution of energy into Rossby, Kelvin, and gravity-inertia waves through a filtering on the wave spectrum. An analytical solution to the divergent barotropic vorticity equation is derived to highlight this timescale filter. When the forcing timescale is long, only the longest Rossby waves, with westward group velocities, can be excited at large amplitudes. As the timescale decreases, both the shorter Rossby waves, which have eastward group velocities, and the long gravity waves can be excited. The complete response of a stratified atmosphere is then shown to depend not only on the horizontal shape and timescale of the forcing, but also on its vertical structure.

Lower tropospheric convective forcing excites a much more vigorous response in the circulation than does upper tropospheric forcing. Strong cyclonic vortices, which can be likened to tropical cyclones, are generated by the unstable breakdown of the flow in the lower troposphere. The initiation locations and the direction of propagation of these vortices are determined by the horizontal shape and orientation of the convective forcing, through differences in Rossby wave energy dispersion. This reasoning provides a simple explanation for observations that tropical cyclones which form in the Western North Pacific during a "reverse monsoon trough" episode tend to track to the north or northeast (Lander 1996), as opposed to the more climatologically favored northwestward tracks of most Western North Pacific tropical storms.

Katherine A. Harris
Department of Atmospheric Science
Colorado State University
Fort Collins, Colorado 80523-1371
Spring 1999

ACKNOWLEDGEMENTS

I extend my deepest thanks to my advisor, Dr. Wayne Schubert, who has been the true inspiration and the motivation for this work. His patience, positive outlook, and his immense knowledge of the atmospheric sciences have provided me with the highest quality of education.

I would also like to thank my committee members, Dr. David Randall and Dr. Gerald Taylor, as well as the members of Dr. Schubert's research group, for their discussions and advice. I would especially like to thank Jim Kossin and Paul Ciesielski for patiently answering my many questions.

I also express my thanks and appreciation to Dr. James Hack and the National Center for Atmospheric Research for the use of the global spectral shallow water model. In addition, I would like to thank Dr. Rosana Nieto Ferreira for allowing me to use the version of the model which she revised for her Ph.D. work in this department. Rosana's own research also provided me with much inspiration.

This research is supported by the National Oceanic and Atmsospheric Administration through TOGA COARE Grant NA37RJ0202.

DEDICATION

To the continued success of women in the field of atmospheric science.

CONTENTS

Appendix

FIGURES

Chapter 1

INTRODUCTION

Observational studies of the tropical and extratropical atmosphere illustrate distinct correlations between tropical deep convection and the extratropical circulation. These "teleconnection" patterns were first reported to exist on interannual timescales by Wallace and Gutzler (1981) and Horel and Wallace (1981), in relation to the El Niño-Southern Oscillation cycle. More recent studies report additional correlations on shorter timescales, from submonthly (6–30 days) to intraseasonal (30–70 days) (Knutson and Weickmann 1987; Kiladis and Weickmann 1992; Kiladis et al. 1994; Tyrrell et al. 1996; Kiladis and Weickmann 1997). Teleconnections are observed globally in atmospheric phenomena such as the Madden-Julian Oscillation (MJO), the summer and winter monsoons, and large bursts of intertropical convergence zone (ITCZ) convection, which can be linked to tropical cyclogenesis.

A vast body of theoretical knowledge exists on the interactions between tropical convection and the extratropical circulation (e.g., Gill 1980; Lim and Chang 1983; Sardeshmukh and Hoskins 1988; Zhang and Webster 1989). Much of our present understanding of tropical-extratropical interactions involves the effect of the background flow on equatorial wave dispersion from tropical convective regions. For example, Zhang and Webster (1989) demonstrated that tropical-extratropical interactions via equatorial Rossby wave dispersion are much stronger in regions of equatorial westerlies than easterlies. Other studies have stressed the importance of the zonal and meridional shear of the zonal wind (Webster and Chang 1988) and the absolute vorticity gradient (Sardeshmukh and Hoskins 1988).

As our understanding of the effect of the background wind field on equatorial wave dispersion grows, more links between tropical convection and the extratropical circulation are understood. However, vital dynamical information is still missing. We are not yet able to predict the far-field effects of a specific convective episode, nor do we understand in detail why convection on different timescales produces different atmospheric responses. In this study, we seek to add another piece to this puzzle by investigating the effects of the horizontal and temporal distribution of tropical convection on the extratropical circulation. Specifically, we are interested in how the shape, size, and timescale of large-scale tropical convection affects the response of the extratropical circulation. A majority of previous modeling studies have concentrated on stationary convective regions of one specific size and shape, on one specific timescale, with varying background flows. In this study, we seek to illustrate and understand the wide variety of circulation patterns which can evolve solely in response to the varying spatial and temporal characteristics of tropical convection.

A nonlinear global shallow water model is used to simulate the effects of tropical convection on the circulation of the atmosphere. This method of investigation into the dynamics of tropical-extratropical teleconnections, although somewhat simplistic, has been used extensively in the past with great success (e.g., Gill 1980; Silva Dias et al. 1983; Webster and Chang 1988). In addition, to assist in the interpretation of the model results, an analytical solution to a simplified, nondivergent version of the model equations is derived. The insight gained through this method sheds new light on the divergent barotropic simulations. The relevance of these results to tropical-extratropical interactions in the MJO, the ITCZ, and for East Pacific-Atlantic teleconnections will be discussed.

As an extension to the discussion of convective shapes and their relation to the extratropical circulation, we consider the possibility of the barotropic instability of the ITCZ region. Ferreira and Schubert (1997) demonstrated through a shallow water model analysis that a simulated lower tropospheric ITCZ can break down into individual tropical cyclone-like disturbances through the barotropic instability mechanism. Here we extend this prior study to include upper tropospheric simulations, and discuss the relevance of these simulations to potential vorticity mixing and the relative dynamical activity of the lower and upper troposphere.

We then investigate whether the orientation of a localized ITCZ, in the form of off-equatorial monsoon convection, can affect the tracks of tropical cyclones which are created through the breakdown of the ITCZ. These experiments are motivated by Lander's (1996) observations that tropical cyclones in the Western North Pacific preferentially follow northward and S-shaped tracks during episodes of the "reverse monsoon trough," when the trough is oriented from southwest to northeast. We propose that this observation can be explained through the barotropic dynamics of the shallow water model.

The remainder of this paper is organized as follows: in Chapter 2, a literature review on tropical-extratropical interactions is presented. Chapter 3 contains the shallow water model equations, the convective forcing scheme, the model spectral transform process, and a discussion of the semi-implicit time differencing scheme. Results from the shallow water model simulations are presented in Chapters 4–6: Chapter 4 contains the shape, location, and orientation experiments, Chapter 5 the timescale experiments, and Chapter 6 the barotropic instability experiments. Finally, a summary and conclusions are presented in Chapter 7.

Chapter 2

LITERATURE REVIEW

This chapter will provide a general background on the observed links between tropical convection and the extratropical circulation, as well as a discussion of the proposed theories for these correlations. Much of the discussion involves the effect of the background wind field on the production of extratropical circulation anomalies. Although most of the shallow water model simulations presented in this study are initialized with a resting basic state, it is important to understand the effects of including more realistic background winds. The conclusions drawn in other studies can then be used in the interpretation of the shallow water model results.

2.1 Observations

Bjerknes (1969) was the first to document that the tropical ocean-atmosphere system is related to global atmospheric circulation fields through the El Niño-Southern Oscillation (ENSO) cycle. He determined that changes in global sea-level pressure fields can be interpreted through changes in tropical ocean temperatures, rainfall, and surface winds. A number of later observational papers documented that these atmospheric changes occur in the upper troposphere as well as at the surface (e.g., Horel and Wallace 1981; Wallace and Gutzler 1981), producing wavelike patterns in the 500-mb geopotential height field. An example of such a "teleconnection" pattern is the Pacific/North American (PNA) pattern designated by Wallace and Gutzler (1981), which extends from the tropical Pacific over North America.

As upper tropospheric datasets have become more complete, with the addition of satellite-derived radiation fields, detailed convection-circulation correlations on many different timescales have been uncovered. On very long timescales, such as are associated with ENSO, stationary wavetrains such as the PNA pattern emerge. On intermediate timescales, e.g., those of an intraseasonal oscillation (30–70 days), extratropical circulation patterns tend to show low zonal wavenumber (0–2) north-south dipole structures (Kiladis and Weickmann 1992; Kiladis et al. 1994). On short timescales (6–30 days), tropical convection is generally linked to east-west wavetrains of zonal wavenumber 5–6 (Kiladis et al. 1994; Kiladis and Weickmann 1997).

It is well-established in the literature that Rossby wave dispersion away from a large-scale convective heat source provides one possible explanation for the observed correlations between tropical convection and the extratropical circulation. Certainly the PNA pattern and other long-timescale teleconnection patterns described by Wallace and Gutzler (1981) resemble the Rossby wave circulation patterns produced when a simple numerical model is forced by a stationary heat source (e.g., Lim and Chang 1983; Lau and Lim 1984). Similar Rossby wave-like structures have also been observed on shorter timescales, developing progressively eastward from tropical convective events in both the Northern and Southern Hemispheres (Nitta 1987; Davidson and Hendon 1989; Ambrizzi and Hoskins 1995; Tyrrell et al. 1996).

The specific circulation patterns produced by deep tropical convection depend not only on the timescale of the convection, but also on its location within the tropics. This is especially true for shorter timescale convection, in the submonthly (6–30 day) range. Kiladis and Weickmann (1997) document these correlations in many regions of the tropics, and determine that the relationship between tropical convection and the extratropical circulation depends highly on both the longitude and latitude of the convection. For example, when convection is confined to the longitudes of the Western Pacific, the corresponding circulation patterns resemble the fields produced by Rossby wave dispersion from a tropical heat source, with twin anticyclonic circulations straddling the Equator. In the Eastern Pacific, however, tropical convection is more likely to be located on the eastern side of an upper-level trough, as part of an equatorward-propagating wavetrain (Kiladis 1998). Thus similarly-sized convection in these two locations may be associated with entirely different upper tropospheric circulation patterns.

The effect of the location of convection on its correlation with the circulation is modulated further by the season of the year. Since the sign, strength, and shear of the basic state wind change with the season, tropical convection which occurs in a certain location will produce different extratropical circulation signals in different seasons. For example, in the Western Pacific, convection tends to produce a stronger response in the winter hemisphere during solstitial months, whereas the response is fairly symmetric between hemispheres during equinoctal months. The season of the year also determines the strength and location of the climatological ITCZ, which determines the latitude at which the bulk of the tropical convection will occur. This will also modulate the extratropical response.

In summary, observations of the tropical and extratropical atmosphere show that the specific circulation patterns associated with tropical convection depend on the timescale of the convection, its location, both in longitude and latitude, and the season of the year, which determines the background wind field in which the tropical convection is embedded.

2.2 Theory

The observed Rossby wave-like structure of large-scale teleconnection patterns in the atmosphere led researchers to investigate the possibility that these fields could be produced by simple Rossby wave dispersion away from a region of tropical heating. Lim and Chang (1983) and Lau and Lim (1984), among others, showed that long-timescale teleconnection patterns similar to those identified by Wallace and Gutzler (1981) could be produced by tropical heating in a numerical model. The production of radiating Rossby modes was shown to be dependent, however, on the presence of westerly winds in the region of the tropical heating. In easterlies, Rossby modes appeared to be evanescent.

If this were true, then tropical convective forcing in upper tropospheric easterlies could never produce a Rossby wave signal which radiates outward to the extratropics. Significant circulation patterns associated with tropical convection are observed, however, in the Northern Hemisphere summer, when the tropics are filled with upper-level easterlies. To explain this discrepency, Sardeshmukh and Hoskins (1988) showed that radiating Rossby modes can in fact be forced in mean easterlies, through the creation of a "Rossby wave source." A region of deep convective heating produces a divergent outflow in the upper troposphere, which advects the basic state absolute vorticity so as to create a source of Rossby waves far removed from the actual tropical convection. If the convection is located in a region of upper-tropospheric mean easterlies, the Rossby wave source can produce a nonlocal source of Rossby waves outside these easterlies, which can then excite a radiating Rossby wave response which disperses energy outward into the extratropics. This mechanism also explains the observations that extratropical circulation signals associated with tropical convection are generally stronger in the winter hemisphere. Since the meridional absolute vorticity gradient is generally stronger in the winter hemisphere, a large Rossby wave source can be produced there.

Zhang and Webster (1989) theoretically analyzed the linearized shallow water equations to determine the effect of the zonal wind on the horizontal structure of equatorially-trapped waves. Rossby wave structures were found to change significantly with the sign and shear of the zonal flow, such that they are able to extend farther latitudinally in basic state westerlies than easterlies. In a geostrophic westerly flow, the potential vorticity gradient increases more strongly toward the poles than in geostrophic easterlies. Since the PV gradient is the restoring force for Rossby waves, and this gradient falls off with latitude more slowly in westerlies, Rossby waves are less "trapped" in westerlies than in easterlies. Westerly shear also enhances this "β-effect," so that Rossby waves are even less trapped in westerly shear. This reasoning assists in explaining the observed correlation between tropical convection and the extratropical circulation in the Eastern Pacific, where it appears that the extratropical circulation may sometimes force tropical convection (Kiladis and Weickmann 1997). When westerlies extend from the Equator into higher latitudes, as is observed in the Eastern Pacific during Northern Hemisphere winter and spring, interaction between the tropics and extratropics can occur more readily. Thus equatorward-propagating wavetrains which intrude into the tropics and trigger tropical convection are more likely to exist in the Eastern Pacific than, for example, the Western Pacific, where the background winds are generally easterly.

One shortcoming in the pure Rossby wave dispersion hypothesis is that the location and shape of extratropical teleconnection patterns can sometimes remain constant regardless of the actual location of tropical convection (Lau and Phillips 1986). This is especially true on timescales longer than 30 days. Webster and Chang (1988) proposed a mechanism to explain this observation: wave energy produced by tropical convection can accumulate in regions where $\partial u/\partial x$ is negative, i.e., regions of negative longitudinal stretch or convergence of the zonal wind. These same longitudinal regions are also areas of wave energy emanation into higher latitudes, by Rossby wave dispersion. Webster and Chang thus provide a mechanism by which the insensitivity of long timescale teleconnection patterns to the location of tropical convection can be explained, while retaining the Rossby wave dispersion hypothesis.

Simmons et al. (1983) proposed an entirely different mechanism by which atmospheric teleconnection patterns can be produced. Numerical model simulations showed that the Northern Hemisphere wintertime 300-mb flow could become barotropically unstable, producing height patterns similar to the PNA and "East Atlantic" patterns discussed by Wallace and Gutzler (1981). This midlatitude instability has a period of approximately 50 days. This mechanism for the production of teleconnection patterns is thus possible

Chapter 3

THE SHALLOW WATER MODEL

3.1 Model equations

In this study, a global nonlinear spectral shallow water model is used to simulate the atmospheric response to large-scale tropical convection. The equations of the model are based on the fully nonlinear shallow water equations, given here in rotational form:

$$\frac{\partial u}{\partial t} - \eta v + \frac{\partial\left[gh + \frac{1}{2}(u^2+v^2)\right]}{a\cos\phi\partial\lambda} = 0, \tag{3.1}$$

$$\frac{\partial v}{\partial t} + \eta u + \frac{\partial\left[gh + \frac{1}{2}(u^2+v^2)\right]}{a\partial\phi} = 0, \tag{3.2}$$

$$\frac{\partial h}{\partial t} + \frac{\partial(hu)}{a\cos\phi\partial\lambda} + \frac{\partial(hv\cos\phi)}{a\cos\phi\partial\phi} = Q, \tag{3.3}$$

where the independent variables are longitude, latitude, and time (λ, ϕ, t), a is the radius of the Earth, the velocity components in the eastward and northward directions are u and v, respectively, and Q is a mass source or sink. The total depth of the fluid is given by $h = H + h'$, where H is the constant global mean fluid depth and h' is the deviation from H. The absolute vorticity, η, is defined as:

$$\eta = 2\Omega\sin\phi + \frac{\partial v}{a\cos\phi\partial\lambda} - \frac{\partial(u\cos\phi)}{a\cos\phi\partial\phi}. \tag{3.4}$$

Model integration via the spectral transform method (see Section 3.3) is simplified when the above equations are combined to form the vorticity-divergence set of the shallow water equations:

$$\frac{\partial \eta}{\partial t} = -\frac{1}{a(1-\mu^2)}\frac{\partial}{\partial \lambda}(U\eta) - \frac{1}{a}\frac{\partial}{\partial \mu}(V\eta), \tag{3.5}$$

$$\frac{\partial \delta}{\partial t} = \frac{1}{a(1-\mu^2)}\frac{\partial}{\partial \lambda}(V\eta) - \frac{1}{a}\frac{\partial}{\partial \mu}(U\eta) - \nabla^2\left[gh + \frac{U^2+V^2}{2(1-\mu^2)}\right], \tag{3.6}$$

$$\frac{\partial h}{\partial t} = -\frac{1}{a(1-\mu^2)}\frac{\partial}{\partial \lambda}(Uh) - \frac{1}{a}\frac{\partial}{\partial \mu}(Vh) + Q, \tag{3.7}$$

where latitude is expressed in terms of $\mu = \sin\phi$, and U and V are given by $u\cos\phi$ and $v\cos\phi$, respectively. The absolute vorticity η and divergence δ are defined as:

$$\eta = 2\Omega\mu + \frac{1}{a(1-\mu^2)}\frac{\partial V}{\partial \lambda} - \frac{1}{a}\frac{\partial U}{\partial \mu}, \tag{3.8}$$

$$\delta = \frac{1}{a(1-\mu^2)}\frac{\partial U}{\partial \lambda} + \frac{1}{a}\frac{\partial V}{\partial \mu}. \tag{3.9}$$

In the context of linear dynamics, the shallow water equations can be thought of as an infinitely large set of equations, each set having a different global mean fluid depth H (also called an "equivalent depth"). Each vertical mode in the continuously stratified atmosphere corresponds to one set of the shallow water equations with a particular equivalent depth. By summing the solutions of the shallow water equations for every equivalent depth, the solution to the continuously stratified equations can be reconstructed.

In the simulations to be presented in this study, an equivalent depth that corresponds to the first internal baroclinic mode of the continuously stratified equations is chosen. This mode is single-signed from the surface upward through the majority of the troposphere, representing the deep positive heating profile produced by tropical convection in the Warm Pool. There is a reveral of sign at approximately 250 mb, above which detrainment and evaporative cooling occur. Observational evidence for a first baroclinic mode structure to Western Pacific convective disturbances is presented by Kiladis and Weickmann (1997). (The second and higher baroclinic modes are shown to be potentially significant by Wheeler and Kiladis (1999). We choose here to concentrate on the first baroclinic mode exclusively.) Following the work of Fulton and Schubert (1985), the global mean shallow water fluid depth is chosen to be 608 m, corresponding to a gravity wave phase speed $\sqrt{gH}$ of 77.2 m s^{-1}

and a Rossby deformation radius $\epsilon^{-\frac{1}{4}}a$ of 1837 km, where $\epsilon = 4\Omega^2 a^2/(gH) \approx 145$ is Lamb's parameter.

All simulations are initialized with a basic state at rest. Although this simplification is unrealistic in terms of the real atmosphere, it allows the basic physics of the model to be understood more clearly.

3.2 Convective forcing

Convection is simulated in the shallow water model by a mass source (upper tropospheric simulations) or a mass sink (lower tropospheric simulations) in the mass continuity equation (3.3). This mass source (sink) is intended to represent the deposition (removal) of mass in the upper (lower) troposphere by deep cumulus convection, i.e., the upward mass transport produced by convection.

In the simulations to be presented here, the mass source/sink $Q(\lambda, \mu, t)$ is divided into separable temporal and spatial functions:

$$Q(\lambda, \mu, t) = \tfrac{1}{2}\alpha^3 t^2 e^{-\alpha t}\tilde{h}(\lambda, \mu), \tag{3.10}$$

where the constant α has dimensions of inverse time, and the function $\tilde{h}(\lambda, \mu)$ has dimensions of length. The parameter α determines the temporal distribution of the forcing. Since

$$\int_0^\infty \tfrac{1}{2}\alpha^3 t^2 e^{-\alpha t} dt = 1, \tag{3.11}$$

regardless of the value of α, this temporal forcing adds or removes the same amount of mass from the model for any α. Examples of this temporal distribution are given in Figure 3.1 for $\alpha = 3.22$, 1.46, and 0.91 days^{-1}, or approximate forcing timescales of 3, 6, and 9 days, respectively. In the model, the temporal forcing is set to zero when its magnitude drops below a designated threshold value, so that the forcing ends at a finite time. This threshold value is depicted by the horizontal line near the bottom of Figure 3.1.

The spatial contribution to the forcing, $\tilde{h}(\lambda, \mu)$, represents an idealized distribution of the fluid. If no other physical processes are allowed to act on the fluid other than the

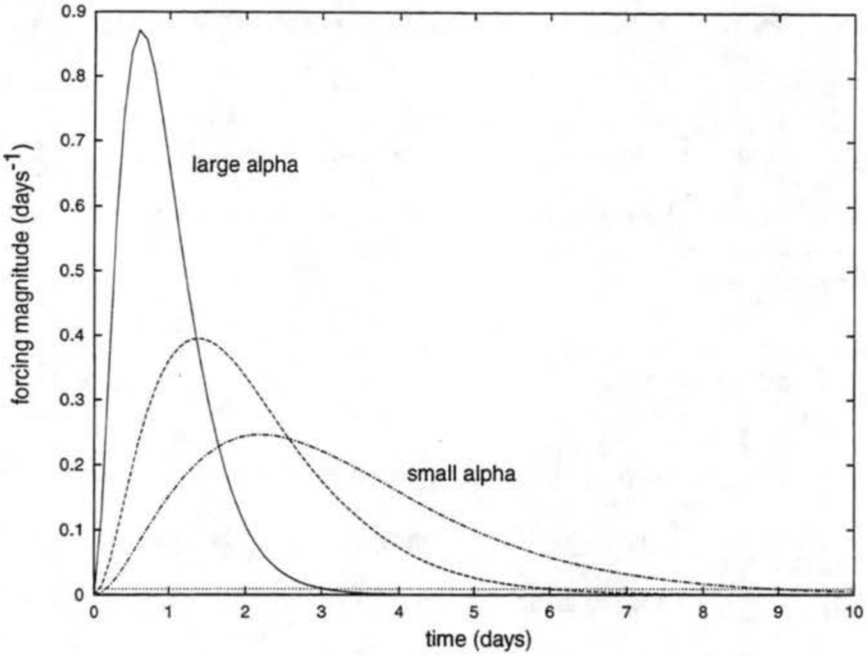

Figure 3.1: Time-dependence of forcing for 3-, 6-, and 9-day forcing, corresponding to $\alpha =$ 3.22, 1.46, and 0.91 days^{-1}, respectively.

mass source/sink, the fluid will have a distribution given by $\tilde{h}(\lambda, \mu)$ at time infinity. In the absence of any restoring forces, equation (3.3) simplifies to:

$$\frac{\partial h}{\partial t} = \tfrac{1}{2}\alpha^3 t^2 e^{-\alpha t}\tilde{h}(\lambda, \mu). \tag{3.12}$$

When this equation is integrated in time from 0 to ∞, assuming that the fluid is initially undisturbed so that $h(\lambda, \mu, 0) = 0$, it becomes:

$$h(\lambda, \mu, \infty) = \tilde{h}(\lambda, \mu). \tag{3.13}$$

Thus the forcing function $\tilde{h}(\lambda, \mu)$ pushes the fluid toward this idealized end state.

The function $\tilde{h}(\lambda, \mu)$ itself is constructed by multiplying a physical space shape function, $F(\lambda, \mu)$, by a constant, h_0:

$$\tilde{h}(\lambda, \mu) = h_0 F(\lambda, \mu). \tag{3.14}$$

The physical space shape function is of the form:

$$F(\lambda, \mu) = F[r(\lambda, \phi), \gamma], \tag{3.15}$$

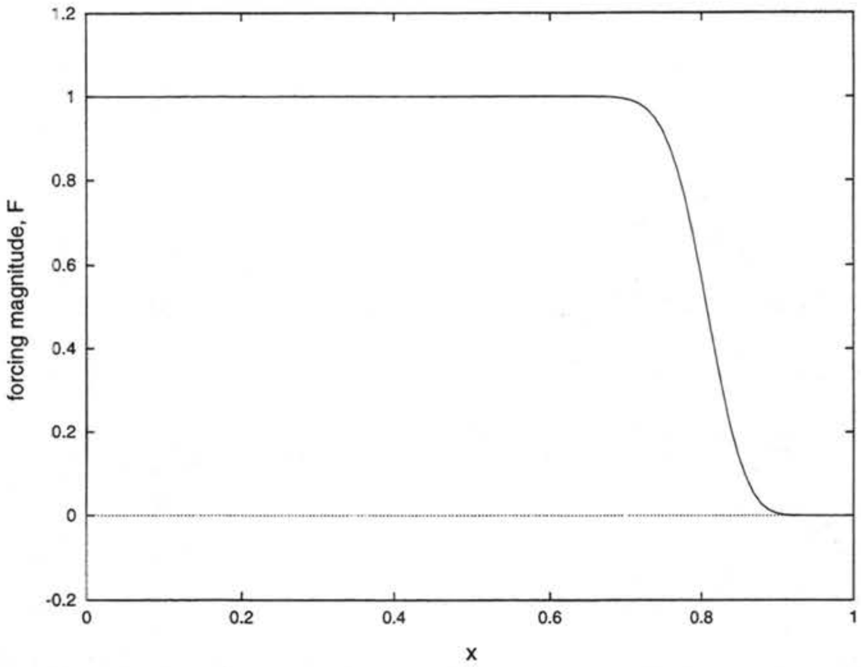

Figure 3.2: The spatial forcing function $F(x, \gamma)$, where x is the radial distance from the center of the forcing and $\gamma = 100$.

where

$$F(x,\gamma) = \begin{cases} 1, & \text{for } x = 0 \\ 1 - \exp\left[-\frac{\gamma}{x}\exp\left(\frac{1}{x-1}\right)\right], & \text{for } 0 < x < 1 \\ 0, & \text{otherwise,} \end{cases} \tag{3.16}$$

and

$$r(\lambda,\phi) = \left[\frac{(\lambda\cos\phi)^2}{b^2} + \frac{(\phi-\phi_0)^2}{c^2}\right]^{\frac{1}{2}}, \tag{3.17}$$

(after Ferreira et al. 1996). The zonal and meridional extent of the forcing are determined by the constants b and c, and the central latitude of the forcing is given by ϕ_0. The constant γ determines the steepness of the dropoff of the function at the edges of the forcing region. An example of this function for $\gamma = 100$ and circular mass forcing is given in Figure 3.2. In the shallow water model simulations to be presented, the approximate width of the forcing given in the text is designated as the width along $F(\lambda, \mu) > 0.5$.

The constant h_0 in (3.14) is calculated by analogy to the stratified atmosphere. The equation for the pseudo-density, σ, in isentropic coordinates in a continuously stratified fluid is:

$$\frac{1}{\sigma}\left[\frac{\partial\sigma}{\partial t}+\frac{\partial(\sigma u)}{a\cos\phi\partial\lambda}+\frac{\partial(\sigma v\cos\phi)}{a\cos\phi\partial\phi}\right]=-\frac{\partial(\sigma\dot{\theta})}{\sigma\partial\theta}, \tag{3.18}$$

where

$$\sigma=-\frac{1}{g}\frac{\partial p}{\partial\theta}, \tag{3.19}$$

and $\dot{\theta}$ is the heating rate. The analogous equation in the shallow water case is the mass continuity equation:

$$\frac{1}{H}\left[\frac{\partial h}{\partial t}+\frac{\partial(hu)}{a\cos\phi\partial\lambda}+\frac{\partial(hv\cos\phi)}{a\cos\phi\partial\phi}\right]=\frac{Q}{H}. \tag{3.20}$$

Assuming that

$$\frac{\partial(\sigma\dot{\theta})}{\sigma\partial\theta}\approx\frac{\partial\dot{\theta}}{\partial\theta}, \tag{3.21}$$

the following analogy can be made between the right hand sides of the pseudo-density and continuity equations:

$$\left|\frac{\partial\dot{\theta}}{\partial\theta}\right|\approx\left|\frac{Q}{H}\right|. \tag{3.22}$$

Substituting in for $Q(\lambda,\mu,t)$ from (3.10) and (3.14), and integrating in time from 0 to the finite time limit of the forcing, t_e, we obtain:

$$\int_0^{t_e}\left|\frac{\partial\dot{\theta}}{\partial\theta}\right|dt\approx\int_0^{t_e}\tfrac{1}{2}\alpha^3t^2e^{-\alpha t}\left|\frac{h_0}{H}\right|F(\lambda,\mu)dt. \tag{3.23}$$

Approximating the time-independent $F(\lambda,\mu)$ as 1 inside the region of the mass source and 0 outside, and using (3.11), we determine the following relationship:

$$\left|\frac{\partial\dot{\theta}}{\partial\theta}\right|t_e\approx\left|\frac{h_0}{H}\right|. \tag{3.24}$$

To approximate a value for h_0, we take an average heating rate $\dot{\theta}$ of 12 K day^{-1} inside the forcing region. This value is approximated from the Q_1 data in Lin and Johnson (1996) in the TOGA-COARE (Tropical Ocean Global Atmosphere Coupled Ocean-Atmosphere Response Experiment) region during a 6-day convectively disturbed period, from 20–26 December 1992. This value also represents approximately twice the average peak Q_1 value in the Western Pacific (Yanai et al. 1976; Fulton and Schubert 1985). This heating is assumed to be a maximum in the midtroposphere, at approximately the 330 K level, and zero at the surface, at approximately 300 K. For a mean depth H of 608 m, and a total heating of 6 days, this gives a value for h_0 of approximately 1500 m. The dimensions of the convective region upon which this calculation is based are 15 degrees latitude by 15 degrees longitude; thus we use this value of h_0 in simulations with the same total convective area in the model. The values of h_0 for simulations of convective regions of other sizes and shapes are scaled accordingly such that the total amount of mass added or removed from the model is the same in each simulation. We believe that this is a reasonable assumption as well as a good way to normalize the simulations presented here.

In the shallow water model, the mass source forces the wind fields, but the wind fields do not feed back onto the mass source. In the real atmosphere, there is of course a two-way feedback between convection and circulation. Kiladis et al. (1994) show, however, that upper tropospheric circulation features in the 6-30 day band in the Western and Central Pacific are generally stronger and more statistically significant following tropical convection, rather than prior to it. Yanai et al. (1999) extend this conclusion to a 40-day period, as in the MJO, stating that in the Western Pacific, convection leads the upper-level circulation (the easterly zonal wind perturbation) by a quarter cycle. These results suggest that upper level circulation fields in the Western Pacific are primarily forced by convection, rather than the convection being forced by the circulation. This justifies the lack of feedback between the wind fields and the forcing in the shallow water model for at least the upper tropospheric simulations.

3.3 The spectral method

The model used is a T-106 spectral model. A spectral model expresses horizontal fields in terms of truncated series expansions of spherical harmonic functions. The model transforms variables between physical and spectral space each timestep, calculating nonlinear terms in physical space on the transform grid, while computing derivatives and stepping forward in time in spectral space. The T-106 model truncates the spherical harmonic expansions at both zonal and total (zonal plus meridional) wavenumber 106. This gives $(107)^2$ real degrees of freedom and therefore a horizontal resolution of approximately $[4\pi a^2/(107)^2]^{\frac{1}{2}} =$ 211 km.

To transform from physical to spectral space and back, the following transforms are used:

$$\psi_n^m(t) = \frac{1}{4\pi}\int_{-1}^{1}\int_{0}^{2\pi}\psi(\lambda,\mu,t)Y_n^{m*}(\lambda,\mu)d\lambda d\mu, \tag{3.25}$$

$$\psi(\lambda,\mu,t) = \sum_{m=-N}^{N}\sum_{n=|m|}^{N}\psi_n^m(t)P_n^m(\mu)e^{im\lambda}. \tag{3.26}$$

The indices m and n indicate the zonal and total wavenumbers, respectively, and N is the truncation limit of the model (in this case, 106). $Y_n^{m*}(\lambda,\mu)$ is the complex conjugate of a spherical harmonic function and $P_n^m(\mu)$ is an associated Legendre polynomial. In the discussions to follow, reference will also be made to the meridional nodal number, defined as the quantity $n-m$.

More information on the transform method can be found in Hack and Jakob (1992).

3.4 Semi-implicit time differencing

One of the global shallow water model options for time discretization is the leapfrog time differencing scheme. For the differential equation

$$\frac{d\psi}{dt} = F(\psi), \tag{3.27}$$

the leapfrog scheme is:

$$\psi^{(\tau+1)} = \psi^{(\tau-1)} + 2\Delta t F^{(\tau)}, \tag{3.28}$$

where ψ is any prognostic variable, Δt is the timestep, and F is a general tendency term. At time level τ, the value of ψ at the next time level $(\tau+1)$ is calculated by using the value of ψ at the previous time level $(\tau-1)$ and the tendency term calculated at the present time level.

The leapfrog scheme presented above is an example of an explicit scheme. In order for solutions under an explicit scheme to be stable (i.e., errors do not grow exponentially with time), the timestep must be short enough to resolve the shortest gravity wave oscillations. This timestep is given by the CFL (Courant-Fredericks-Lewy) criterion:

$$\Delta t < \frac{1}{\nu_N}, \tag{3.29}$$

where ν_N is the continuous solution frequency (i.e., no time differencing approximations) of the shortest gravity waves in the model. The continuous solution gravity wave frequency for any wavenumber n can be analytically determined from the linearized, nonrotating, spectrally represented shallow water equations:

$$\nu_n = \left[\frac{gHn(n+1)}{a^2}\right]^{\frac{1}{2}}, \tag{3.30}$$

where H is the mean depth of the fluid. When this formula is used with $n = N$, the frequency of the shortest gravity waves in the model, ν_N, can be calculated and then used to determine the maximum timestep in (3.29). For a T-106 model with a mean depth of 608m, this calculation gives a maximum timestep Δt of 12.9 minutes. The CFL criterion is thus a powerful constraint on the timestep in the model, which can make an explicit scheme computationally inefficient, especially for slowly-evolving processes.

An effective method to eliminate this short timestep dilemma is to use semi-implicit timestepping, which combines the explicit and implicit schemes. An implicit time differencing scheme is stable for any length timestep, so poses no CFL criterion for stability. An example of an implicit scheme for (3.27) is:

$$\psi^{(\tau+1)} = \psi^{(\tau-1)} + 2\Delta t F^{(\tau+1)}. \tag{3.31}$$

The time tendency term in this implicit scheme is evaluated at time level $(\tau + 1)$ instead of at time level τ, as in the explicit scheme. One drawback to the implicit scheme is that it may be difficult to disentangle the components of the time tendency term on the right hand side of the equation in order to group all terms evaluated at time level $(\tau + 1)$ on the left hand side.

The semi-implicit time scheme combines the explicit and implicit time schemes such that the CFL condition associated with the explicit scheme applies only to the slowly-evolving, advective components of the flow. The gravity wave terms are treated implicitly, so that there is no CFL restriction associated with these high-frequency oscillations. The semi-implicit time scheme can be illustrated as follows:

$$\psi^{(\tau+1)} = \psi^{(\tau-1)} + 2\Delta t N^{(\tau)} + 2\Delta t \left(\frac{G^{(\tau-1)} + G^{(\tau+1)}}{2} \right), \tag{3.32}$$

where N represents all the nonlinear tendency terms, and G represents the gravity wave tendency terms. The nonlinear terms are treated explicitly, at the present time level, whereas the gravity wave terms are treated implicitly, as an average of the tendency terms from the previous and the next time levels. The CFL timestep restriction in the semi-implicit scheme is much less severe than in the purely explicit scheme, since it is associated with the low frequency advective processes.

The maximum timestep for the semi-implicit scheme depends on the fastest flow speeds produced in a given simulation, instead of the gravity wave phase speed ($\sqrt{gH}$). A useful estimate is that (3.29) is modified to:

$$\Delta t < \left(\frac{\sqrt{gH}}{V_m} \right) \left(\frac{1}{\nu_N} \right), \tag{3.33}$$

where V_m is the maximum flow speed in the simulation. This timestep is small enough to resolve only the low-frequency oscillations, not the high-frequency gravity waves. For a T-106 model with a mean depth of 608 m and a maximum flow speed of 20 m s^{-1}, Δt must be less than 50 minutes. This is a much less severe restriction, giving a timestep approximately four times longer than in the purely explicit time scheme.

The semi-implicit scheme can be a very efficient method of timestepping the spectral shallow water model. However, gravity waves are no longer calculated exactly by the model, since the timestep allowed by the semi-implicit model is not short enough to resolve the highest frequency oscillations. One might wonder, then, how distorted these gravity waves become. To answer this question, the following relationship is derived from the linearized, nonrotating shallow water equations:

$$\frac{\hat{\nu}_n}{\nu_n} = \frac{\arctan(\nu_n \Delta t)}{\nu_n \Delta t}, \tag{3.34}$$

where $\hat{\nu}_n$ is the actual frequency of the time-differenced solution and ν_n is the continuous solution frequency. From this equation, it is apparent that the actual frequency of gravity wave oscillations of wavenumber n in a semi-implicit model will be less than or approximately equal to the true frequency calculated from the continuous solution to the shallow water equations. When $\nu_n \Delta t$ is small, (i.e., the true gravity wave frequency and/or the semi-implicit timestep is small), the ratio $\hat{\nu}_n/\nu_n$ will be close to 1. As $\nu_n \Delta t$ increases, the time-differenced frequency becomes a smaller percentage of the true frequency.

To illustrate this point more clearly, Figure 3.3 compares the continuous solution and semi-implicit frequencies in a wavenumber-frequency diagram. The straight line running from the lower left to the upper right corner of the diagram represents the continuous solution frequency as a function of wavenumber. The other curves are computed from (3.34) for the time-differenced frequency, $\hat{\nu}_n$. The curves are labeled in terms of $\nu_N \Delta t$, the Courant number. The Courant number represents how the timestep used in the semi-implicit scheme compares with the maximum timestep allowed in the explicit scheme. For example, a Courant number of 2 means that the semi-implicit timestep is twice the maximum timestep allowed by the explicit scheme. When the Courant number is small, only the frequencies of the shortest waves are affected by the semi-implicit scheme. As the Courant number increases, a larger portion of the wavenumber spectrum suffers from a reduction in gravity wave frequency, with the largest effects at high wavenumbers.

Figure 3.3 clearly illustrates why the semi-implicit time scheme is not suitable for use in shallow water simulations in which gravity waves play a significant role. Since the semi-implicit scheme was designed to allow a longer timestep to be taken than with the explicit scheme, it would make little sense to use a semi-implicit scheme with a Courant number less than 1. Courant numbers greater than 1, however, significantly distort the frequencies of gravity waves, especially the short waves. Thus in a simulation in which gravity

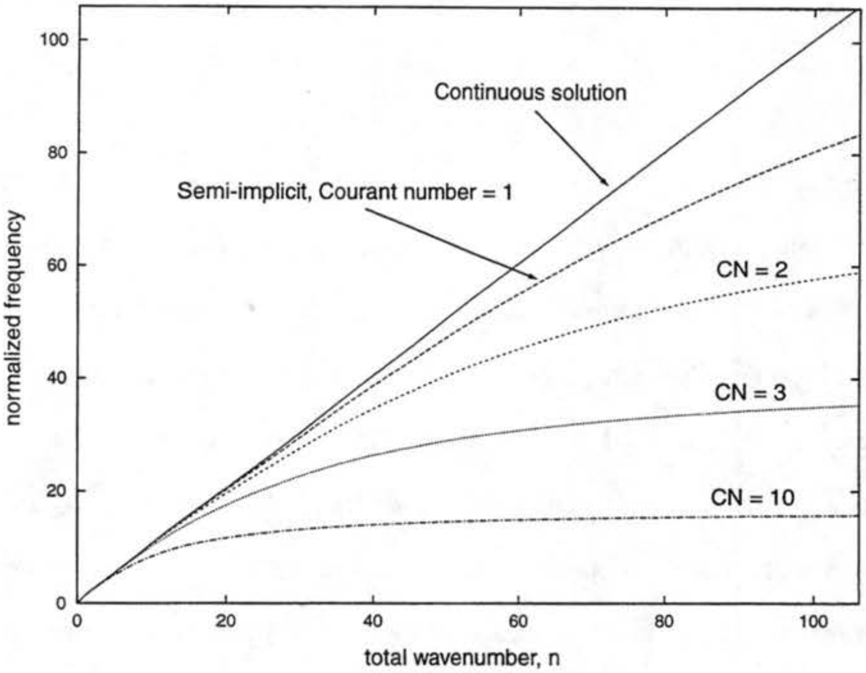

Figure 3.3: Continuous solution and semi-implicitly timestepped gravity wave frequencies as a function of total wavenumber, n. All frequencies are normalized by $\sqrt{gH}/a$. Semi-implicit curves are labeled in terms of the Courant number (CN).

wave motions are significant, the semi-implicit scheme can distort the results. In slowly-evolving flows, however, where gravity waves are insignificant, the semi-implicit scheme can significantly cut computational costs by increasing the timestep length.

In most of the shallow water model simulations described in this study, the forcing is prescribed on a long enough timescale that no significant gravity wave motions are excited. The timestep is chosen to be 40 minutes, or a Courant number of approximately 3. This reduces the computational time by a factor of 3 over explicit timestepping, and does not distort the results. Several simulations in Chapter 5, however, are forced on very short timescales, which allows the excitation of gravity waves. These simulations are timestepped explicitly, so that the gravity waves are treated accurately.

Chapter 4

SHAPE, LOCATION, AND ORIENTATION OF CONVECTIVE FORCING

Tropical deep convection occurs on a wide variety of spatial and temporal scales. Spatial organization ranges from individual clouds and storms to large-scale convective envelopes, for example, associated with the MJO or ITCZ convection. Temporal scales range from a few hours for an individual storm through several years for an El Niño-Southern Oscillation event. In this study, we seek to understand the dynamics which control the production of extratropical circulation signals by large-scale tropical convection. Specifically, we address how the physical shape and location of tropical disturbances, as well as their timescale, affect the response of the extratropical circulation. Most of the simulations described here are limited to large-scale, low frequency tropical convection, greater than 1000 km in horizontal dimension, on a timescale of three days or longer. The focus is therefore on the slower Rossby wave response of the atmosphere, not the faster gravity wave response. We seek to investigate the response of the atmosphere to large-scale, relatively low-frequency convective events such as the Madden-Julian Oscillation, monsoon convection, and ITCZ disturbances.

This chapter describes simulations in which the horizontal shape, location, and orientation of a stationary convective region are varied, while the timescale is held constant. Simulations in which the timescale of the forcing is varied are presented in Chapter 5.

4.1 Observations

Large-scale tropical convection is organized into a variety of horizontal shape and size distributions. In the Indian Ocean and Western Pacific Warm Pool, for example, convection associated with the MJO on a 5–7 day timescale can vary drastically in its horizontal distribution. Figures 4.1 and 4.2 are plots of the outgoing longwave radiation (OLR, a proxy for deep convection) in the Indian Ocean region from an MJO event in May 1995. On May 4, deep convection, here denoted by OLR values less than 200 W m^{-2}, is zonally elongated, extending approximately 30 degrees in longitude and 20 degrees in latitude. On May 7, convection becomes meridionally elongated, stretching 40 degrees in latitude and 25 degrees in longitude. Examples such as this occur rather frequently, i.e., in the MJO episodes of April and May 1986, January 1992, and December 1992.

In the Eastern Pacific basin, similar shape differences can occur. When the basin is relatively inactive, generally in the Northern Hemisphere winter, convection tends to organize in a zonal direction along the ITCZ (Figure 4.3). When convection flares up, typically in the Northern Hemisphere summer and autumn, the organization becomes more meridional (Figure 4.4).

In addition to these dramatic horizontal shape and size changes, the mean latitude of tropical convection can also change throughout the year. For example, the location of the mean ITCZ in the Western Pacific shifts from well north of the Equator during the Northern Hemisphere summer monsoon season (June–August) to south of the Equator during the winter monsoon season (December–February), passing across the Equator twice per year.

The model simulations presented in this chapter will provide a dynamical view of the different atmospheric responses produced by idealized tropical convection of these various spatial organizations.

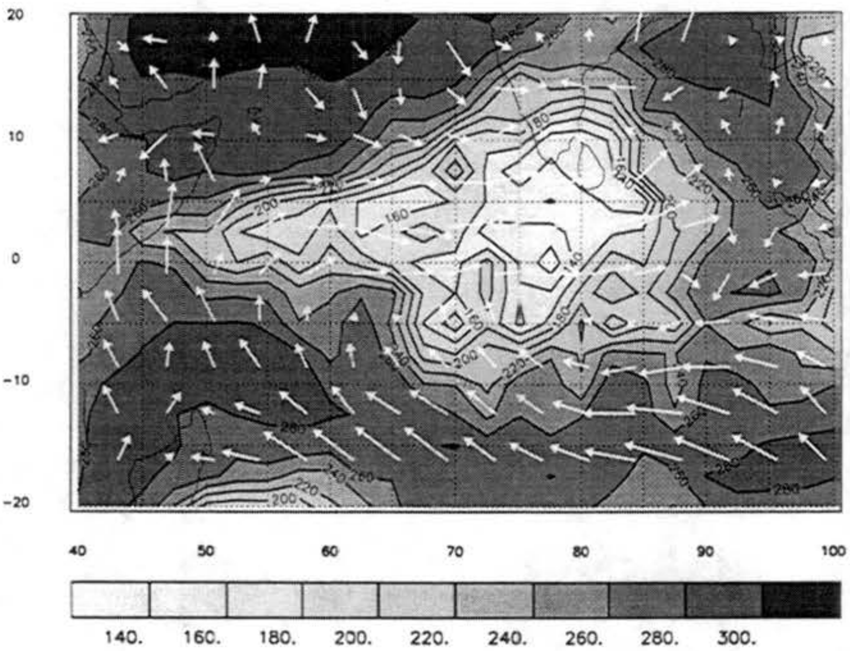

Figure 4.1: OLR (contours, Wm^{-2}) and 10 m winds (vectors) on 4 May 1995. Longitude in degrees E. (From Maria Flatau, Scripps Institute of Oceanography.)

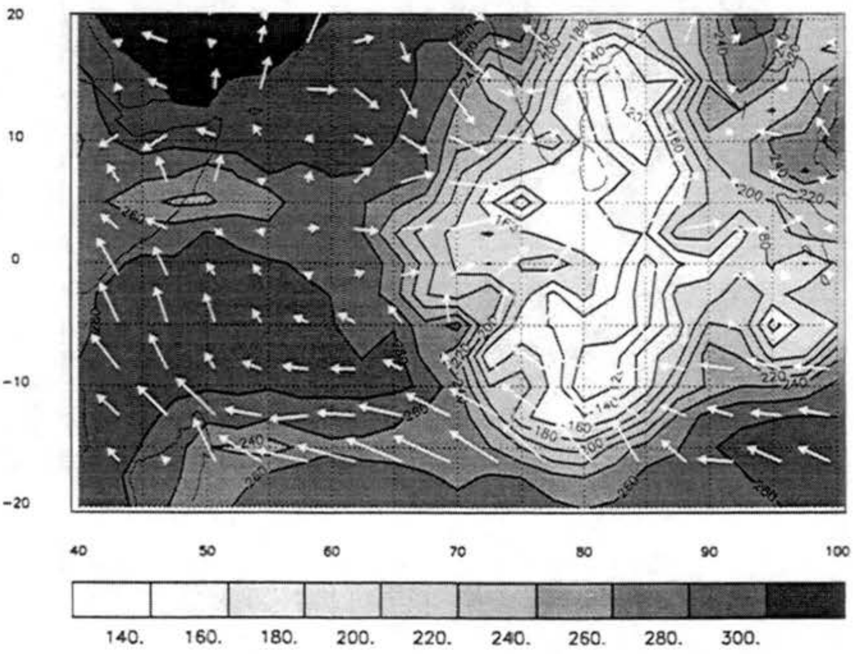

Figure 4.2: Same as Figure 4.1 but for 7 May 1995.

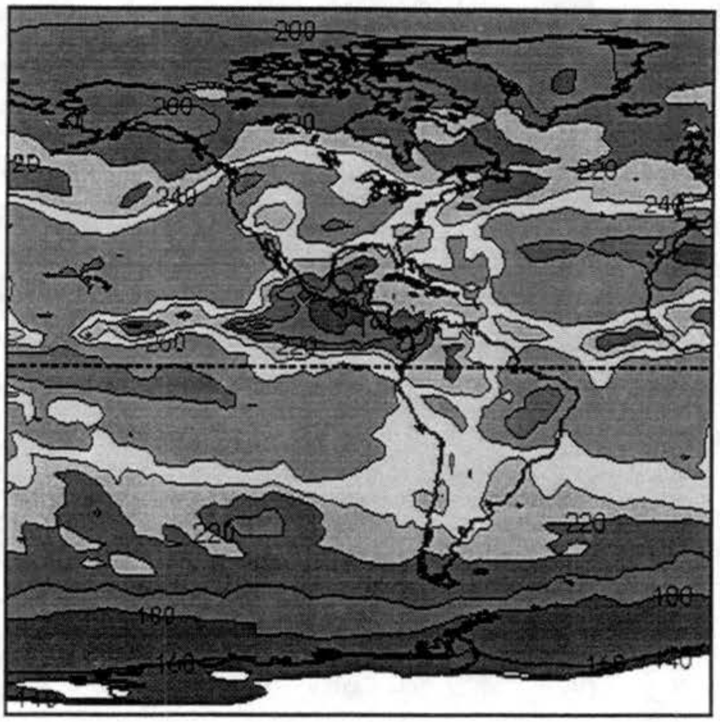

Figure 4.3: Seven-day averaged OLR from 31 August to 6 September 1998. OLR less than 220 Wm^{-2} denoted by darker gray shading. (From Climate Diagnostics Center.)

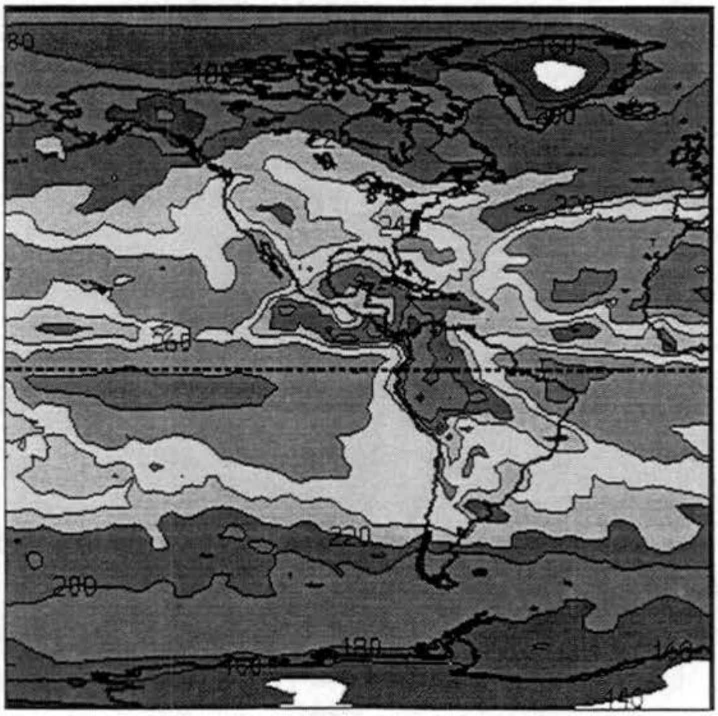

Figure 4.4: Same as Figure 4.3 but for 10–17 October 1998.

4.2 Circular forcing, upper troposphere

The shallow water model is used to illustrate the barotropic response of the atmospheric circulation to large-scale tropical convection. We begin by discussing the model results from a simple circular forcing simulation. When compared with observations, this simulation will provide justification for the validity of the model itself, as well as providing a "control run" with which to compare later simulations.

4.2.1 Model results

Experiment CIRC15 was run to determine the basic response of the shallow water model to equatorially symmetric forcing. The spatial component $\tilde{h}(\lambda, \mu)$ of the mass forcing $Q(\lambda, \mu, t)$ is positive, i.e., a mass source; thus this simulation represents the effects of convection on the upper troposphere. The numerical value of h_0 in (3.14) is 1500 m, representing a heating over the mass source region of approximately 12 K day^{-1} for a total of 6 days. The temporal distribution of the forcing is given by the middle curve in Figure 3.1, corresponding to $\alpha = 1.46$ days^{-1}. This forcing timescale is intended to represent the approximate amount of time a large-scale convective region remains stationary in an event such as the MJO. The physical shape of the mass source is circular, with half-widths b and c of 9.375 degrees, giving an approximate diameter of 15°. The mass source is centered on both the Equator and zero degrees relative longitude.

After two days of forcing, a response similar to the steady-state simulations of Gill (1980) emerges in the height and wind fields (Figure 4.5). Two symmetric anticyclonic Rossby wave circulations are produced, one to the north and one to the south of the forcing region. A Kelvin wave emerges to the east of the forcing, distinguished by its westerly zonal winds and positive height anomaly, both which decay exponentially away from the Equator. The Kelvin wave extends to the east of the forcing region farther than the Rossby wave extends to the west because the Kelvin wave propagation speed is faster.

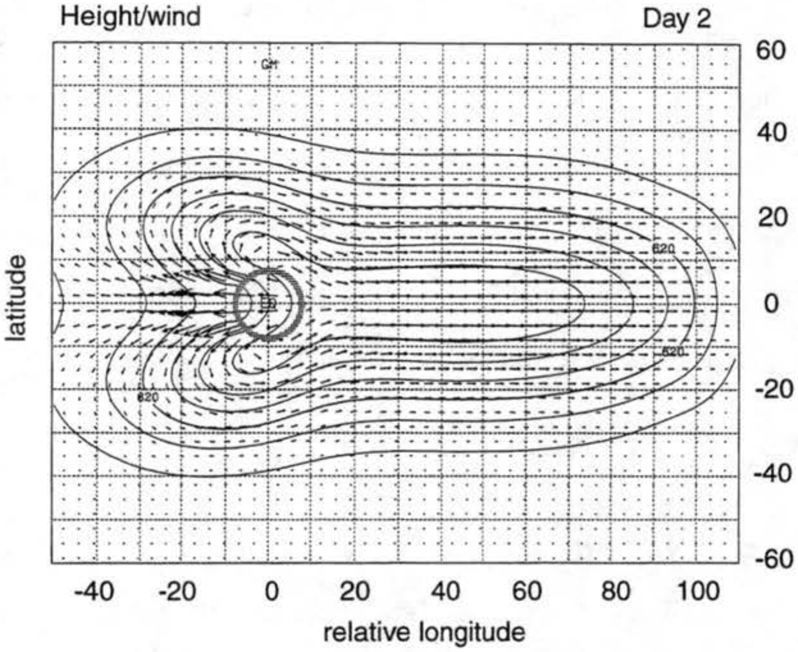

Figure 4.5: Height/wind field on Day 2 for CIRC15. Height field is contoured every 4 meters. Wind vectors are scaled so that a vector 10° in length represents a 10 m s^{-1} wind. The heavy circle represents the approximate size and location of the mass source. Scaling is the same for all other simulations unless otherwise noted.

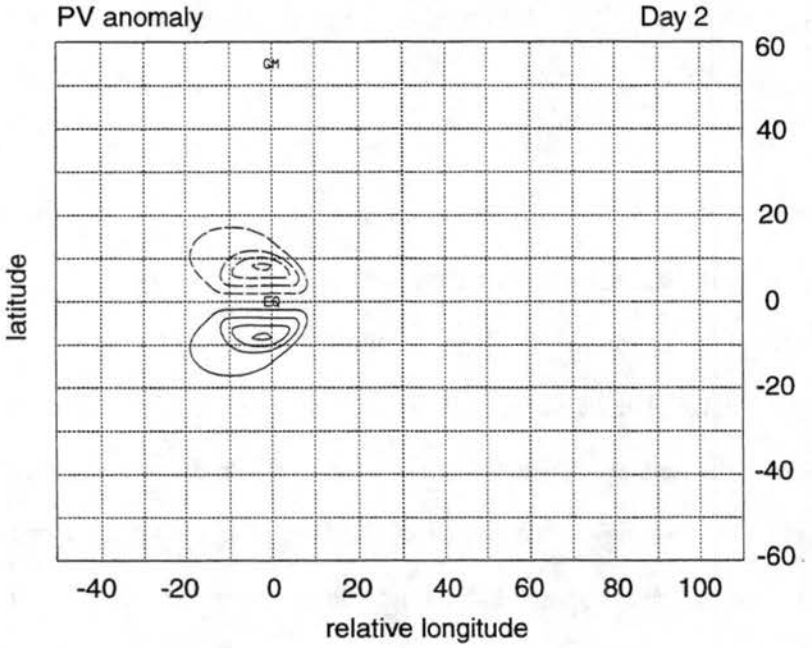

Figure 4.6: PV anomaly field on Day 2 for CIRC15. Contour interval is 4.0×10^{-6} s^{-1}. Dashed contours represent negative values. Zero contour lines are suppressed.

The potential vorticity (PV) contours are pushed poleward in the region of the mass source, signaling the creation of opposite-signed PV anomalies on either side of the Equator. This result can be interpreted directly from the PV conservation relation, derived from equations (3.1)–(3.3):

$$\frac{DP}{Dt} = -\frac{PQ}{h}, \tag{4.1}$$

where the potential vorticity, P, is given by:

$$P = \frac{\eta H}{h}. \tag{4.2}$$

Equation (4.1) states that the PV of a fluid parcel changes only when it is located in the region of the mass forcing Q. When Q is positive, signifying a mass source, DP/Dt will be negative in the Northern Hemisphere and positive in the Southern Hemisphere. This will induce a negative (positive) PV anomaly in the Northern (Southern) Hemisphere, which will push the PV contours away from the Equator. The PV anomaly plot on Day 2 (Figure 4.6) illustrates this result. Note also that the Kelvin wave is "invisible" in the PV anomaly field, i.e., it has no effect on the PV.

The maximum PV anomalies are produced in the most poleward extensions of the forcing region. Since DP/Dt depends not only on the magnitude of the mass source Q, but also on the value of the ambient potential vorticity P, the largest PV anomalies will be produced where the magnitude of the product PQ is the largest. In this resting basic state case, the magnitude of the ambient PV increases monotonically towards the poles. Initially, then, the largest PV anomalies are produced towards the northern and southern edges of the mass source region.

After six days of integration, evidence of Rossby wave propagation and dispersion is clearly seen in the height and wind fields (Figure 4.7). The anticyclonic cells from Day 2 have propagated westward, and new cyclonic and anticyclonic circulations now appear to their east. These new cells are a result of the eastward dispersion of short Rossby wave energy. The PV anomaly plot for Day 6 (Figure 4.8) illustrates the creation of opposite-signed anomalies to the east of the original PV anomalies from Day 2. The long waves to

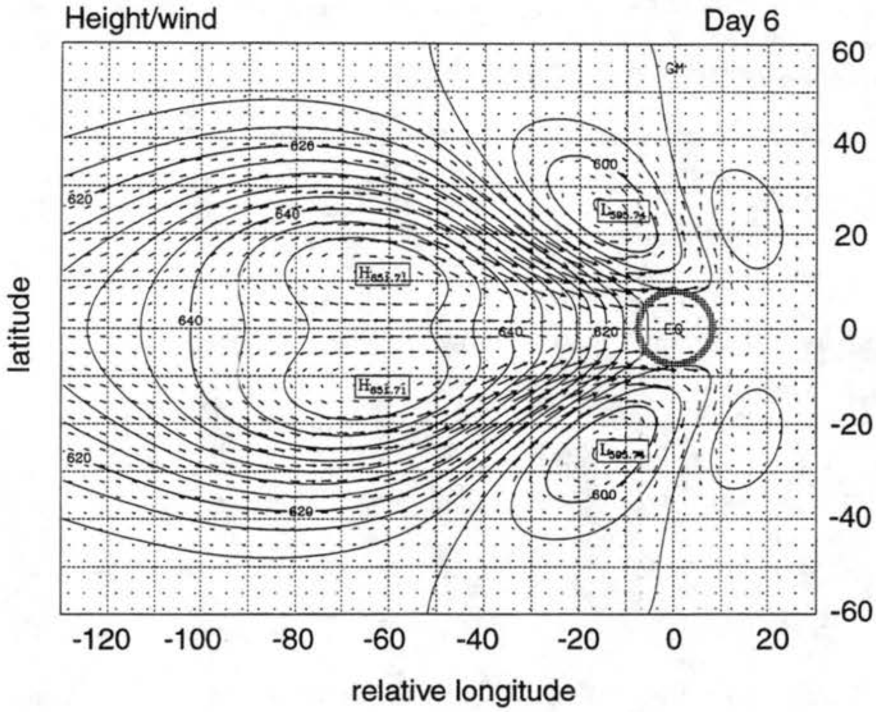

Figure 4.7: Height/wind field on Day 6 for CIRC15.

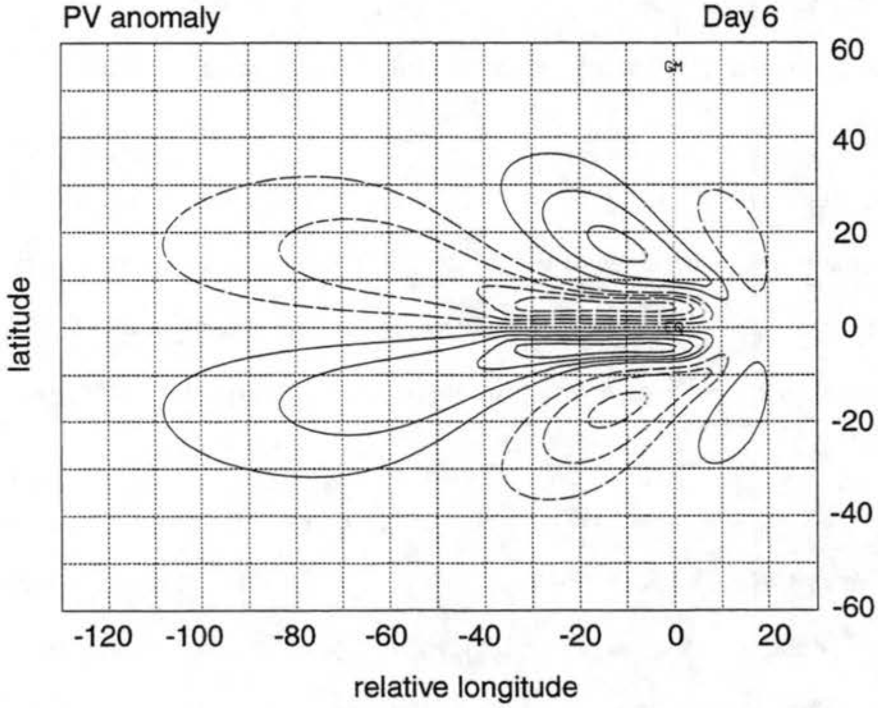

Figure 4.8: PV anomaly field on Day 6 for CIRC15. Contour interval is 2.0×10^{-6} s^{-1}.

the west of the forcing region are a result of the dispersion of long Rossby wave energy to the west, as well as the westward propagation of individual Rossby waves.

These long Rossby waves produce a local westerly acceleration in the subtropics of both hemispheres. In the presence of a basic state subtropical westerly jet, the convective forcing would accelerate the jet, producing localized wind maxima or jet streaks. Such features are observed in the South Pacific during austral summer, and are most frequently associated with tropical convective forcing (as opposed to midlatitude forcing; Vincent et al. 1997). The divergent kinetic energy generated by the addition of mass to the upper troposphere by deep tropical convection is converted into rotational kinetic energy through the emergence of Rossby waves. Nogues-Paegle and Mo (1988) show that both external and internal Rossby modes force these short-timescale jet accelerations.

4.2.2 Model evaluation with observations

Before drawing conclusions based on this simulation and those to follow, it is helpful to evaluate the model results with observations. Convection and circulation data from TOGA-COARE presented by Tyrrell et al. (1996) show both qualitative and quantitative similarities with the model output. Figure 4.9 is a plot of the 200-mb divergence (shading) and divergent wind (vectors, upper panel), and the 200-mb streamfunction field (lower panel) in the Western Pacific, averaged over 1–5 December 1992. The divergence is a measure of the strongest deep convection, which is centered just south of the Equator. Associated with this convection are two large-scale anticyclonic circulations to the north and south of the convective region, stretching 20° in latitude in each hemisphere, and 40° in the east-west direction. Zonal winds near the Equator based on this streamfunction analysis are on the order of 5 m s^{-1}. A large trough is present in the Northern Hemisphere to the east of the convection, extending over 20° longitude and digging southward almost to the Equator. The dashed lines in the Southern Hemisphere mark trough axes, which are located to the east of the center of convergence.

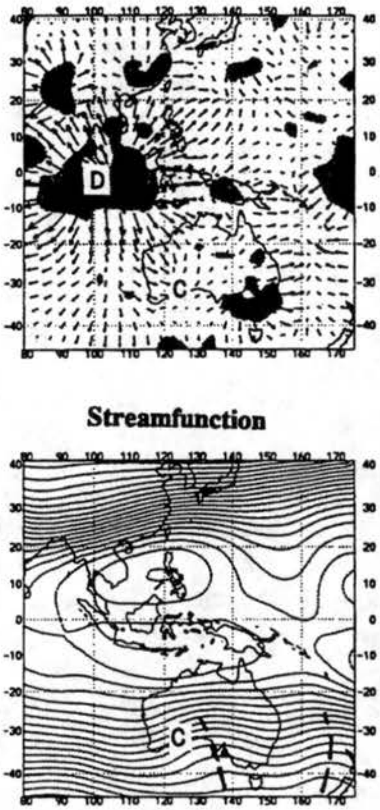

Divergence, v_χ

Streamfunction

Figure 4.9: Top: Divergence (shading) and divergent wind (vectors) at 200 mb averaged over the period 1–5 December 1992. *D* represents the center of divergence and *C* the center of convergence. Bottom: Streamfunction at 200 mb for the same time period. Contour interval 6×10^6 m^{2}s^{-1}. (From Tyrrell et al. 1996.)

When these observational data are compared with the shallow water model height and wind fields on Day 6 (Figure 4.7), the model is shown to accurately predict the size and shape of the circulation patterns associated with a region of convection centered on or near the Equator, but not the location. The model generates anticyclonic circulation cells and downstream troughs in both hemispheres, of approximately the same size as the observations. The zonal winds between these cells are on the order of 5 m s^{-1}, also similar to the observations. The entire anticyclone/cyclone pattern in the model, however, is shifted to the west of the observations. Several factors could explain this discrepency: 1) the observations are averaged over a 5-day period, whereas the model results represent the instantaneous state of the atmosphere; 2) westward Rossby wave propagation may be slower in the real atmosphere than in the barotropic model; and 3) the model does not account for the basic state winds. We conclude then that the model simulates the size, shape, and magnitude of the upper tropospheric circulation pattern fairly well, and keep in mind that the basic state winds may play a role in determining the actual location of the extratropical circulation patterns produced by tropical convection.

On a broader time-space scale, Kiladis and Weickmann (1997) document the statistical relationships between tropical convection and the extratropical circulation on a 6–30 day timescale. Figure 4.10 illustrates several examples of correlations between convection (OLR) and circulation data. Note that in many regions of the tropics, large-scale convection is associated with anticyclonic outflow at 200 mb and wavetrains extending to the east and/or the west. In general, Kiladis and Weickmann (1997) illustrate that significant circulation patterns similar to those produced by the model are associated with tropical convection in many different regions of the tropics.

4.2.3 Rossby wave energy dispersion

The model results clearly show the separation of Rossby wave energy by scale, with a longer wave packet dispersing to the west and a shorter wave packet dispersing to the east. In order to fully understand these results, expressions for the group velocity of a Rossby wave packet in both nondivergent and divergent systems are derived in this section.

The simplest case to consider is for linear, nondivergent Rossby waves on a β-plane. The dispersion relation for these waves is:

$$\nu = \frac{-\beta k}{k^2 + l^2}, \tag{4.3}$$

where ν is the frequency (in s^{-1}), $\beta = 2\Omega/a$ is the meridional gradient of the Coriolis parameter evaluated at the Equator, and k and l are zonal and meridional wavenumbers, respectively (in m^{-1}).

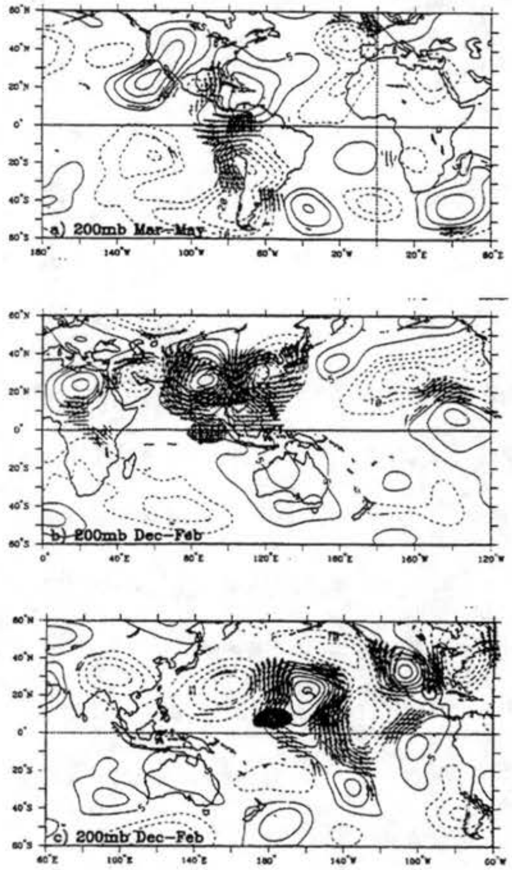

Figure 4.10: The 6–30 day 200-mb streamfunction, wind, and OLR perturbations associated with a −1 standard deviation in OLR in the regions 5°S–5°N, 80°–90°E (top), 5°–15°N, 180°–170°W (middle) and 5°S–5°N, 80°–70°W (bottom) in the months indicated. The streamfunction contour interval is 5×10^5 $\mathrm{m^2 s^{-1}}$. Shading denotes OLR anomalies less than -10 W $\mathrm{m^{-2}}$. Locally statistically significant wind vectors are shown; the longest vectors are approximately 5 m $\mathrm{s^{-1}}$. (From Kiladis and Weickmann 1997.)

The group velocity in the x-direction is calculated by taking the derivative of the frequency with respect to k:

$$c_{gx} = \frac{\partial \nu}{\partial k} = \frac{\beta(k^2 - l^2)}{k^2 + l^2}. \tag{4.4}$$

Since the sign of the group velocity determines the direction of energy propagation, Rossby wave energy will propagate to the east when the wave packet is longer in the north-south direction than in the east-west direction ($k^2 > l^2$), and to the west when the wave packet is longer in the east-west direction than in the north-south direction ($k^2 < l^2$). In spherical harmonic notation, the division between eastward and westward energy propagation occurs at:

$$m^2 = (n - m + 1)^2. \tag{4.5}$$

(The zonal wavenumbers k and m are directly related by the expression $m = ka$, where a is the radius of the Earth. The meridional wavenumber l is approximately related to the meridional nodal number $n - m$ by the relation $n - m = la - 1$.)

The Rossby wave dispersion relation can be made more accurate if the sphericity of the Earth is taken into account. In this case, the spectral space dispersion relation is given by:

$$\nu = \frac{-2\Omega m}{n(n+1)}, \tag{4.6}$$

or, in dimensional form:

$$\nu = \frac{-\beta k}{k^2 + l^2 + 2kl - (k+l)/a}. \tag{4.7}$$

The additional terms in the denominator [compare (4.7) with (4.3)] tend to decrease the Rossby wave frequencies over the β-plane case. The curve separating the eastward- from the westward-dispersing waves for nondivergent Rossby waves on the sphere is:

$$m^2 = (n - m + 1)^2 - (n - m + 1). \tag{4.8}$$

In this case, a wave packet which is slightly longer in the zonal direction than in the meridional direction can disperse energy to the east.

A wavenumber-frequency diagram for nondivergent Rossby waves on the sphere is presented in Figure 4.11. Positive frequencies represent westward phase propagation. The group velocity for a wave packet of a given zonal and meridional wavenumber is determined by the slope of the curve at that particular point. The zero group velocity curves for the β-plane and spherical cases are also plotted in Figure 4.11: note the higher accuracy of the curve calculated for the sphere. In general, as the zonal scale becomes smaller (m becomes larger), the group velocities for all meridional scales (all values of $n - m$) change from

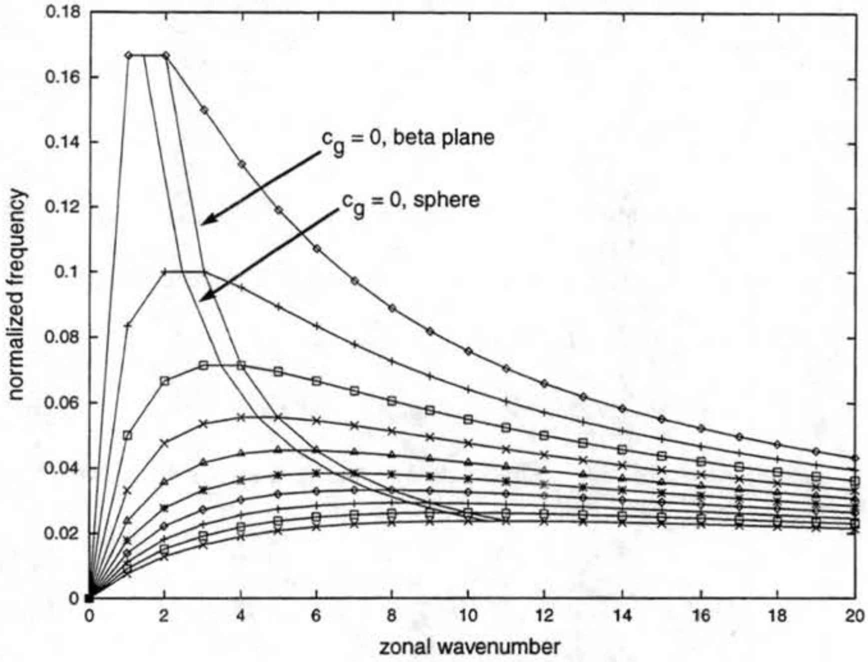

Figure 4.11: Wavenumber-frequency diagram for the nondivergent barotropic equations on the sphere. Frequencies are normalized by 2Ω. Curves are arranged by $n - m$ from 1 (top) to 10 (bottom).

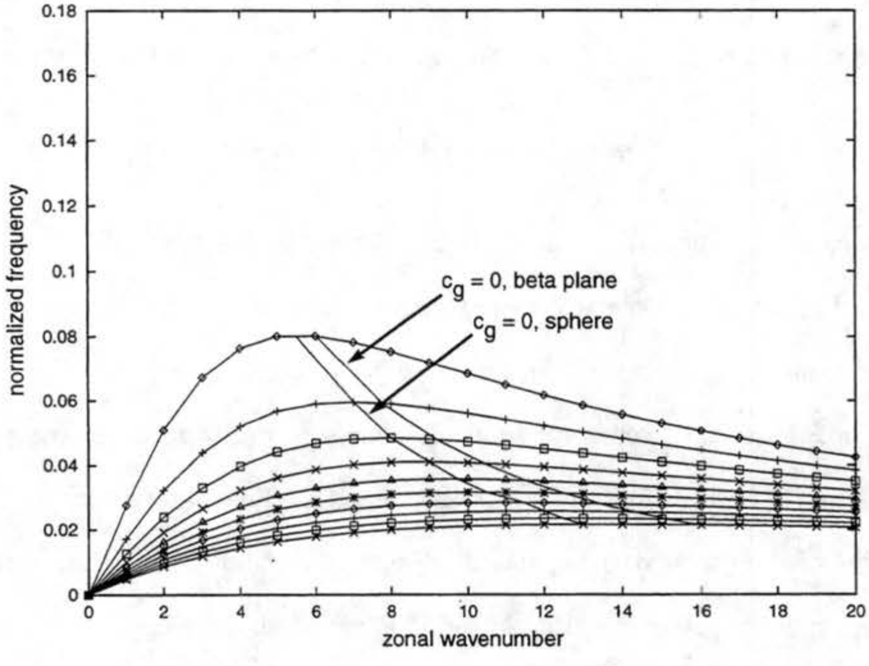

Figure 4.12: Similar to Figure 4.11, but for the divergent barotropic equations on the sphere with mean depth 608 m. Data provided by A. Kasahara, NCAR.

westward to eastward, passing through zero, then level out again to approximately zero at high m. Larger meridional scales give faster group velocities for all zonal scales.

The separation of wave energy by scale, as occurs in the shallow water model, can be interpreted as a result of the excitation of Rossby waves of one particular frequency. A horizontal line on the wavenumber-frequency diagram corresponding to a certain frequency will intersect most Rossby wave curves in two locations, corresponding to two different zonal wavenumbers. These particular Rossby waves will then be excited by the forcing. The waves of smaller zonal wavenumber, i.e. larger zonal scale, will have westward group velocities, and the waves of larger zonal wavenumber, or smaller zonal scale, will have eastward group velocities. This prediction is qualitatively seen in the shallow water model results.

Since the shallow water model is a divergent model, the nondivergent Rossby wave dispersion relation is not strictly applicable in the analysis of the results. A more appropriate dispersion relation, for linear, *divergent* Rossby waves on a β-plane, is given by:

$$\nu \approx \frac{-\beta k}{k^2 + (2n+1)\frac{\beta}{c}}, \tag{4.9}$$

(Gill 1982), where $c = \sqrt{gH}$ and n is the order of the Hermite polynomial, here analogous to $n - m$ on the sphere. The separation between westward- and eastward-dispersing wave packets is now given by:

$$m^2 = [2(n-m)+1]\frac{\beta a^2}{c}. \tag{4.10}$$

Since the shallow water model operates on the sphere, not on a β-plane, a further refinement of the divergent barotropic dispersion relation in (4.9) would need to take into account the sphericity of the Earth. However, no analytical dispersion relation exists for divergent Rossby waves on a sphere. Instead, these frequencies can be computationally determined. Figure 4.12 is a wavenumber-frequency diagram similar to Figure 4.11, but calculated specifically for the divergent barotropic equations on a sphere with a mean depth of 608 m. These frequency data were calculated by Akira Kasahara at the National Center for Atmospheric Research using code developed by Swarztrauber and Kasahara (1985). The frequencies are calculated for the normal modes of the linearized shallow water equations on the sphere (Laplace's tidal equations) using spherical vector harmonics.

Compared to the nondivergent case, all of the curves in the divergent diagram are shifted downward to lower frequencies, and the separation between eastward- and westward-dispersing wave packets is shifted to higher zonal wavenumbers. Therefore Rossby wave packets of a particular zonal and meridional scale will oscillate with different frequencies and disperse energy with different speeds (and possibly directions) in nondivergent and divergent models. In general, for a given zonal scale, the divergent equations require a much larger meridional scale for eastward energy propagation to occur. For example, given a zonal wavenumber of 6, the nondivergent diagram predicts eastward energy dispersion if $n - m$ is less than or equal to 5. In the divergent case, however, $n - m$ must be less than or equal to 1, corresponding to a much larger meridional scale.

4.2.4 Application to model results

At this point in the discussion, it is unclear how the shallow water model determines which Rossby modes will become dominant in the solution. For example, if the selection were purely based on the forcing frequency, waves of many different zonal and meridional wavenumbers would all be forced at the same magnitude. Clearly this is not the case, since the shallow water model results show a fairly smooth solution with only a few dominant wavenumbers in the response. Since the model is forced with a mass source of a particular size and shape, it is possible that the model determines the response based on this distribution. This idea will be explored in relation to the wavenumber-frequency diagram for the divergent equations.

The point representing the approximate size of the forcing in experiment CIRC15 has been plotted onto the divergent barotropic wavenumber-frequency diagram in Figure 4.13. It lies to the left of the curve dividing eastward- and westward-dispersing Rossby wave energy, in a region of minimal westward group velocity. According to this analysis, then, energy should propagate slowly westward in CIRC15. However, the model results do include some eastward-dispersing modes. Therefore this one particular point on the wavenumber-frequency diagram also does not sufficiently explain all of the wave dispersion properties inherent in the shallow water model.

Since the shallow water model operates in spectral space, the physical space forcing $\tilde{h}(\lambda, \mu)$ is decomposed into its spectral components during model integration. One way to think about the forcing in the model, then, might be to look at the spectral space coefficients corresponding to the physical space forcing. However, the forcing $\tilde{h}(\lambda, \mu)$ acts on the height field in the shallow water equations [see Q in equation (3.7)], whereas Rossby waves are controlled by the dynamics of the (potential) vorticity field. It is therefore necessary to analyze the structure of the vorticity field forcing in order to make any predictions about Rossby wave dispersion properties based on Figure 4.13.

If the height field is forced symmetrically, as in experiment CIRC15, then the divergence field will also be symmetric [see equation (3.6)], but the vorticity field will be antisymmetric. This can be shown by rearranging equation (3.5) to highlight the divergence:

$$\frac{\partial \eta}{\partial t} = -\frac{1}{a(1-\mu^2)}\frac{\partial U}{\partial \lambda} - \frac{1}{a}\frac{\partial V}{\partial \mu} - \eta\delta. \tag{4.11}$$

The divergence, an even function, is multiplied by the absolute vorticity, η, which is initially an odd function, since the basic state is at rest. The absolute vorticity anomaly field, then, is initially an odd function also, and will remain so for all time if the forcing remains symmetric about the Equator. Therefore, a better way to think about the forcing in the model would be to look at the spectral transform of the forcing (an even function, of the same physical shape as the divergence) multiplied by μ (an odd function).

The largest spectral coefficients in this transform are located in low zonal wavenumbers (small m) and large meridional nodal numbers (large $n - m$). Figure 4.14 is a representation on the wavenumber-frequency diagram of the spectral space forcing in the model. Most of the spectral power in the forcing is concentrated in the low-frequency modes with

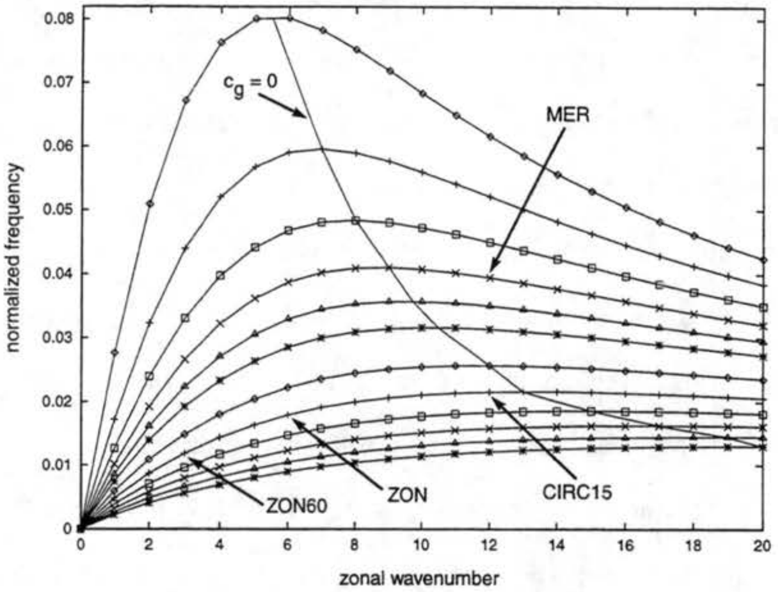

Figure 4.13: Divergent barotropic wavenumber-frequency diagram labeled with points representing shape experiments in Chapter 4. Curves are arranged by $n-m$ from 1(top) to 6, then from $n-m = 6$ to 18 in increments of 2.

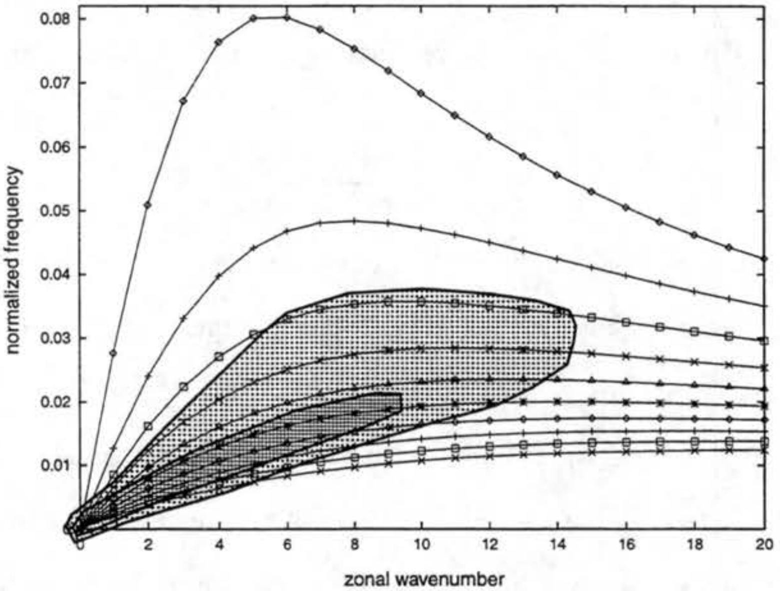

Figure 4.14: Contours of $|(h\mu)_n^m|$ for CIRC15 plotted on a wavenumber-frequency plot similar to Figure 4.13. Rossby wave curves are plotted only for $n-m = 1, 3, 5, 7, \ldots 19$, since the vorticity forcing is asymmetric. The hatched areas represent spectral coefficients larger than 0.45 (an arbitrary designation), and the dotted areas represent spectral coefficients larger than 0.40.

westward group velocities. Some weak power does exist, though, in the higher zonal wavenumber, lower meridional nodal number waves, which have eastward group velocities. This is a preliminary indication of why eastward dispersion of Rossby wave energy occurs in simulation CIRC15. The forcing in the model is actually spread over a large region of spectral space, which allows both westward- and eastward-dispersing Rossby wave packets to be excited.

4.3 Circular forcing, lower troposphere

When the forcing from experiment CIRC15 is applied to the model with a mass sink instead of a mass source, the response simulates the effect of deep tropical convection on the lower troposphere. The response is not expected to be a simple reversal of sign from the response to the upper tropospheric forcing, since the model is nonlinear.

By Day 2, the forcing has produced two closed cyclonic circulations, one on either side of the Equator, at approximately 5°N and 5°S (Figure 4.15). The wind field produced by the model is similar to the observational data in Figures 4.1–4.2. Surrounding the model cyclones are two larger regions of low pressure, with similar height anomalies to the high pressure regions produced in the upper troposphere by the mass source (compare Figure 4.15 with Figure 4.5). This result suggests that the broad-scale evolution of the fluid at this time is approximately linear. A Kelvin wave circulation appears to the east of the forcing, in an opposite sense to the upper tropospheric case, with easterly winds and a low height anomaly.

In the region of the mass sink, however, the model results do show differences from the upper tropospheric simulation. The closed cyclonic circulations in the region of the mass sink are smaller and more intense on Day 2 than the anticyclonic circulations in the upper tropospheric case, and become even stronger as the integration proceeds. This result can be understood through the PV dynamics of the nonlinear system. The PV anomalies produced in the lower troposphere are of opposite sign to those in the upper troposphere,

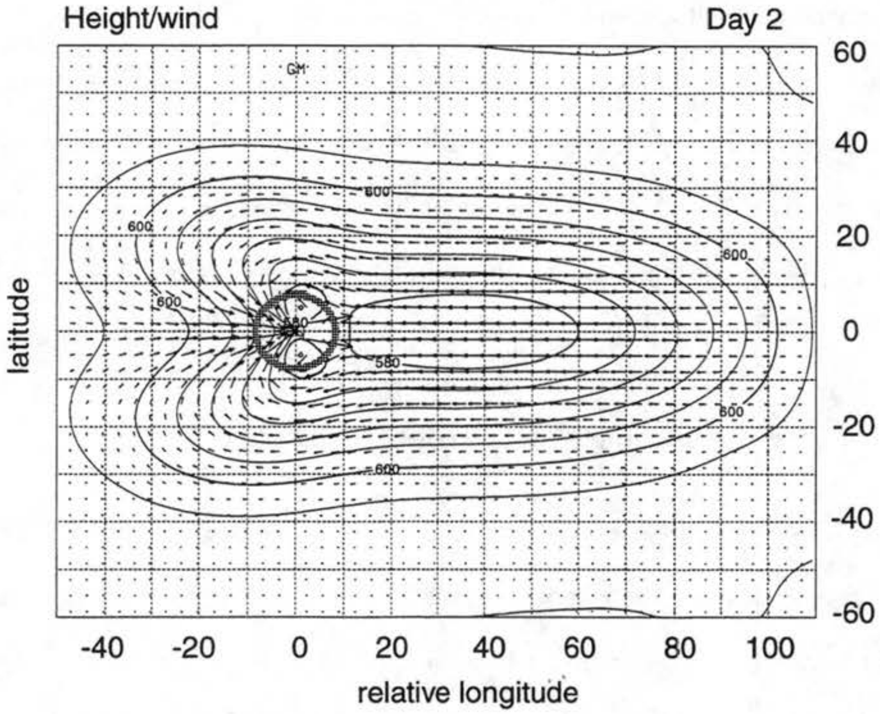

Figure 4.15: Height/wind field on Day 2 for lower tropospheric experiment CIRC15.

which results in an equatorward bending of the PV contours as high PV is pulled into the region of the mass sink. Since the potential vorticity evolution, DP/Dt, depends not only on the value of Q, but also on the value of the ambient PV, the PV anomaly in the region of the mass sink grows rapidly in magnitude. In the upper tropospheric case, on the other hand, the mass source pushes the PV contours away from the Equator, lowering the ambient PV and causing DP/Dt to be constrained in size. By Day 2, the magnitude of the PV anomaly in the lower troposphere is more than three times that in the upper troposphere. This leads to stronger, more intense circulations in the lower troposphere.

Mathematically, this result can be expressed by integrating the PV conservation equation. Approximating the material derivative DP/Dt by the local derivative $\partial P/\partial t$, thereby neglecting the effects of advection of PV (which are obviously important, but are set aside for this simple discussion), and integrating from 0 to t, (4.1) becomes:

$$\int_0^t \frac{\partial(\ln P)}{\partial t'} dt' = -\int_0^t \frac{Q}{h} dt'. \tag{4.12}$$

Solving for P under the assumption that Q is constant in time, we obtain:

$$P(t) = P(0)e^{-\frac{Q}{h}t}. \tag{4.13}$$

When Q is positive, in the upper troposphere, the PV in the mass source region decreases exponentially until it reaches a value of zero. As the PV decreases to zero, DP/Dt also decreases to zero, until the local PV is changed by advection only. In this case, the mass source is not very "efficient" at producing a PV anomaly of large magnitude.

When Q is negative, in the lower troposphere, the PV in the mass sink region grows exponentially at all times. Thus DP/Dt also grows exponentially with time. The mass sink can be thought of as becoming more "efficient" as time progresses, since it produces larger PV anomalies from the same magnitude of the mass sink. Thus for the same forcing (i.e., deep convection removing the same amount of mass from the lower troposphere as it adds to the upper troposphere), the PV anomalies, and hence the circulations, are much stronger in the lower troposphere than in the upper troposphere. This simple argument explains why strong, tight circulations associated with deep convective episodes are observed in the lower troposphere (e.g., tropical depressions and disturbances), but not in the upper troposphere.

In a linear system, these differences between the upper and lower troposphere would not be apparent. The right hand side of the PV equation (4.1) would be linearized to $-fQ/H$, so that the local PV evolution would depend only on the magnitude of f, not on the magnitude of the PV. Thus the upper and lower tropospheric fields would differ only in the sign of the anomalies, not in their intensity or size.

The relative size of the induced circulations can be explained more readily by the wind fields themselves. Since PV is advected largely by the divergent part of the wind in the vicinity of the mass source/sink, high PV is pulled into the region of the mass sink in the lower tropospheric simulation, which concentrates the high vorticity into a small region. The circulation produced is therefore small and intense. In the upper tropospheric simulation, on the other hand, the divergent wind pushes the higher vorticity away from

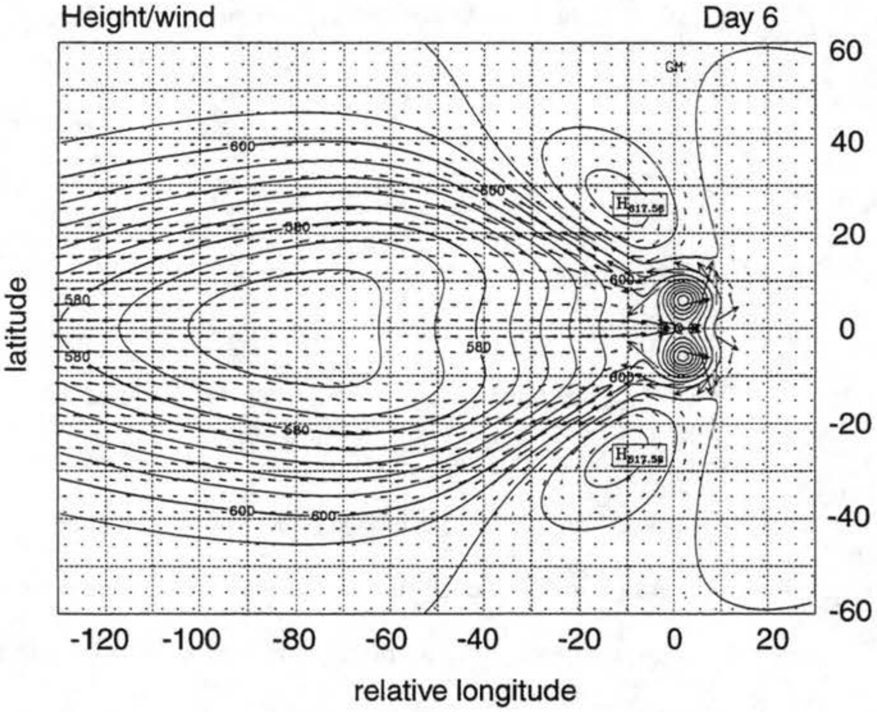

Figure 4.16: Height/wind field on Day 6 for lower tropospheric experiment CIRC15.

the region of the mass source, which spreads out the vorticity into a larger area. Thus the upper tropospheric circulations are larger and less intense.

Kiladis and Weickmann (1997) provide clear observational evidence, based on global convection and circulation data, for circulation fields similar to those produced by the nonlinear model. Equatorial convection is correlated with small twin cyclonic circulations in the lower troposphere and broad, diffuse anticyclones in the upper troposphere.

By Day 6 in the shallow water model integration, when the forcing has ended, a broad area of low pressure has spread to the west of the forcing region (Figure 4.16), and high pressure regions have formed to its northeast and southeast by eastward Rossby wave dispersion. The cyclones from Day 2 have continued to strengthen while remaining stationary, with maximum winds of 10 m s^{-1}. These circulations can be likened to twin tropical cyclones in the Western Pacific (Ferreira et al. 1996).

When the lower and upper tropospheric circulations on Day 6 of the simulations are compared (Figures 4.16 and 4.7), the broad-scale circulations seem to be very similar in magnitude and size, although opposite in sign, of course. However, the lower tropospheric circulation contains the additional intense cyclones in the region of the forcing, whereas the upper tropospheric circulation contains no analog to this circulation.

This result hinges on the nonlinearity of the shallow water model. In the upper tropospheric case, the forcing allows the circulation to remain within a linear regime, so that the PV contours simply undulate and Rossby wave energy disperses. In the lower tropospheric case, however, the efficiency of the mass sink allows the creation of very large PV anomalies, which shift the flow near the forcing region into a nonlinear regime. Since the circulation around the cyclones is so intense, and constrained to such a small region, low magnitude PV is advected strongly poleward to the east of the cyclones and high PV is advected equatorward to their west. This causes the eventual wave breaking of PV contours to the west of the cyclones (Figure 4.17).

Outside of this small region of the intense cyclones, however, the PV contours simply undulate without rolling up or breaking nonlinearly, in a similar manner to the upper tropospheric simulation. This is caused by a similar dispersion process to the west of the forcing region in the lower and upper tropospheric simulations. When the forcing is initially turned on in both cases, a long Rossby wave forms to the west of the forcing. This wave produces an anticyclonic circulation in the upper troposphere and a cyclonic circulation in the lower troposphere, with winds which advect the PV such that the PV anomalies propagate westward. These circulations are far enough removed from the mass forcing region that their evolution does not depend to a large extent on what is happening near the forcing.

In summary, linear Rossby wave dispersion away from a mass source/sink proceeds in a similar manner in the upper and lower troposphere, producing similarly-sized but opposite-signed PV anomalies. In the lower troposphere, however, the forcing creates larger

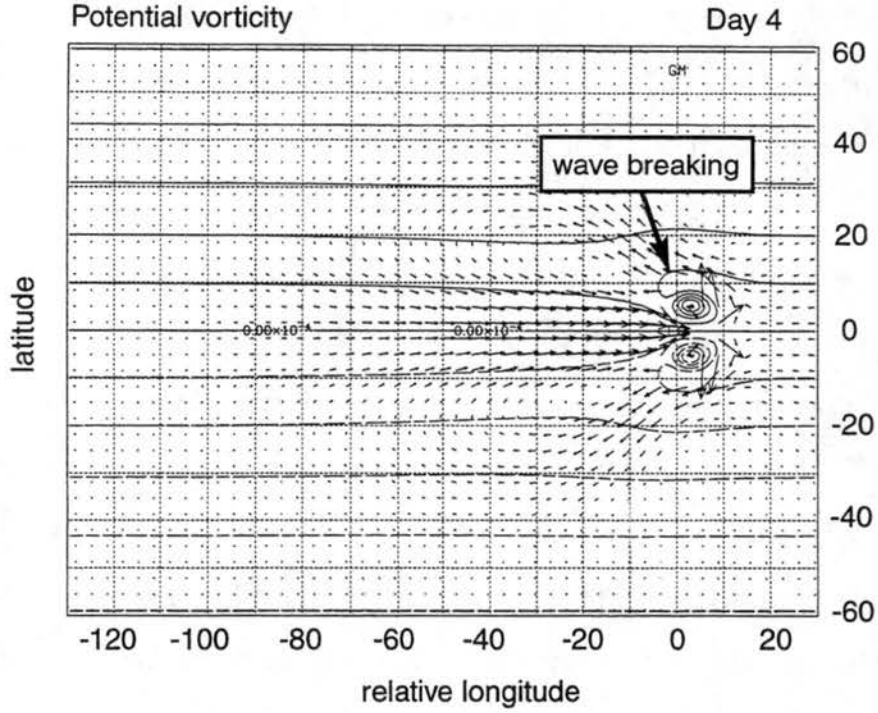

Figure 4.17: Potential vorticity field on Day 4 for lower tropospheric experiment CIRC15. Contour interval is 2.5×10^{-5} s^{-1}.

PV anomalies than in the upper troposphere, which allows the flow to enter a nonlinear regime in the vicinity of the forcing. This nonlinearity allows intense cyclones to be sustained in the lower troposphere, while no significant circulation features remain within the forcing region in the upper troposphere.

4.4 Comparisons: shape of convection

In this section, the effect of the physical shape of tropical convection on the upper tropospheric extratropical circulation fields, or teleconnection patterns, is investigated. Specifically of interest is determining what convective forcing shape produces the maximum response to the east of the forcing. This result will give insight into the mechanisms by which strong eastward teleconnection patterns are produced in the atmosphere.

4.4.1 Zonally-elongated forcing

Large-scale tropical convection is more often zonally elongated than circular in shape. Experiment ZON was run to compare the differences in wave dispersion and propagation between circular and zonally-elongated convective forcing. The forcing region in ZON is elliptical, with dimensions of 30 degrees longitude by 15 degrees latitude. Forcing is centered at the Equator. The magnitude of h_0 is 750 m in ZON, so that the total mass added to the system after 6 days of forcing is equal to that in experiment CIRC15.

By Day 2, the zonally-elongated forcing produces a smaller maximum PV anomaly than the circular forcing. The PV conservation equation (4.1) predicts this result, since the forcing magnitude h_0 in ZON is smaller than in CIRC15, and extends over the same range of basic state PV (i.e., has the same latitudinal extent).

When the forcing ends on Day 6, Rossby waves have dispersed from the region of the forcing in a similar manner as in CIRC15, with long waves emerging to the west and shorter waves to the east (Figure 4.18). All of the height anomalies are smaller in magnitude in ZON than in CIRC15, with larger differences in the cyclones than in the anticyclones. The PV anomaly field is also weaker throughout experiment ZON (Figure 4.19). Since the maximum PV anomalies produced directly by the forcing are smaller, Rossby wave dispersion in ZON excites new PV anomalies which are also smaller in magnitude than those in CIRC15. Thus weaker circulation anomalies are present in all of the dispersed Rossby waves.

The shape of the forcing not only determines the maximum PV anomalies produced, but also determines the proportion of Rossby wave energy which disperses to the east and to the west. Proportionally less wave energy, as measured by the PV anomalies, is dispersed to the east in ZON than in CIRC15. This energy disperses at the same speed in ZON and CIRC15, however, since PV anomalies appear in the same locations at the same times in both simulations. It is only the magnitude of these anomalies which differs significantly.

The height fields on Day 6 in ZON and CIRC15 illustrate that these small differences in PV anomalies do not make a very large difference in the circulations produced. However,

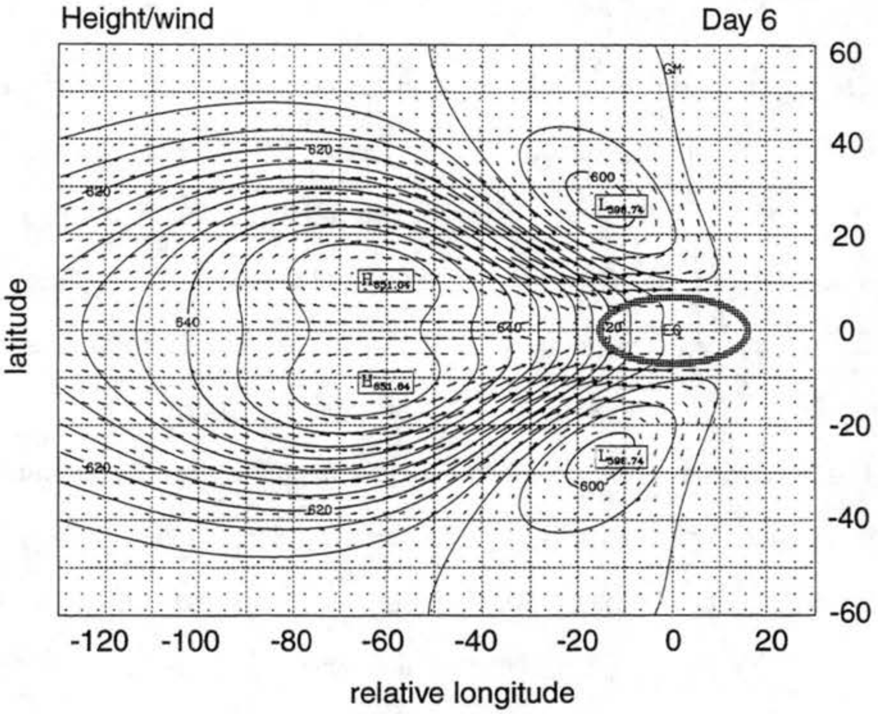

Figure 4.18: Height/wind field on Day 6 for ZON.

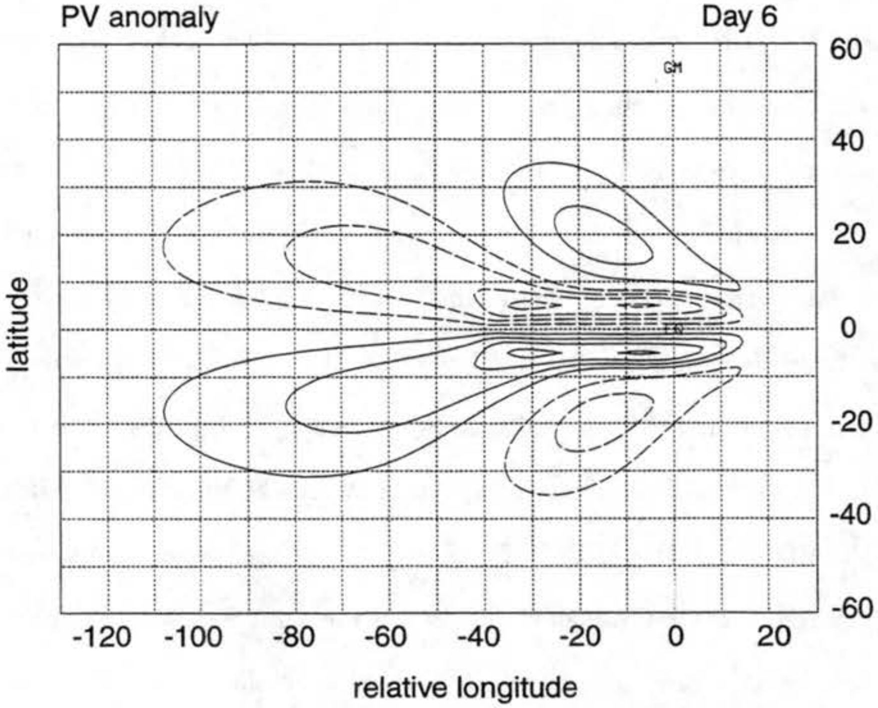

Figure 4.19: PV anomaly field on Day 6 for ZON. Contour interval is 2.0×10^{-6} s^{-1}.

the short Rossby waves excited by eastward dispersion show more height and wind field differences than the long waves to the west of the forcing, which remain fairly constant in strength between simulations.

The mass source was then elongated again in the zonal direction to a length of 60° longitude, while the meridional dimension was held constant at 15°. The magnitude of the mass source (h_0) in this experiment, ZON60, is decreased to 375 m so that the total mass added to the model is equal to that in the previous two experiments. This value of h_0 represents a heating rate of only one-half the mean heating rate in the Western Pacific, in order to keep consistent with the addition of mass in all other simulations. We feel that this is appropriate, however, since such a large convective region is most likely not completely filled with deep convection, but rather has some areas of more concentrated convection and some clear areas. The low heating rate thus represents an average over the entire region.

The height/wind and PV anomaly fields on Day 6 (Figures 4.20 and 4.21) further solidify the conclusions reached for ZON. By lengthening the mass source again in the zonal direction, the maximum PV anomalies are weakened throughout the simulation, and the proportion of Rossby wave energy dispersed to the east becomes even smaller. The PV anomalies appearing to the east in ZON60 are approximately one-third the magnitude of those in CIRC15.

Comparing the height/wind fields for simulations ZON60, ZON, and CIRC15 (Figures 4.20, 4.18, and 4.7), it is apparent that the shape of the forcing affects the circulation anomalies produced by eastward Rossby wave dispersion much more than those produced by westward dispersion. The anticyclonic circulations to the west are nearly identical between simulations, whereas to the east, two circulation centers are present in CIRC15 which do not appear at all in ZON60. The PV anomalies produced by the forcing also become more zonal in shape as the forcing itself becomes more zonal. The maximum PV anomalies created by eastward Rossby wave dispersion are located farther to the northwest in ZON60 than in ZON or CIRC15.

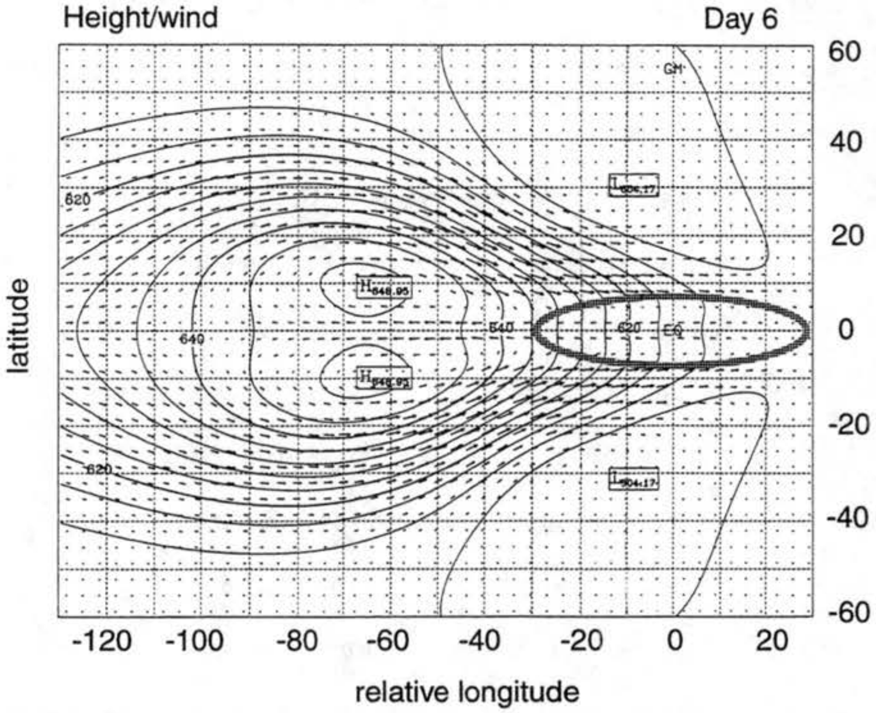

Figure 4.20: Height/wind field on Day 6 for ZON60.

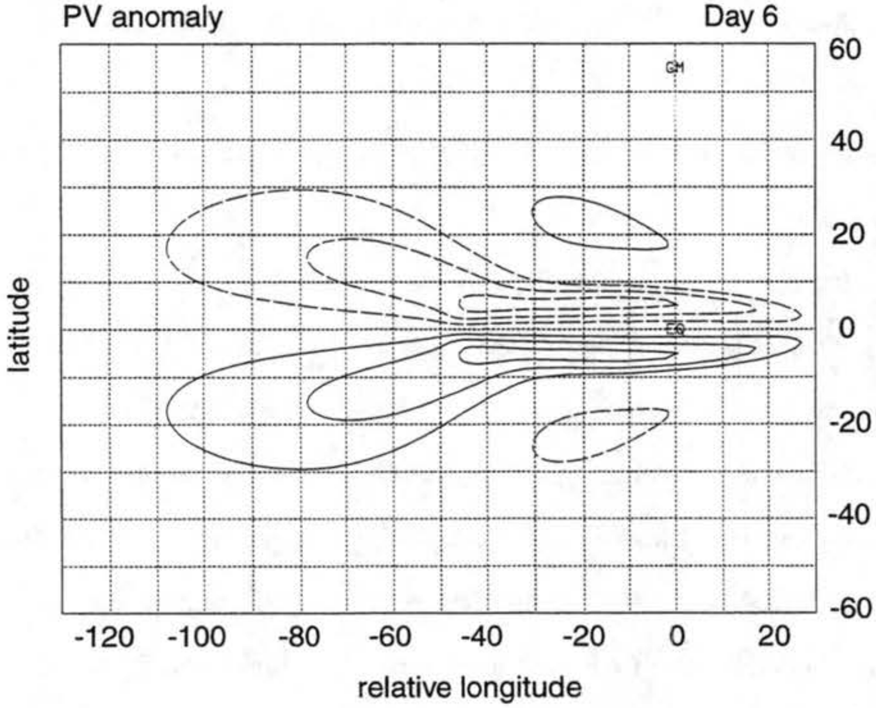

Figure 4.21: PV anomaly field on Day 6 for ZON60. Contour interval is 2.0×10^{-6} s^{-1}.

Simulations CIRC15, ZON, and ZON60 have shown that the meridional extent of the forcing determines the maximum PV anomalies which can be produced by a tropical convective region, and hence determines the magnitude of the PV anomalies created by Rossby wave dispersion. In addition, the shape of the forcing determines the proportion of Rossby wave energy which disperses to the east and to the west. These results may be understood by again examining the wavenumber-frequency diagram for the shallow water model (Figure 4.13). In the simplest sense, the total forcing in ZON and ZON60 is represented by the single points labeled on the diagram, which lie well to the left of the zero group velocity curve. From these points alone, we would expect the group velocities in experiments ZON and ZON60 to have stronger westward components than in CIRC15. This hypothesis is substantiated in the model results.

When the spectral coefficients of the forcing in ZON are plotted onto the wavenumber-frequency diagram (Figure 4.22), it is apparent that increasing the zonal scale of the forcing constrains the strongest wave response to lower zonal wavenumber Rossby waves, as expected (compare with Figure 4.14). The strongest response in ZON is limited to zonal wavenumbers 0–3, whereas it extends out to wavenumber 9 in CIRC15. Thus the longest zonal wavelength Rossby modes, with the largest westward group velocities, are forced at approximately the same magnitude in ZON and CIRC15, whereas the shorter zonal wavelength modes, still with westward group velocities, are forced more strongly in CIRC15. Thus the superposition of the modes with westward group velocities is stronger in CIRC15 than in ZON, so the height and wind fields are also more intense. The eastward-propagating modes are also forced more strongly in CIRC15 than in ZON, which is evidenced in the model results.

In ZON60, the highest power in the forcing is constrained even more strongly to the low zonal wavenumber Rossby waves (Figure 4.23). Only the zonally symmetric and zonal wavenumber 1 modes are forced at the same magnitude as they are in CIRC15 and ZON; the remainder of the westward-dispersing modes are weaker. Thus in the model results we see

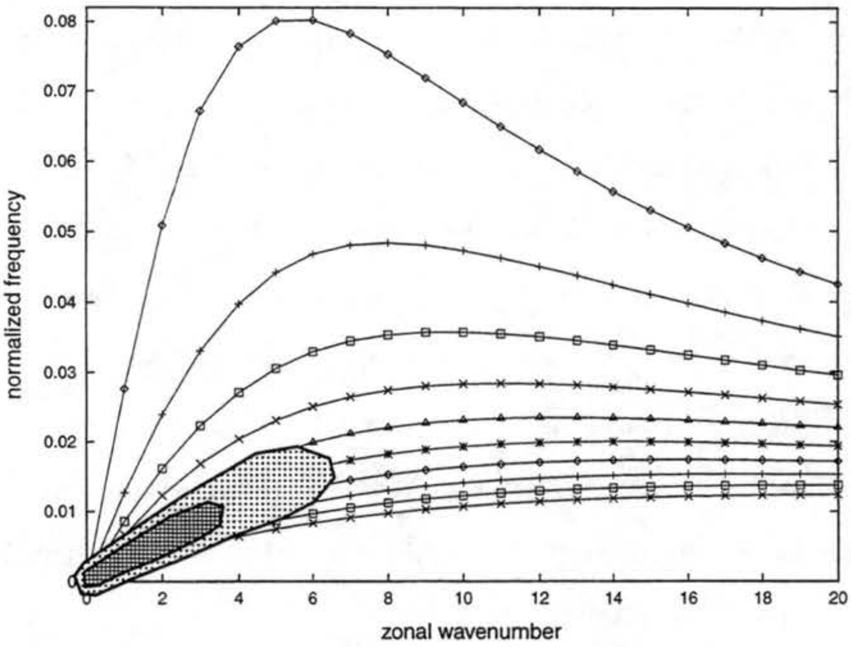

Figure 4.22: Contours of $|(h\mu)_n^m|$ for ZON plotted on the wavenumber-frequency plot from Figure 4.14. Shading intervals identical to Figure 4.14.

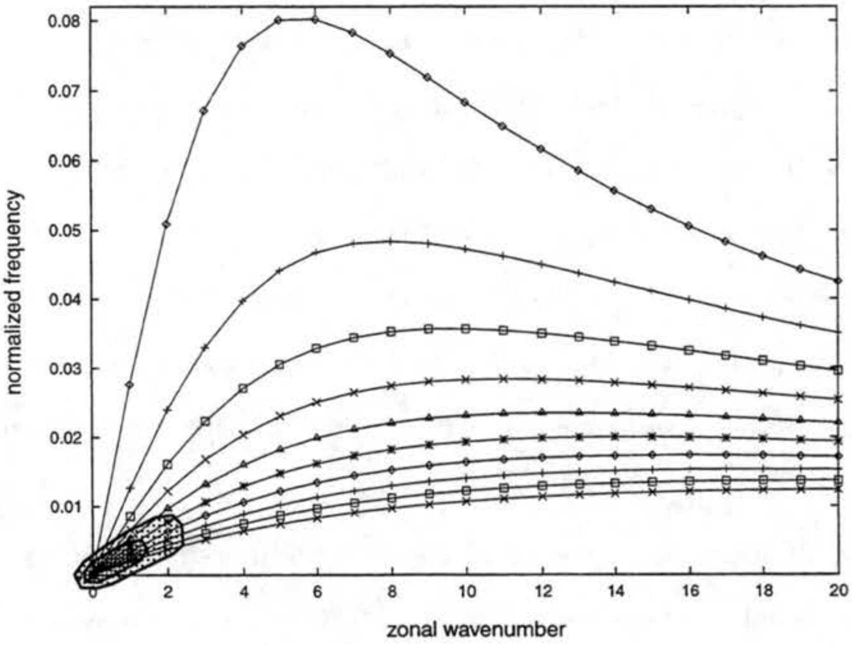

Figure 4.23: Same as Figure 4.22 but for ZON60.

very little eastward dispersion of Rossby wave energy, and similar, but longer wavelength, westward dispersion.

In all three simulations, all of the Rossby modes pictured on the wavenumber-frequency diagram in Figure 4.13 are forced to some extent. The shape of the mass source simply determines how strongly each of these modes is forced. When the forcing is zonally elongated, the low zonal wavenumber modes are forced most strongly. As the forcing becomes shorter in the zonal direction, the area of highest spectral power extends farther out into the higher zonal wavenumber modes. Larger PV anomalies are produced by the forcing, and the waves with eastward group velocities are forced more strongly. The superposition of all of these Rossby modes then determines the response seen in the physical space results.

4.4.2 Meridionally-elongated forcing

The wavenumber/frequency diagram indicates that the eastward group velocity of a short Rossby wave packet should increase if the meridional scale of the forcing in CIRC15 is increased while the zonal scale is held constant. Experiment MER was run to determine whether the eastward dispersion of short Rossby waves is indeed stronger, i.e., the resultant waves have higher amplitude and disperse farther to the east, when the meridional wavelength of the forcing is increased.

The mass source in experiment MER is identical to the mass source in ZON in dimensions and magnitude, but it is rotated 90° so that the major axis of the ellipse is in the north-south direction. All other parameters are identical to those used in previous simulations. This point is labeled on Figure 4.13 as MER.

On Day 2, the maximum PV anomalies in experiment MER are larger than in either CIRC or ZON. This result clearly illustrates the dependence of the maximum PV anomaly on the latitudinal extent of the mass source. Although the mass source in MER is approximately half as strong as in CIRC15, it produces a larger PV anomaly because it extends into higher latitudes, i.e., regions of higher ambient PV. Experiment MER also produces a

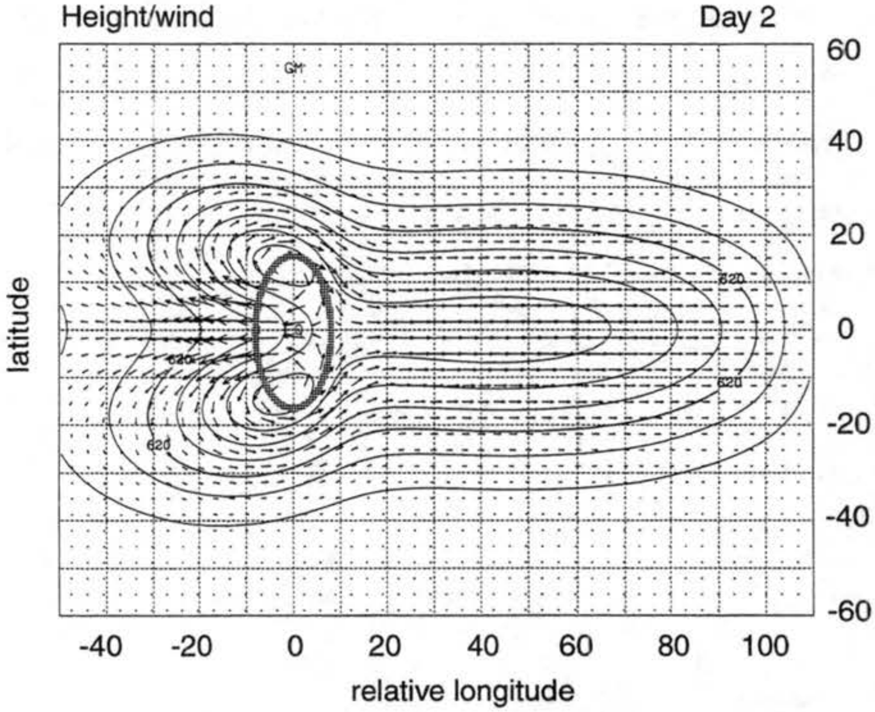

Figure 4.24: Height/wind field on Day 2 for MER.

larger PV anomaly than experiment ZON, which has equal magnitude forcing. Since the PV anomalies in MER are larger than those in CIRC15 or ZON, the induced circulations in MER are stronger. The height/wind field for Day 2 of MER (Figure 4.24) illustrates this result.

An interesting feature to note in Figure 4.24 is the presence of equatorward flow inside the mass source region. This result seems counterintuitive, since one might expect the fluid to flow *away from* the positive height anomaly produced by the forcing, not toward it. However, this result is consistent with the results of Gill (1980) and is in fact predicted by steady-state, linear theory (and also can be generalized to transient forcing and a nonlinear system). Assuming a steady-state flow linearized about a basic state of rest, the absolute vorticity conservation equation for a shallow water system is:

$$\beta v + f\delta = 0. \tag{4.14}$$

This equation states that in a steady-state flow, divergence induces equatorward flow. The shallow water mass continuity equation under these same conditions is:

$$\delta = \frac{Q}{H}. \tag{4.15}$$

Substituting (4.15) into (4.14), we obtain:

$$\beta v = -\frac{fQ}{H}. \tag{4.16}$$

Inside the region of the mass source, where Q is positive, the meridional wind v must be equatorward. This predicted result is seen in the wind fields for all forcing shapes in the shallow water model, although it does not appear until after Day 2 for shapes which do not extend as far in the north-south direction as MER.

Returning to the shallow water model results for MER, surprisingly large differences are seen in the PV anomaly fields between experiments MER and CIRC15 on Day 6 (compare Figures 4.26 and 4.8). By doubling the meridional scale of the mass source, the amplitude of the PV anomaly produced by eastward Rossby wave dispersion increases by at least a factor of 2. The proportion of energy dispersing to the east is also higher in MER than in any of the other simulations. This result is apparent in the height/wind field in Figure 4.25.

This result can again be understood through the wavenumber/frequency diagram (Figure 4.13). In the simplest sense, moving the total forcing upward on the diagram to a lower $n-m$ curve corresponds to a greater eastward group velocity for short Rossby waves. In addition, this particular example moves the point representing the total forcing to the right of the zero group velocity curve, which means in the broad sense that the total group velocity should be to the east.

The spectral breakdown of the forcing in MER provides more evidence for the strong eastward Rossby wave dispersion (Figure 4.27). The power is highly concentrated into the high $n-m$ modes (1, 3, and 5), which have significant eastward group velocities. In addition, the maximum coefficients in these modes are at least twice the magnitude of the westward-dispersing modes in the other three experiments.

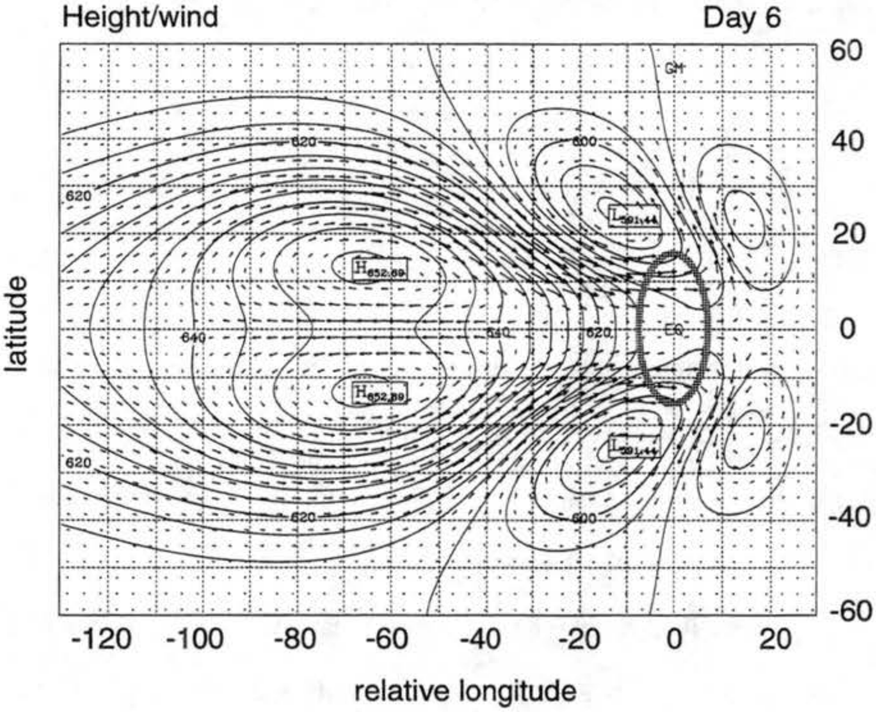

Figure 4.25: Same as Figure 4.24 but on Day 6.

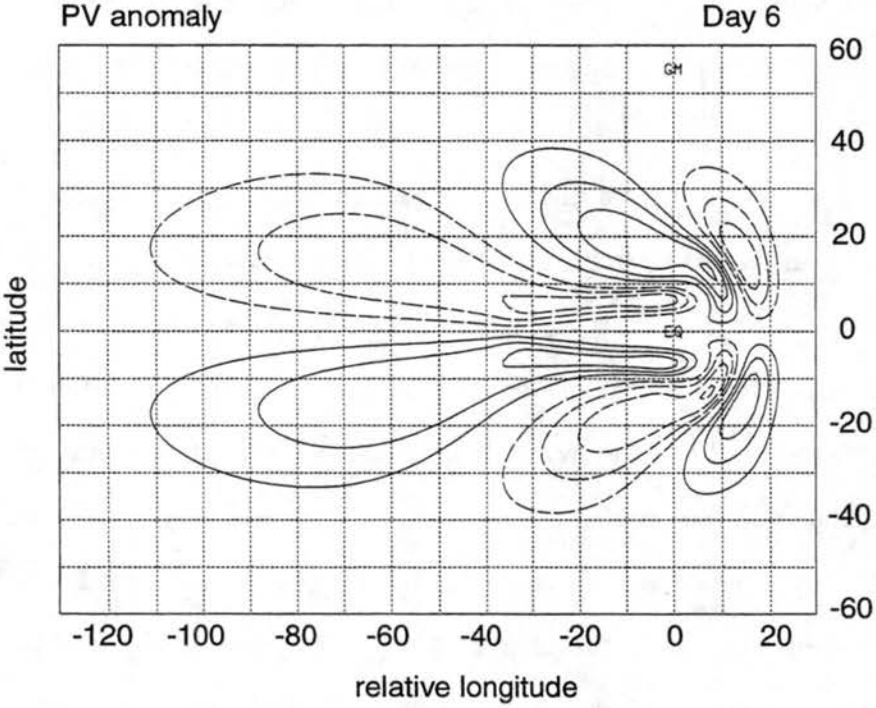

Figure 4.26: PV anomaly field on Day 6 for MER. Contour interval is 2.0×10^{-6} s^{-1}.

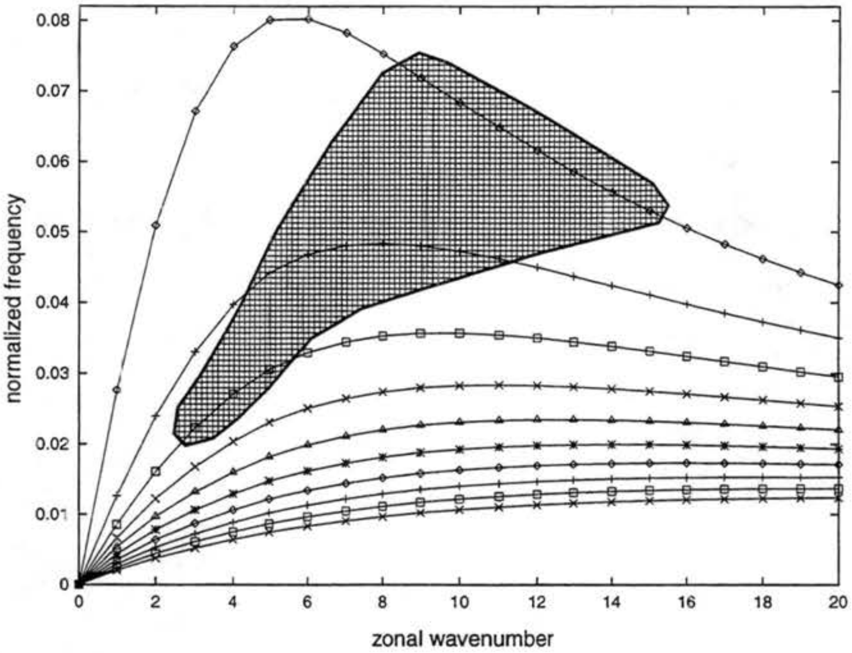

Figure 4.27: Contours of $|(h\mu)_n^m|$ for MER plotted on the wavenumber-frequency plot from Figure 4.14. Shaded area represents spectral coefficients greater than 1.0.

A remarkable difference between experiment MER and the previous three upper tropospheric experiments (CIRC15, ZON, and ZON60) is that the amplitudes and locations of the westward-propagating waves remain fairly constant regardless of the shape of the mass source, while the amplitudes of the eastward-propagating waves vary much more significantly. Since the waves which disperse to the west are long waves, i.e., large in horizontal extent, small differences in PV anomalies between forcing shapes do not make a large difference in the circulations produced. The short waves which disperse to the east, however, are much smaller in area, so they respond more strongly to small changes in PV anomalies produced by changes in the mass source shape.

An important conclusion to draw from these results is that the strength and location of the circulation fields produced by tropical convection do not simply depend on the intensity of the convection. Instead, it is a combination of the strength of the convection and its horizontal shape which determine the strength and location of the circulation fields.

4.4.3 Changes to the zonally-averaged circulation

The shallow water model simulations have emphasized the differences in the total circulation between different convective forcing shapes. Another way to examine these effects is through the zonally-averaged circulation. The zonally-averaged zonal momentum equation can be written as:

$$\frac{\partial \bar{u}}{\partial t} - \frac{\overline{hPv}}{H} = 0, \tag{4.17}$$

where the overbars represent normal zonal averages.

Defining a mass-weighted zonal average as:

$$\hat{v} = \frac{\overline{hv}}{\bar{h}}, \tag{4.18}$$

and its deviation as:

$$v^* = v - \hat{v}, \tag{4.19}$$

(4.17) can be rewritten as:

$$\frac{\partial \bar{u}}{\partial t} = \frac{\bar{h}\hat{P}\hat{v}}{H} + \frac{\overline{hP^*v^*}}{H}. \tag{4.20}$$

The first term on the right hand side represents the flux of the zonal mean PV by the mean meridional mass flux. The second term represents the flux of the eddy PV by the eddy meridional mass flux. This term can be equated to the pseudodivergence of a generalized Eliassen-Palm Flux, as shown by Ferreira and Schubert (1999). The sum of these two terms forces the zonal mean flow. When (4.20) is integrated in time, the change in the zonal mean zonal wind can be computed:

$$\Delta u = \int_0^t \frac{\bar{h}\hat{P}\hat{v}}{H} dt' + \int_0^t \frac{\overline{hP^*v^*}}{H} dt'. \tag{4.21}$$

Figures 4.28 and 4.29 are plots of the three terms in (4.21) as functions of latitude for experiments ZON60 and MER. In both experiments, the change in the zonal mean zonal wind is westerly everywhere. This result is consistent with observations of a strengthening of the subtropical westerly jets by MJO convection (Vincent et al. 1997). In ZON60, this westerly acceleration is produced mainly by the action of the mean meridional circulation.

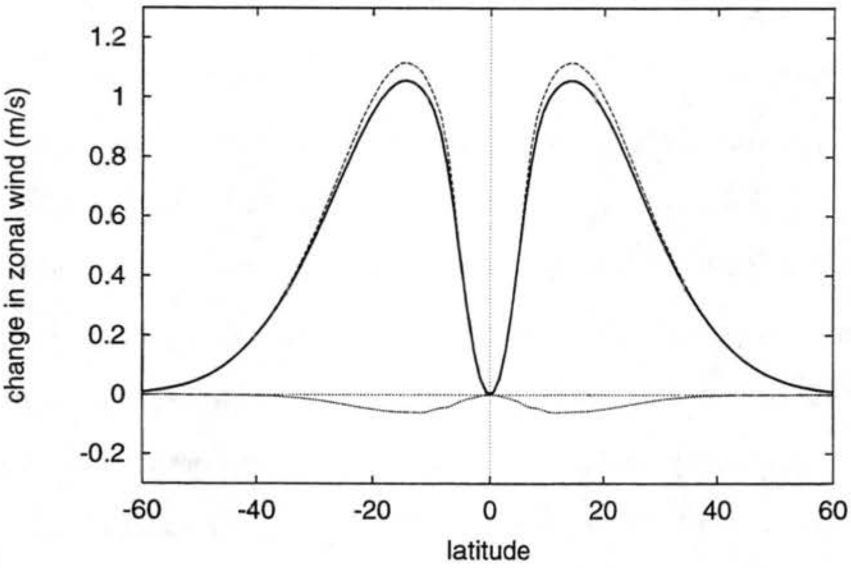

Figure 4.28: Change in the zonal mean zonal wind (thick solid line, in m s^{-1}) and time-integrated forcing by the mean meridional circulation (dashed line) and eddy circulation (dotted line) on Day 6 of ZON60.

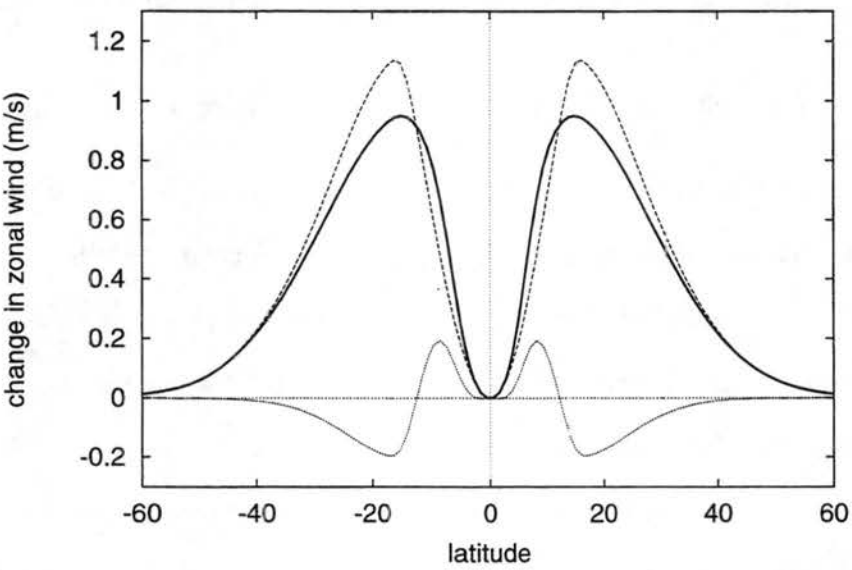

Figure 4.29: Same as Figure 4.28 but for MER.

The eddy circulation does not affect the total circulation to a large extent; it produces a weak easterly acceleration equatorward of 40°. This easterly acceleration results from the equatorward flux of PV through the strong equatorward flow on the east side of the anticyclones, where the PV anomalies are large (see Figures 4.20 and 4.21).

The meridionally-elongated forcing also produces a westerly acceleration in all latitudes, but the maximum acceleration is smaller than for zonally-elongated forcing. As was seen in the shallow water model results, the eddies play a larger role in MER than in ZON60. In the zonally-averaged results, the eddy circulation in MER damps the total westerly acceleration by producing a stronger easterly acceleration between 10° and 40°. This easterly acceleration is stronger in MER because the equatorward wind on the east sides of the anticyclones is stronger and has a greater equatorward component of motion than in ZON60 (see Figure 4.25).

In summary, the zonal mean circulation produced by equatorially-centered convective forcing tends to produce a westerly acceleration on the zonal mean zonal wind, while the eddy circulation produces an easterly acceleration. When the eddies are weak, as in ZON60, the subtropical westerlies are accelerated more than when the eddies are strong, as in MER.

4.4.4 Implications for Pacific teleconnection patterns

The simulations presented thus far have shown that the horizontal shape of tropical convection can have a large effect on the response of the circulation. When the convection is meridionally elongated, it produces large PV anomalies and a strong eastward short Rossby wave response. When the convection is zonally elongated, the maximum PV anomalies are much smaller, and the eastward dispersion of short Rossby wave energy is weaker.

Equatorially-centered tropical convection is most frequently observed in the Indian Ocean and Western Pacific Warm Pool during spring and fall. For example, as an MJO convective envelope propagates eastward, it can produce a number of quasi-stationary large-scale convective bursts of different sizes and shapes. In addition, when the convection reaches the Dateline, it is prevented from propagating farther to the east by colder sea surface temperatures, and generally remains stationary for a number of days. During these periods of stationary tropical convection, the response of the atmosphere is expected to be similar to the shallow water model response. Thus the physical shape of the convection should play a large role in determining the strength and location of the upper tropospheric Rossby wave circulations, as well as the locations of subtropical jet streaks.

The short Rossby waves produced by stationary MJO convection can have a far-reaching effect when the basic state winds are taken into account. A modest subtropical westerly flow of approximately 5 m s^{-1} in the shallow water model will allow short Rossby waves to affect the extratropical circulation 70° to the east of the forcing by Day 10 (not shown). Meehl et al. (1996) show that observed MJO convection on a 6–30 day timescale in the Indian Ocean is associated with a Northern Hemisphere upper tropospheric wavetrain which arcs across the Western Pacific, contributing to the development of convective activity in the Eastern Pacific. When the downstream wavetrain pattern is most developed, the composite convection is meridionally elongated in shape. This correlation together with the results from the shallow water model suggest that the strength of cross-Pacific teleconnection patterns may depend on the horizontal distribution of equatorially-centered tropical convection.

4.5 Location of convective forcing

The ITCZ migrates from the Northern Hemisphere to the Southern Hemisphere and back each year in the Western Pacific, and can often exist in both hemispheres at once. In the Eastern Pacific and Atlantic, the ITCZ remains in the Northern Hemisphere year round. Tropical convection is thus not always centered exactly on the Equator, as was depicted in the first set of experiments. For example, convection in the Western North Pacific in boreal summer tends to cluster in the Northern Hemisphere ITCZ and in the summer monsoon trough, both located northward of approximately 10°N.

Experiment OFFZON was run to determine the effects of off-equatorial forcing on the tropical and extratropical circulation fields. The forcing in this experiment is of the same shape and magnitude as in experiment ZON, but is centered at 10°N. The timescale of forcing remains at 6 days.

Initially, the most prominent difference between experiments ZON and OFFZON is the asymmetry of the response in OFFZON. Since the forcing is located entirely within the Northern Hemisphere, the response is strongest there. In fact, the maximum PV anomaly in the Northern Hemisphere on Day 2 is stronger even than in MER, since more of the area of the mass source is located in higher latitudes, where the ambient value of PV is larger.

The height/wind fields on Day 2 (Figure 4.30) show two Rossby wave circulations, one in each hemisphere, even though the forcing is limited to the Northern Hemisphere alone. The generation of Rossby waves in the Southern Hemisphere, far removed from the forcing itself, can be understood by considering the Rossby wave source (Sardeshmukh and Hoskins 1988). The Rossby wave source S is defined as a residual term in the absolute vorticity conservation equation for a divergent barotropic fluid:

$$\left(\frac{\partial}{\partial t} + \mathbf{v}_{\psi} \cdot \nabla\right) \eta = S, \tag{4.22}$$

where

$$S = -\nabla \cdot (\mathbf{v}_{\chi} \eta), \tag{4.23}$$

and the vector wind $\mathbf{v}$ has been divided into its rotational ($\mathbf{v}_{\psi}$) and divergent ($\mathbf{v}_{\chi}$) components. If S is linearized about a resting basic state, denoted by overbars, the Rossby wave source becomes:

$$S = -\mathbf{v}_{\chi} \cdot \nabla \bar{\eta} - \bar{\eta}(\nabla \cdot \mathbf{v}_{\chi}). \tag{4.24}$$

The first term in the linearized Rossby wave source represents the advection of the basic state absolute vorticity gradient by the divergent wind. This term is initially very large in OFFZON. When the forcing is turned on in the model, the mass source produces a strong divergent wind field, with strong northerlies to the south of the forcing.

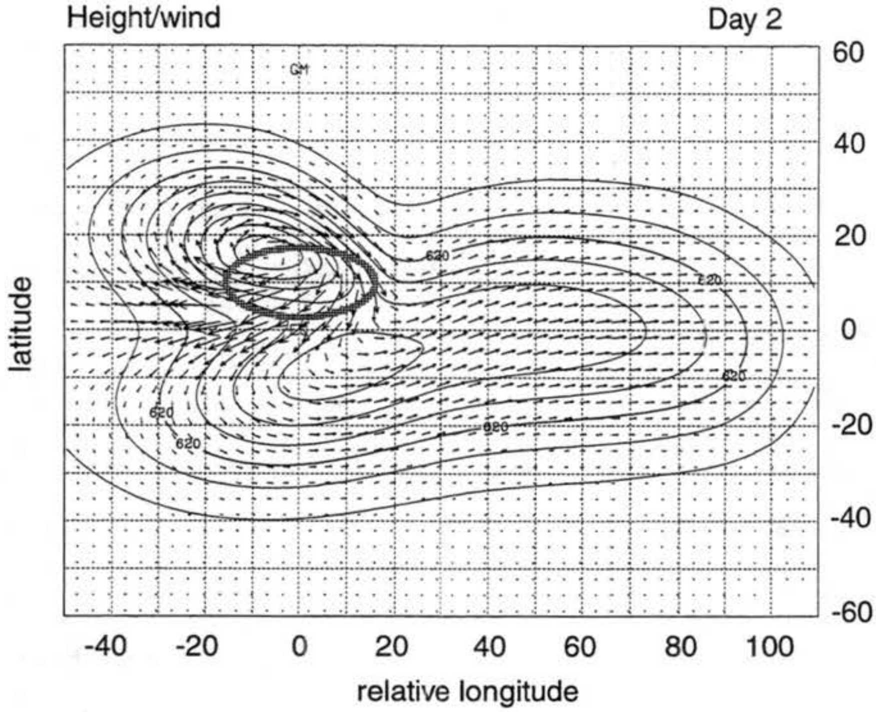

Figure 4.30: Height/wind field on Day 2 for OFFZON.

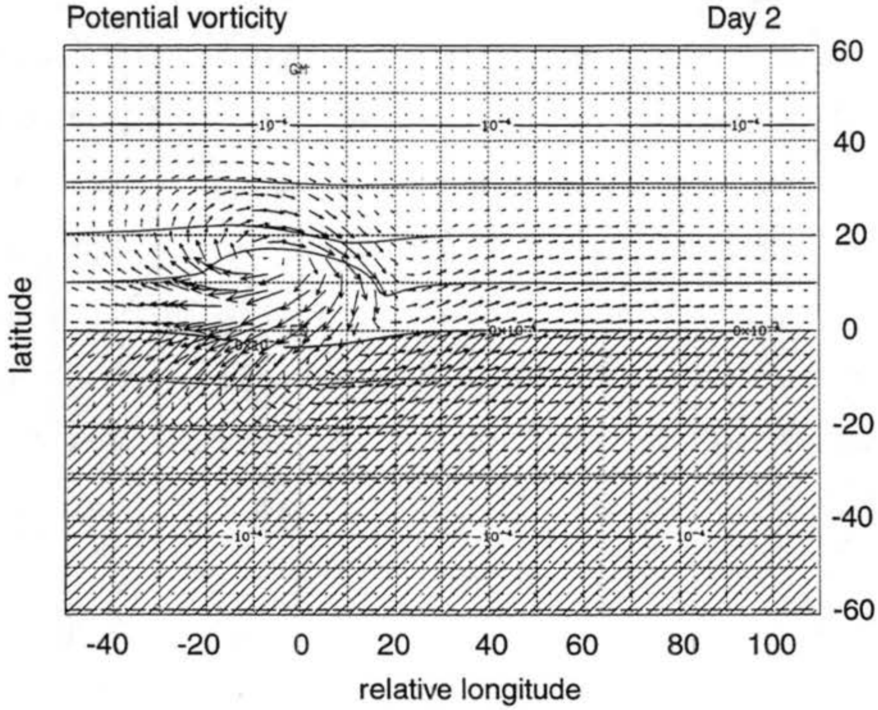

Figure 4.31: Potential vorticity and vector wind fields on Day 2 for OFFZON. Contour interval is 2.5×10^{-5} s^{-1}. Hatched region denotes negative PV values.

These winds are generally perpendicular to the contours of absolute vorticity (Figure 4.31). A significant Rossby wave source is thus created to the south of the forcing, extending into the Southern Hemisphere. This first term in the Rossby wave source transfers energy away from the forcing region to remote areas not directly affected by the mass source. The second term in the Rossby wave source produces Rossby waves locally, inside the region of forcing, where the divergence is strong.

The circulation fields in the shallow water model simulation symmetrize across the Equator through the action of the first term in the Rossby wave source, and eventually behave much like the fields forced by a symmetric mass source, even though the forcing is localized to one hemisphere. The Rossby wave source is able to have such a far-reaching effect because the circulation anomalies produced by the initial vorticity anomaly, which consist largely of divergent winds, extend much farther outward than the vorticity anomaly itself. The wind field can then advect the basic state vorticity gradient and produce additional vorticity anomalies far from the direct source of Rossby waves.

The off-equatorial mass source initially induces a stronger flow toward the Equator than into higher latitudes because the inertial stability of the fluid is smaller near the Equator. This equatorward flow can be likened to the upper tropospheric branch of a localized winter hemisphere Hadley cell. The strength of the cross-equatorial flow in the shallow water model depends on the central latitude of the forcing, such that when the forcing is shifted to a higher latitude, the equatorward winds increase in magnitude. This result is consistent with the zonally symmetric model results of Hack et al. (1989), which show that the cross-equatorial (winter) Hadley cell circulation strengthens considerably when the peak tropical heating is moved off of the Equator.

The circulation fields in the model become more symmetric as the forcing weakens in magnitude. By Day 6, when the forcing has ended, the Northern Hemisphere response remains the stronger of the two, but the height and wind fields have symmetrized such that little cross-equatorial flow remains (Figure 4.32). The cross-equatorial winds are simply a transient response of the fluid as it adjusts to the forcing.

Surprisingly, the Southern Hemisphere height anomalies are stronger in OFFZON than in ZON, even though no forcing exists in the Southern Hemisphere in OFFZON. Large PV anomalies are initially created in the Northern Hemisphere by the off-equatorial forcing in OFFZON, which produces a strong divergent circulation and a large Rossby wave source in the Southern Hemisphere. This Rossby wave source then induces strong PV anomalies in the Southern Hemisphere, which translate into strong height anomalies. Thus forcing in the "summer" hemisphere alone can produce a stronger response in the "winter" hemisphere than forcing which is centered directly on the Equator. Adding the wintertime basic state winds will only augment this effect.

In terms of the zonally-averaged circulation, off-equatorial forcing also produces a different response than equatorially-centered forcing (Figure 4.33). The zonally-averaged zonal wind is accelerated to westerlies poleward of approximately 2°S and 10°N, and to easterlies from 2°S to 10°N. The easterly acceleration is accomplished largely by the mean meridional circulation through an equatorward flux of the zonal mean PV (see Figure 4.31). The westerly acceleration elsewhere is again caused by a combination of the stronger poleward flux of mean PV by the mean meridional circulation and the weaker equatorward flux of eddy PV by the eddies themselves.

Kiladis and Weickmann (1997) provide observational evidence that off-equatorial tropical convection is associated with cross-equatorial winds and double anticyclones. One example is shown in Figure 4.34. Convection in the Southern Hemisphere during austral summer is correlated with strong 200-mb cross-equatorial flow into the Northern Hemisphere and a strong Northern Hemisphere anticyclone. The cross-equatorial flow is produced by the divergent outflow from the convective source; the stronger anomalies in the winter hemisphere are then produced by the Rossby wave source, which becomes large in the Northern Hemisphere because of the strong wintertime meridional vorticity gradient.

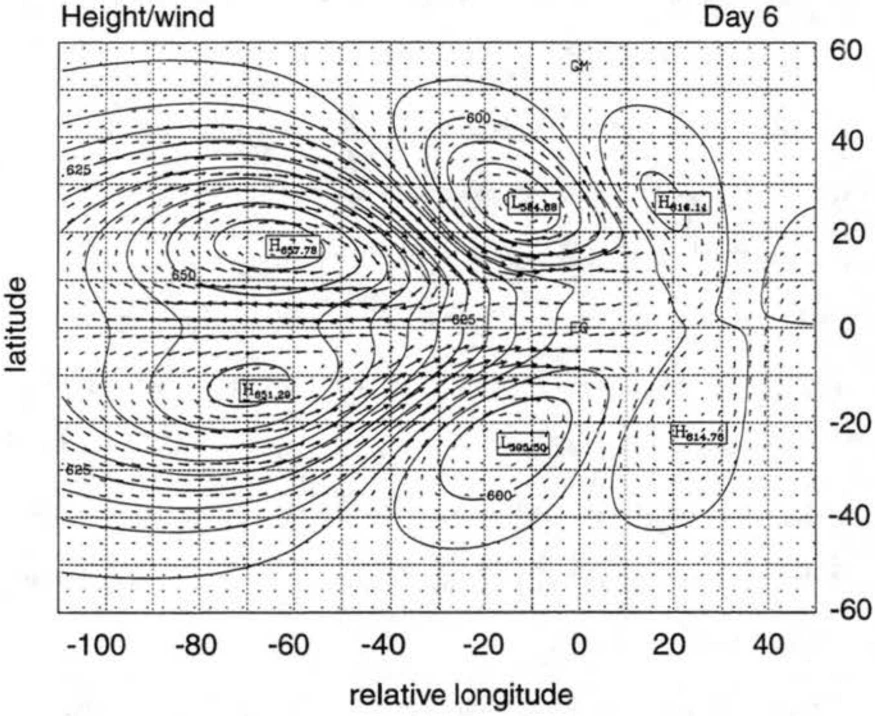

Figure 4.32: Height/wind field on Day 6 for OFFZON.

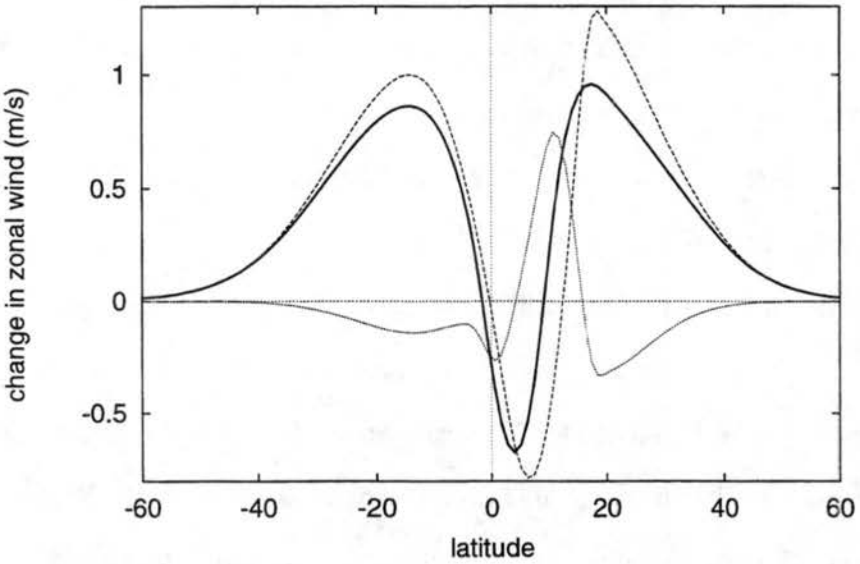

Figure 4.33: Change in the zonal mean zonal wind (thick solid line, in m s^{-1}) and time-integrated forcing by the mean meridional circulation (dashed line) and eddy circulation (dotted line) on Day 6 of OFFZON.

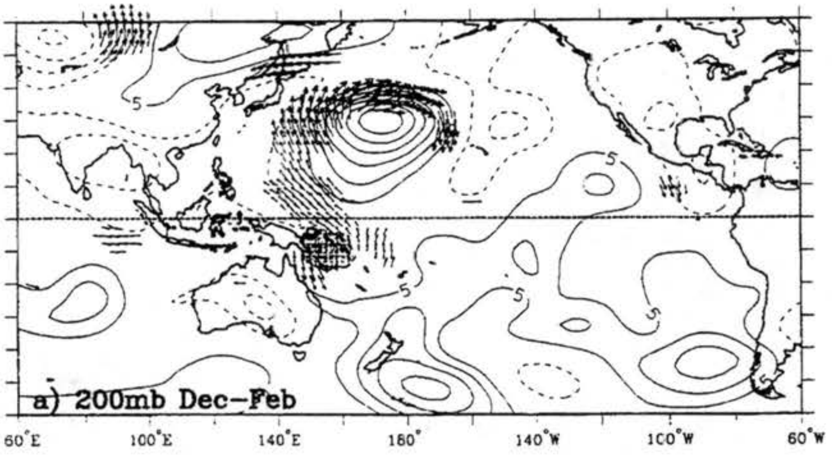

Figure 4.34: The 6–30 day 200-mb streamfunction, wind, and OLR perturbations associated with a -1 standard deviation in OLR in the regions 15°–5°S, 150°–160°E. (From Kiladis and Weickmann 1997.)

4.6 Orientation of off-equatorial forcing

Two simulations were run to determine the effect of the orientation of off-equatorial forcing on the circulation fields. Both simulations are forced with a mass source of shape, size, and location identical to that in OFFZON, but the forcing is rotated either 45° counterclockwise (OFFZON+) or clockwise (OFFZON−).

In both simulations, low PV anomalies are initially produced in the Northern Hemisphere by the mass source. The divergent wind then advects high PV into the Southern Hemisphere, in a similar manner as in experiment OFFZON. These PV anomalies, and the circulations they induce, are of approximately the same magnitude in both simulations. Eastward Rossby wave energy dispersion, however, creates additional PV anomalies which differ greatly between the simulations. When the mass source is rotated counterclockwise, such that the forcing is tilted from southwest to northeast (OFFZON+), the strongest short Rossby wave dispersion occurs to the southeast of the forcing (Figure 4.35). When the mass source is tilted in the opposite direction, from northwest to southeast (OFFZON−), the maximum PV anomalies appear to the northeast of the forcing (Figure 4.36). Short

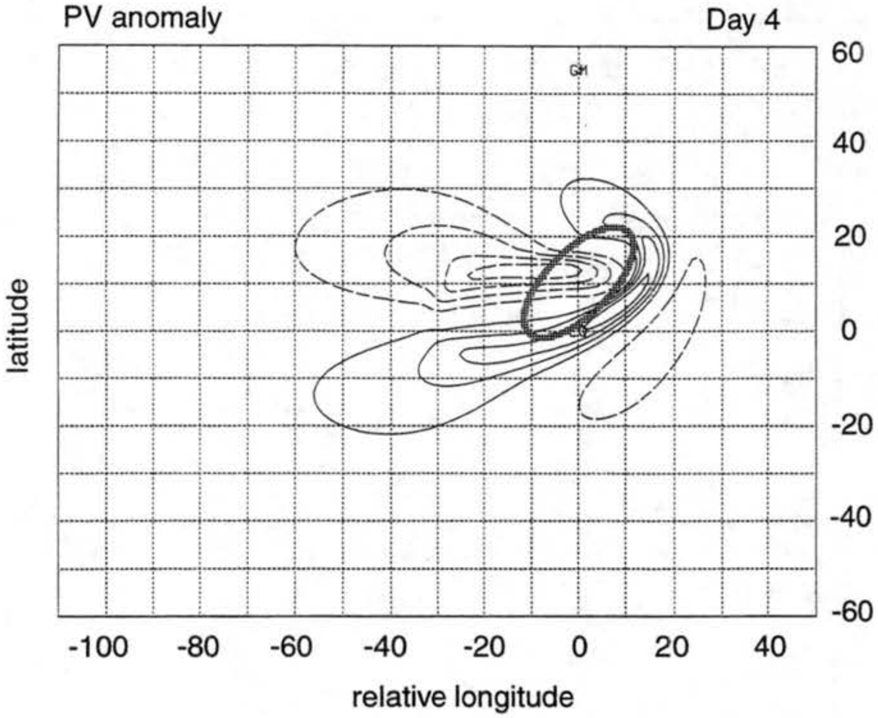

Figure 4.35: PV anomaly field on Day 4 for OFFZON+. Contour interval is 4.0×10^{-6} s^{-1}.

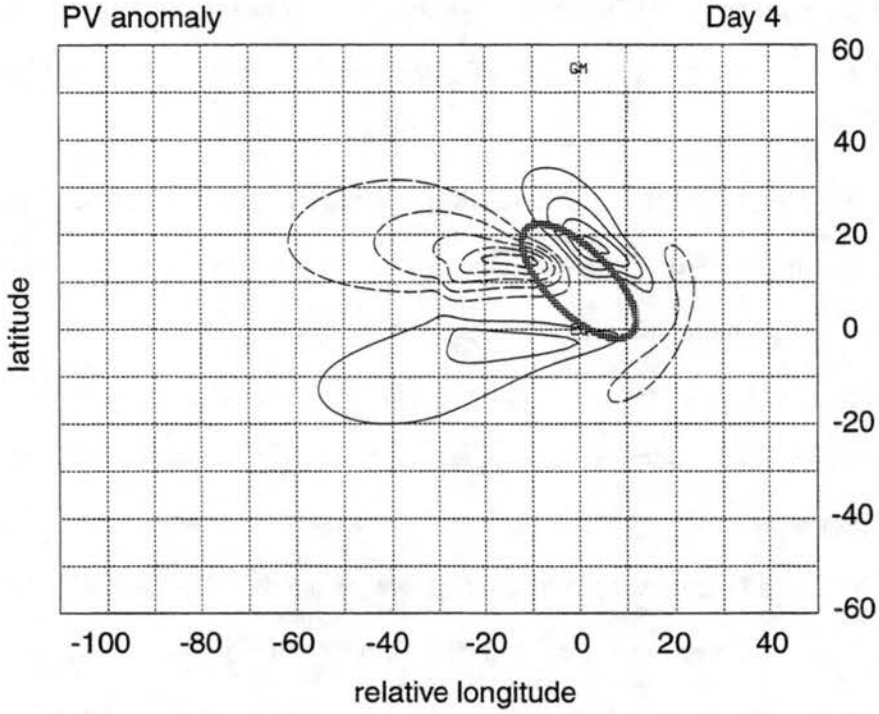

Figure 4.36: Same as Figure 4.35 but for OFFZON−.

Rossby wave dispersion from an elliptical, off-equatorial mass source thus tends to proceed in a direction perpendicular to the major axis of the ellipse.

By Day 6, the height and wind fields are fairly symmetric between hemispheres in both simulations, due to the creation of a Rossby wave source in the Southern Hemisphere. However, differences in circulation strength are still apparent between the different forcing orientations. The strongest short Rossby wave circulations are always located in the Northern Hemisphere for forcing at 10°N; however, these circulations are weakened when the forcing is oriented from southwest to northeast, as in OFFZON+ (Figure 4.37). When the forcing is oriented from northwest to southeast, as in OFFZON−, the Northern Hemisphere short Rossby wave circulations become even stronger than when the forcing is oriented straight east-west (Figure 4.38). Another difference between the two simulations is that the cross-equatorial flow at approximately 10°E is stronger in OFFZON+. Rossby wave dispersion to the southeast of the mass source produces larger PV anomalies to the southeast, which then induce a stronger cross-equatorial flow. Thus the orientation of the off-equatorial convective forcing determines both strength of the cross-equatorial flow and the preferential direction of Rossby wave dispersion, which determines the hemisphere in which the strongest short Rossby wave circulations exist.

4.7 Discussion

The model simulations presented in this chapter have shown that the response of the upper tropospheric circulation to tropical forcing depends on the shape, location, and orientation of the forcing. Many significant circulation features observed in the atmosphere (e.g., Kiladis and Weickmann 1997) can be explained by this simple model.

As was discussed in Section 4.4.4, the model results from the equatorially-centered forcing simulations are most relevant to tropical convection in the Western Pacific during spring and fall, when the upper-level tropical winds are easterly and convection is centered on the Equator. The most significant eastward Rossby wave energy propagation should then

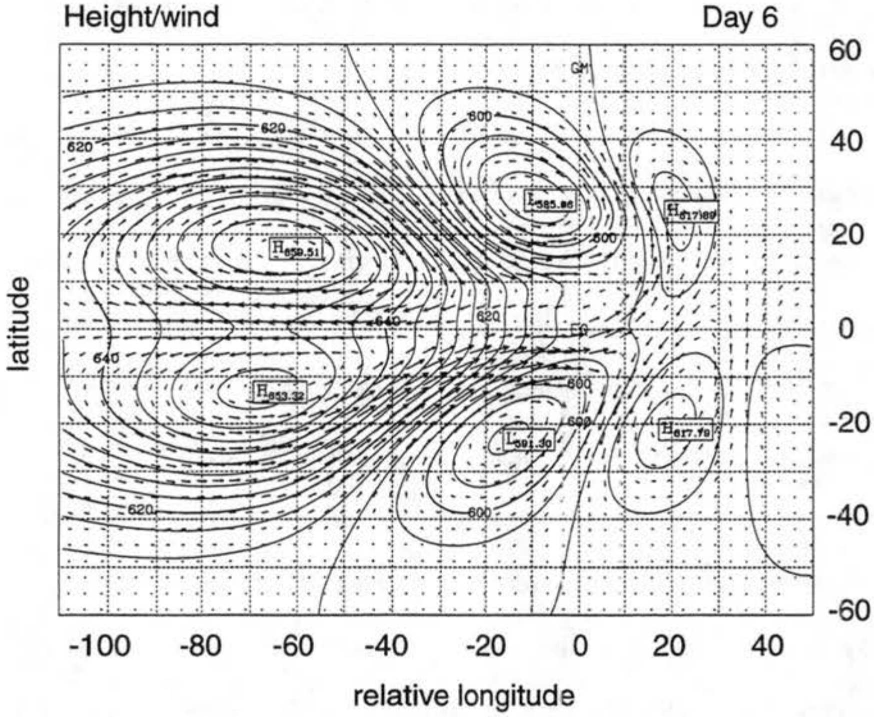

Figure 4.37: Height/wind field on Day 6 for OFFZON+.

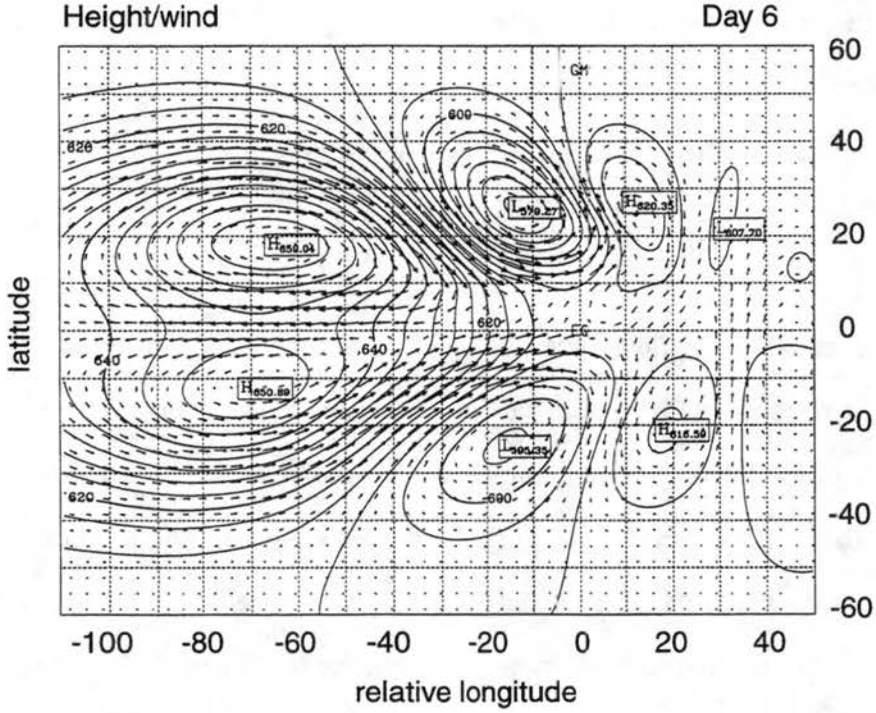

Figure 4.38: Same as Figure 4.37 but for OFFZON−.

occur when the forcing is elongated in the north-south direction. Subtropical westerlies will advect this response substantially to the east, potentially affecting the circulation in the Eastern Pacific and the subtropical regions of the North American continent.

The results presented in this chapter are also relevant to Eastern Pacific convection in the Northern Hemisphere summer, when the upper tropospheric winds are easterly and the convection generally forces the circulation (Kiladis and Weickmann 1997). Eastern Pacific tropical convection is observed to orient itself meridionally, along the Central American coast, during Northern Hemisphere summer (Kiladis 1998). The response of the circulation is thus expected to be very strong, since the convection is not only meridionally elongated in shape, but is located to the north of the Equator and extends into higher latitudes. The upper tropospheric circulation is expected to affect the flow patterns in the Caribbean and the Western Atlantic, which could influence tropical cyclogenesis in those basins. Effects are also expected to be observed in the Southern Hemisphere, because of the Rossby wave source located there in the Southern Hemisphere winter.

In the Eastern Pacific during Northern Hemisphere winter, on the other hand, the upper tropospheric flow is westerly, so the effects of midlatitude forcing are felt much more strongly in the tropics. In this season, observations show that the circulation, in the form of equatorward-propagating wavetrains, tends to force the convection (Kiladis 1998). The association between the convection and the circulation is thus expected to be very different from the model results presented here.

In conclusion, Rossby wave energy dispersion represents one particular mechanism by which energy can be transferred out of the tropics and into the extratropics. The simulations in this chapter have shown that the specific horizontal distribution of tropical convection has a large impact on this energy dispersion process. Thus the statistics of the horizontal distribution of tropical convection should be important in determining the net poleward transport of Rossby wave energy by the atmosphere.

Chapter 5

TIMESCALE OF CONVECTIVE FORCING

One topic left largely unaddressed in the literature to date is the dynamical effect of the timescale of tropical convection on the response of the global circulation. Although individual deep convective storms occur on timescales on the order of only one day, there exist large-scale "envelopes" of convection in the tropics in which a significant average intensity of convection can be sustained for a much longer time period. This chapter contains the results of shallow water model simulations which compare the response of the global circulation to large-scale tropical convective forcing on a number of different timescales.

5.1 Observations

The extratropical circulation patterns associated with tropical convection are observed to depend on the timescale of the convection. For example, Kiladis et al. (1994) show that equatorial convection in the Western Pacific in the 6–30 day band is correlated with a Northern Hemisphere wavetrain which extends to the west of the convection, with a zonal wavelength of approximately 40° (Figure 5.1). On a longer timescale, 30–70 days, the circulation is more zonally elongated, with anticyclones in both hemispheres stretching at least 120° in longitude (Figure 5.2).

In a more general study, Blackmon et al. (1984) show that the spatial structure of observed 500-mb wave patterns in the extratropics also depends on the timescale interval over which the height field is filtered. On long timescales (greater than 30 days), the circulation patterns tend to resemble the "teleconnection" patterns described by Wallace

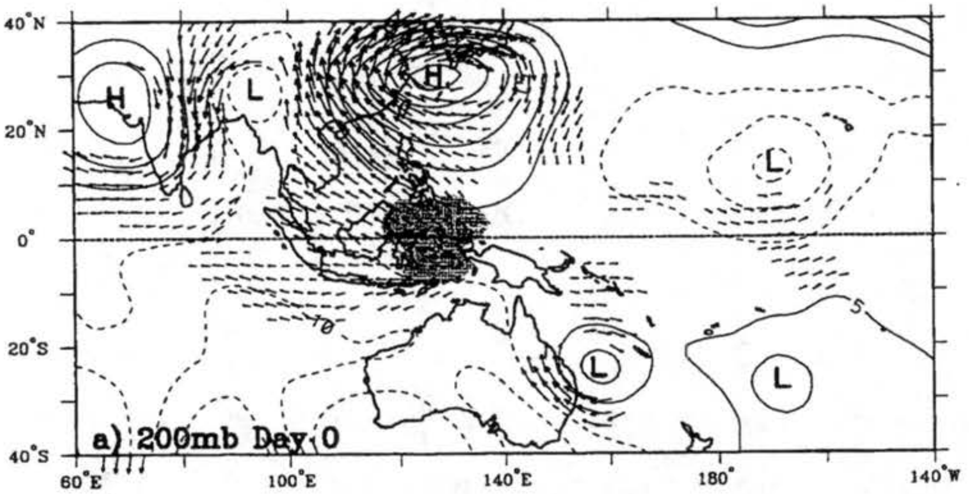

Figure 5.1: Contemporaneous OLR (shading), streamfunction (contours), and wind anomalies (vectors) at 200-mb in the 6- to 30-day band during November–March 1985–1986 through 1991–1992 associated with an area-averaged OLR anomaly of −1 standard deviation in the base region 5°S–5°N, 120°–130°E. (From Kiladis et al. 1994.)

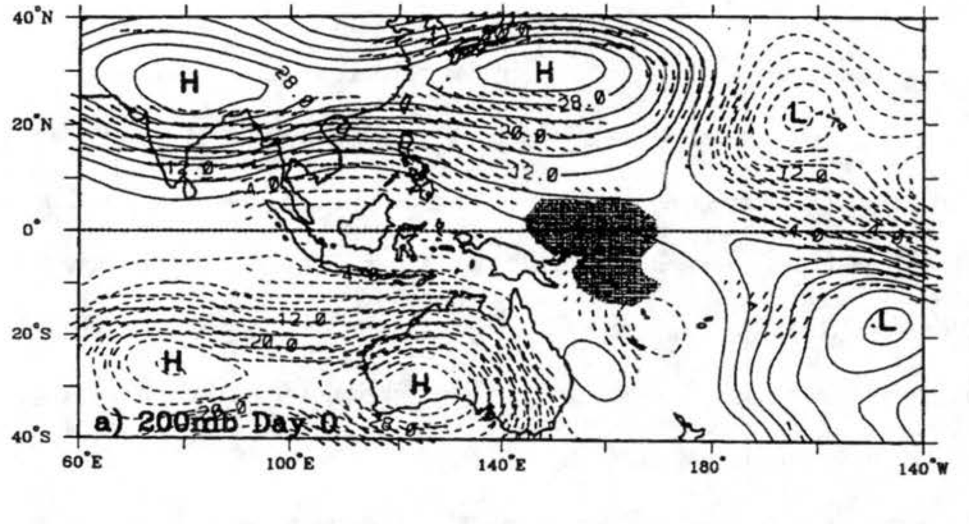

Figure 5.2: Same as Figure 5.1 except for the 30- to 70-day band and an OLR base region of 5°S–5°N, 150°–160°E.

and Gutzler (1981), arcing well into the extratropics along an approximate great circle path. Intermediate timescale filtering (10–30 days) highlights zonally-oriented wavetrains which have a universal shape relative to the basepoint of the correlation, suggesting a Rossby wave dispersion source. Shorter timescale filtering (2.5–6 days) also shows zonally-oriented wavetrains, but of shorter zonal wavelength, of zonal wavenumber 6–7. Although this study does not correlate the extratropical height anomalies with tropical convection, it shows that significant Rossby wavetrain-like patterns exist on a broad range of timescales.

One possible reason for the difference in extratropical circulation patterns among the various timsecales might be that the dominant convective shape changes with the timescale. For example, seasonal averages of tropical convection show concentrated zonally-elongated ITCZ bands, whereas shorter-timescale convection, on the order of a week or so, can take on a much wider variety of shapes (see Figures 4.1–4.4). The simulations presented in Chapter 4 showed that zonally-elongated convection, as might be associated with a longer timescale, tends to produce zonally-elongated extratropical circulation fields. Thus the dominant shape of the convection may influence the long-timescale circulation fields.

This explanation, while plausible, does not address the purely dynamical reasons why the timescale of convective forcing should affect the extratropical circulation. Certainly convective regions of similar shapes and sizes exist in the atmosphere on different timescales, as evidenced in Figures 5.1 and 5.2. This chapter examines the responses of the circulation to these different temporal forcing distributions.

5.2 Model results

The shallow water model is forced with a circular mass source (as in CIRC15) on four different timescales: 3, 6, 9, and 18 days. The temporal distribution of the forcing in each case is given in Figure 5.3. The 6-day forcing simulation, CIRC15, was presented in Chapter 4, and has a midtropospheric peak heating rate in a stratified atmosphere of approximately 12 K day^{-1}. For the 3-day forcing, the heating rate is then doubled, to

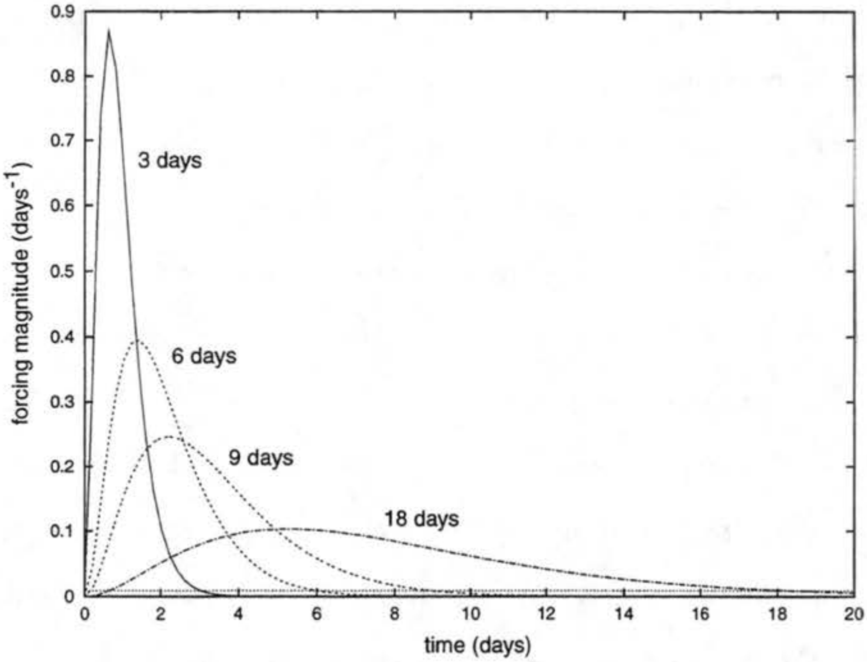

Figure 5.3: Time-dependence of forcing for 3-, 6-, 9-, and 18-day forcing, corresponding to $\alpha = 3.22$, 1.46, 0.91, and 0.45 days^{-1}.

24 K day^{-1}; for the 9-day forcing, the heating rate is decreased to 8 K day^{-1}; and for the 18-day forcing, the heating rate is decreased again, to approximately 4 K day^{-1}. All of these heating rates are within the observed range for the tropical atmosphere, as evidenced by the Q_1 (apparent heat source) data over the TOGA-COARE region presented by Lin and Johnson (1996).

5.2.1 Rossby wave response

The 3-day forcing produces the strongest Rossby wave response in the height and wind fields. By Day 9, eastward Rossby wave dispersion has generated two additional circulation centers to the east of the initial anticylonic anomalies (Figure 5.4). The 6-day forcing (Figure 5.5) also produces two circulation centers through eastward short Rossby wave dispersion, but both are weaker in magnitude than in the 3-day forcing case. The 9-day forcing (Figure 5.6) produces an even weaker response, with one significant downstream closed circulation and a wavy wind pattern to its east.

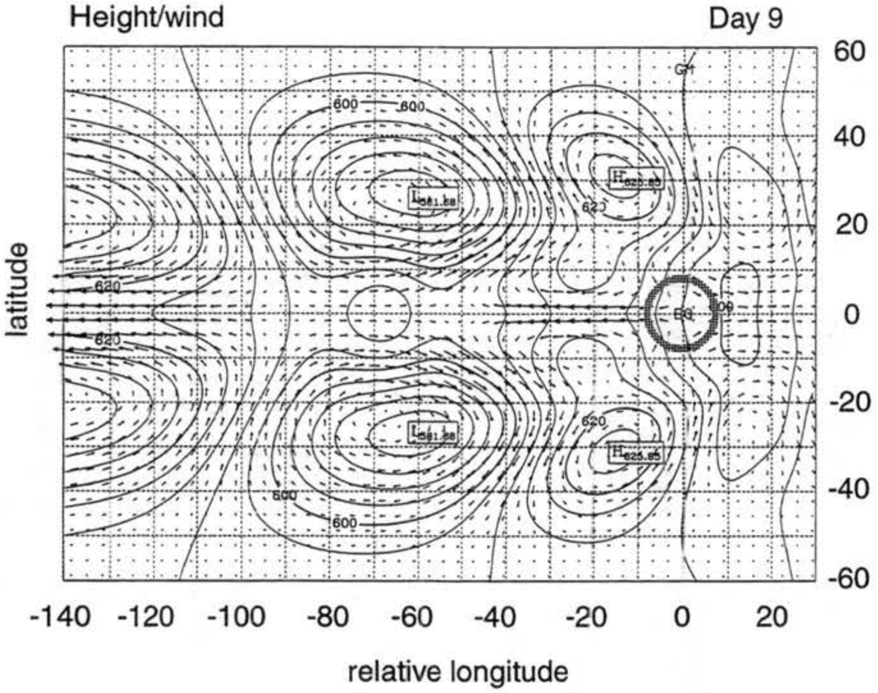

Figure 5.4: Height/wind field on Day 9 for 3-day circular forcing. Contour interval is 4 m. Wind vectors are scaled so that a vector 10° in length represents a 10 m s^{-1} wind. Scaling remains the same in all other figures unless otherwise noted.

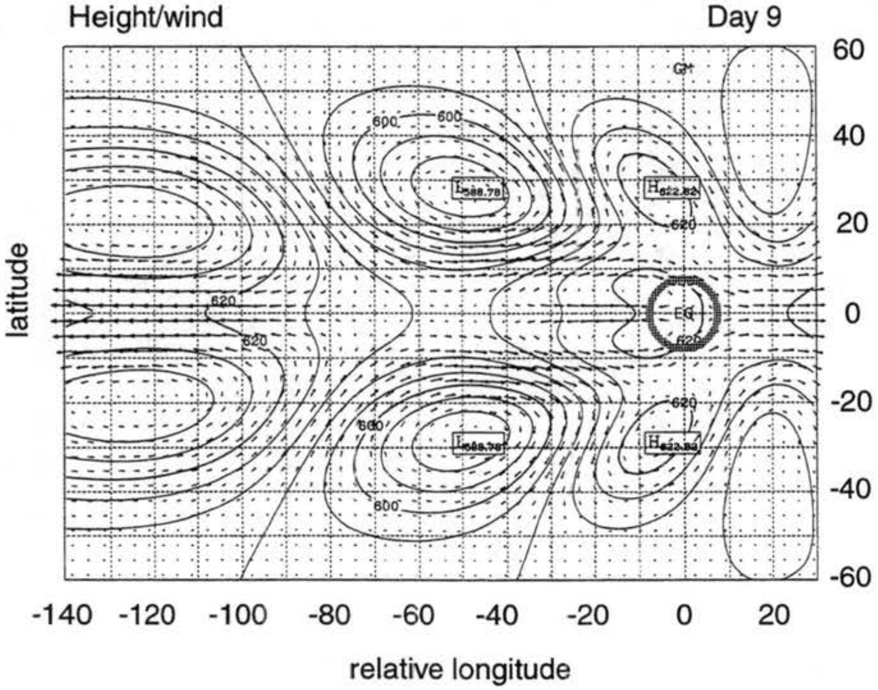

Figure 5.5: Same as Figure 5.4 but for 6-day forcing.

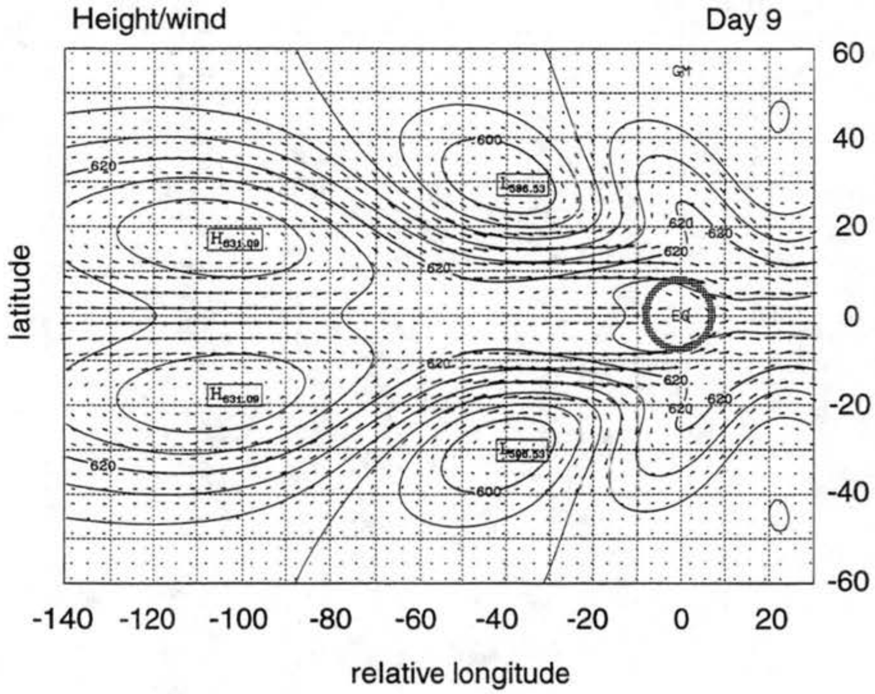

Figure 5.6: Same as Figure 5.4 but for 9-day forcing.

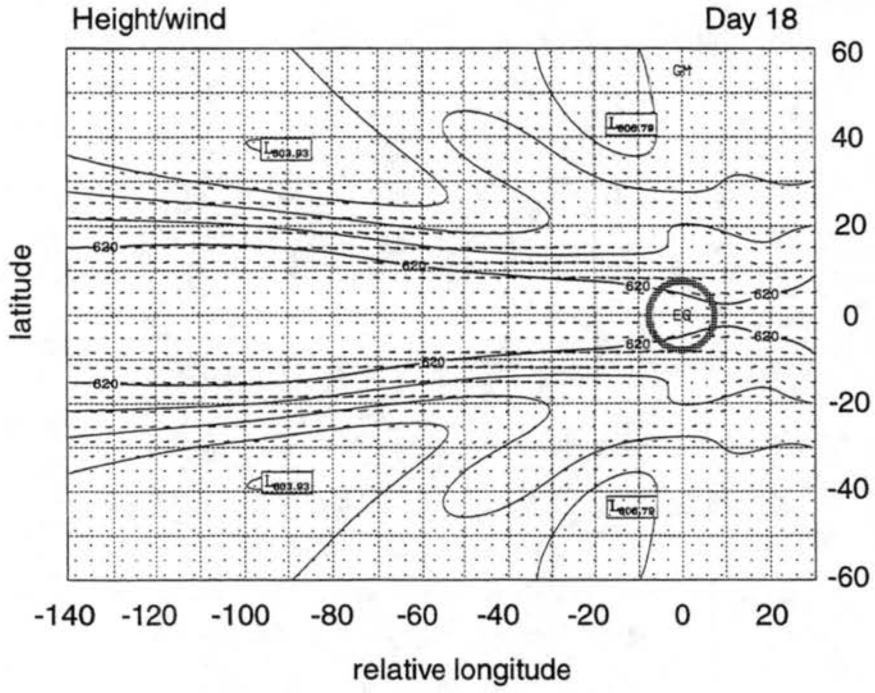

Figure 5.7: Height/wind field on Day 18 for 18-day forcing.

By Day 9 of the 18-day forcing simulation, all of the mass has not been added to the fluid, so the response is of course weaker than in the shorter-timescale experiments. By Day 18, when all of the mass has been added, the circulation is very zonal in character, with elongated westerly wind maxima between 10° and 20° latitude (Figure 5.7). The broader zonal scale of the response in the 18-day forcing experiment compared to the 3-day forcing is reminiscent of the observations presented in Figures 5.1–5.2.

The zonally-averaged zonal wind evolution (not shown) is as expected from Figures 5.4–5.7, with the strongest eddy contribution to the total zonal wind acceleration in the 3-day forcing simulation. Thus the subtropical westerlies are accelerated to the largest magnitude when the forcing is the slowest.

5.2.2 Kelvin wave response

One of the most striking differences among the four simulations is the variation in the strength of the Kelvin wave produced by the forcing. By Day 1 of the 3-day forcing simulation, the Kelvin wave westerlies at the Equator reach 6 m s^{-1}. As the Kelvin wave propagates eastward, it develops a front-like feature with height anomalies of up to 80 m and westerly winds of 10 m s^{-1} (Figure 5.8). This wave propagates at approximately 60° longitude per day, or 77 m s^{-1}, the correct phase speed for a Kelvin wave in a fluid of mean depth 608 m. (This result is qualitatively independent of the method of time differencing. The structure of the front itself differs slightly between the semi-implicit and explicit time differencing schemes.) The strong Kelvin wave circulation field interferes with the Rossby wave circulations as it propagates eastward through the fluid, but since it has no PV signature, it does not make any irreversible changes to their structure.

When the model is forced on a longer timescale, the initial Kelvin wave westerlies are much weaker, since the rate at which mass is added to the fluid is smaller. In the 6-day forcing simulation, these westerlies accelerate to only 3 m s^{-1} by Day 1, and in the 9-day

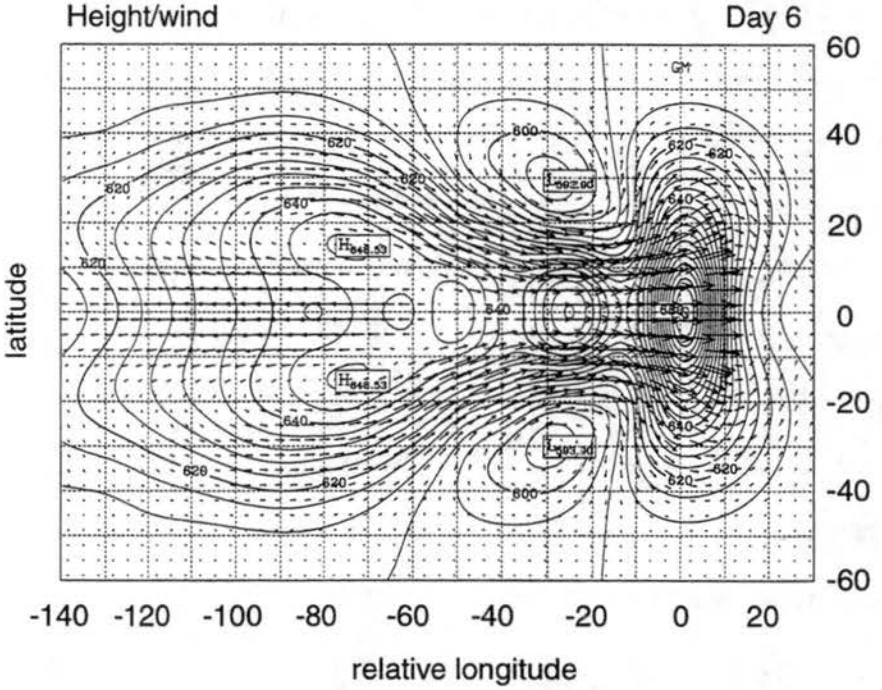

Figure 5.8: Height/wind field on Day 6 for 3-day forcing.

forcing simulation, they barely reach 1 m s^{-1}. The free Kelvin wave response corresponding to Figure 5.8 is also much weaker in the slower forcing timescale simulations.

To further test the hypothesis that the initial Kelvin wave response to the forcing becomes stronger as the timescale of the forcing is decreased, several additional experiments are run on timescales of 3 days or less. An explicit timestepping scheme is implemented, with a timestep of 12 minutes, which satisfies the CFL criterion for the fastest gravity waves. The forcing magnitude, h_0, is lowered to 500 m so that the corresponding peak heating rates are reduced to reasonable values. The physical shape of the forcing remains the same.

Three-day forcing produces the familiar Rossby/Kelvin wave response on Day 1 (Figure 5.9). When the forcing timescale is decreased to 2 days (Figure 5.10), the Kelvin wave westerlies to the east of the forcing increase in magnitude, and the Kelvin wave begins to develop a front-like feature. The Rossby wave circulations remain similar in shape and magnitude to the 3-day forcing. When the timescale is decreased to 1 day, a very different solution emerges (Figure 5.11). The distinct Rossby and Kelvin wave circulations present in

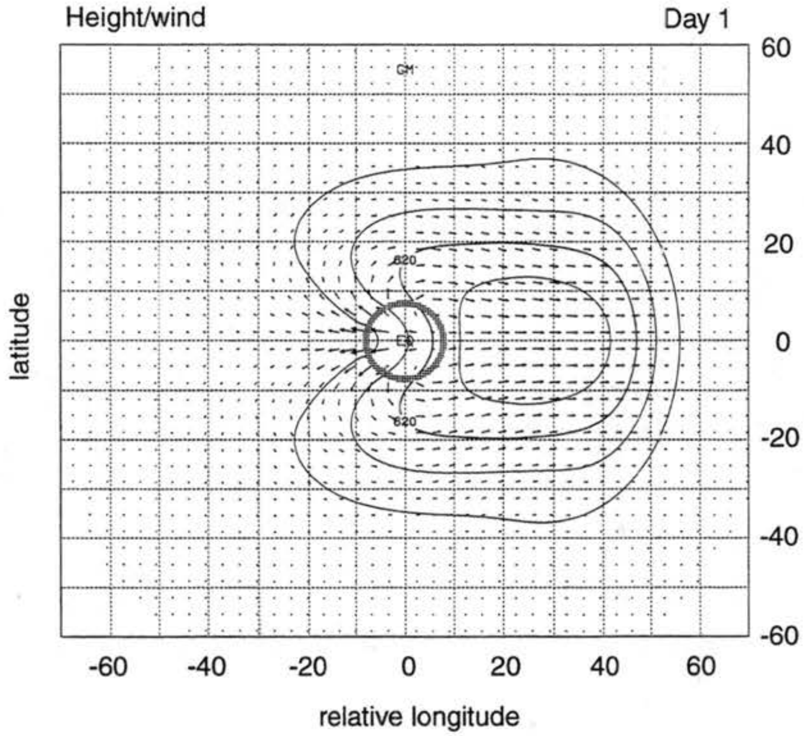

Figure 5.9: Height/wind field on Day 1 for 3-day forcing.

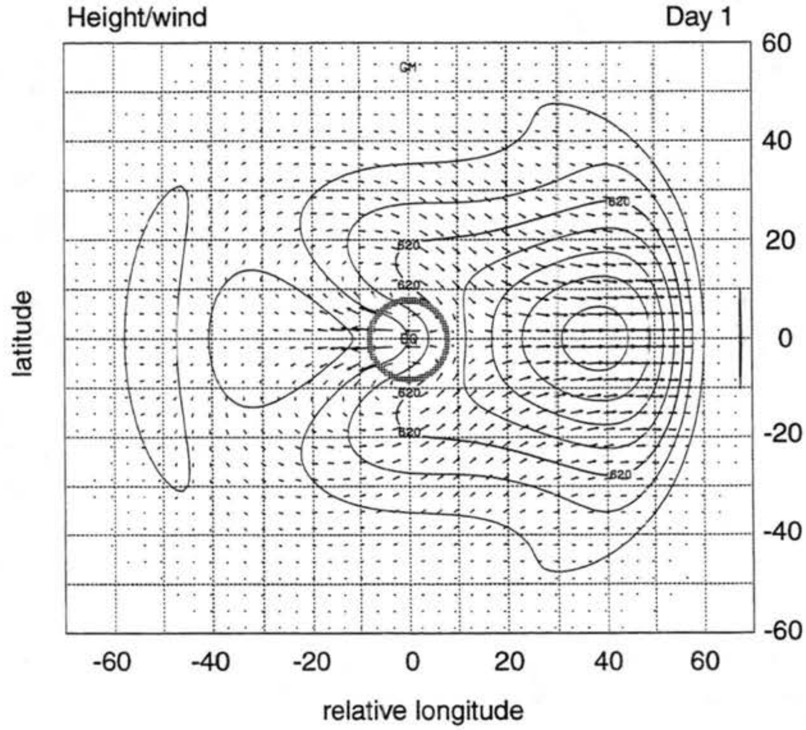

Figure 5.10: Same as Figure 5.9 but for 2-day forcing.

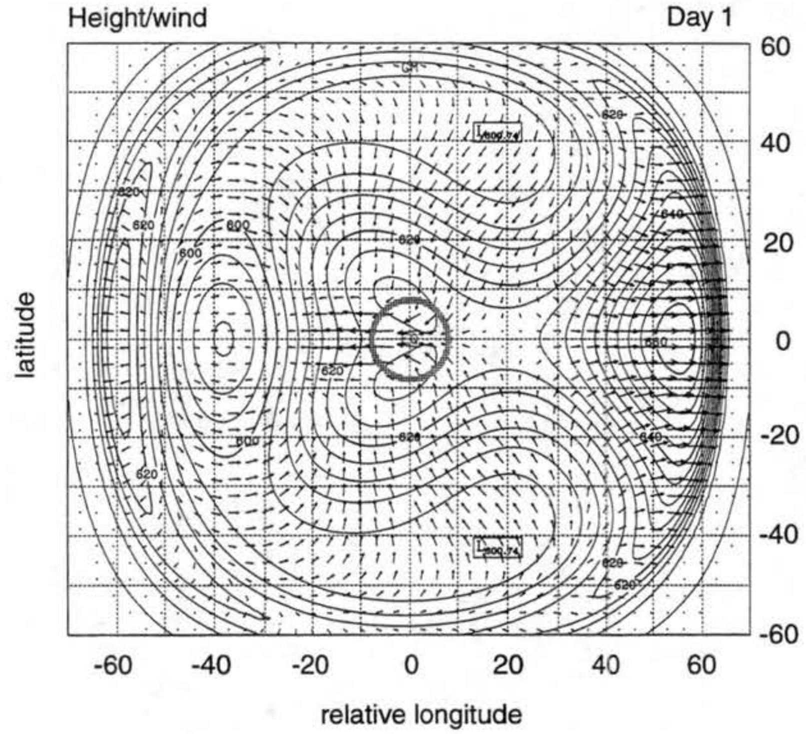

Figure 5.11: Same as Figure 5.9 but for 1-day forcing.

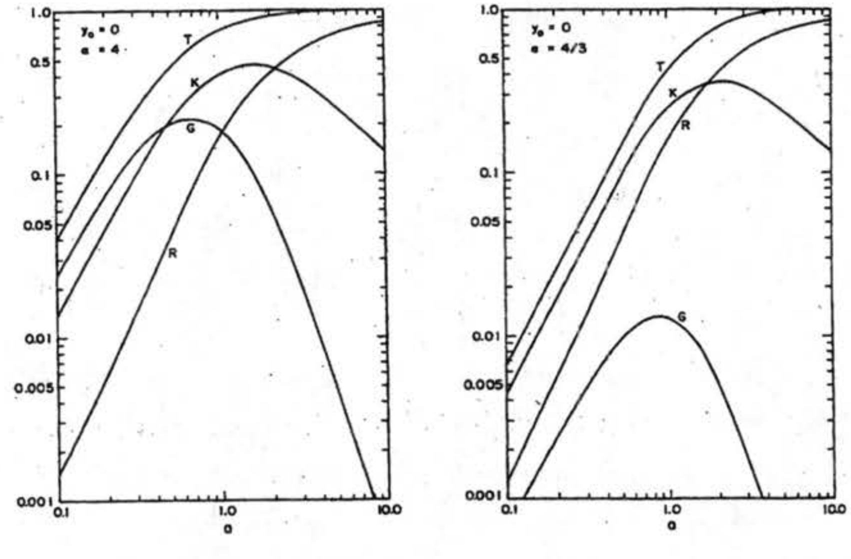

Figure 5.12: Normalized energy partitions for a heat source centered at the Equator for fast forcing (left) and slow forcing (right), as a function of the *e*-folding radius of the heat source, *a*. *T* represents the total energy, *K* the energy partioned to Kelvin modes, *G* to gravity modes, and *R* to Rossby modes. (From Silva Dias et al. 1983.)

the 3- and 2-day forcing experiments are distorted by the strong emission of gravity waves from the forcing region. The combination of the gravity and Kelvin waves to the east of the forcing region produces a very strong wave front, with height anomalies of more than 50 m.

The intensity of this initial Kelvin wave response is much more sensitive to the timescale of the forcing than to the physical shape of the forcing. The forcing shapes used in Chapter 4 (MER, ZON, and ZON60) were tested against the circular forcing, all on a 3-day timescale (not shown). Only very slight differences in the strength of the Kelvin wave response on Day 1 were found among the forcing shapes.

From these simulations and those on longer timescales presented in the previous section, we conclude that both the Kelvin and Rossby wave responses become stronger as the forcing timescale becomes shorter, for timescales down to a limit of approximately 2–3 days. When the forcing timescale decreases below 2–3 days, the fluid response becomes dominated by gravity waves.

In support of this result is a theoretical study of the full shallow water equations by Silva Dias et al. (1983). The two panels presented in Figure 5.12 show the partitioning of energy in a linear shallow water system among the Rossby, Kelvin, and gravity waves as a function of the *e*-folding radius of the forcing, for two different forcing timescales. More energy is partitioned into each of the three modes when the forcing is prescribed on a shorter timescale (left-hand panel), especially for an *e*-folding radius close to the Rossby radius of deformation. In the circular forcing simulations presented in this chapter, the *e*-folding radius of the forcing is approximately one-half the Rossby radius, which should give close to the maximum gravity wave response.

5.2.3 Implications for the Madden-Julian Oscillation

The strength of the Kelvin wave response in the shallow water model has been shown to depend on the timescale of the forcing. When the forcing timescale is short, on the order of 2–3 days, and of large magnitude, representing "impulsive" or "explosive" large-scale tropical convection, the Kelvin wave response attains its maximum intensity. These results suggest that short timescale tropical convection can trigger a very strong wave response in the atmosphere, one which could potentially influence the surrounding circulation and convection fields so as to trigger the onset of a Madden-Julian Oscillation episode.

The MJO is presently thought to consist of a convectively-coupled Kelvin wave (see Lau and Peng 1987, among others). Since the MJO convective envelope is observed to propagate to the east, it was originally assumed to be a pure Kelvin wave phenomenon. However, the phase speed of the MJO is on the order of 5–10 m s^{-1}, whereas a free Kelvin wave in the upper troposphere propagates at approximately 40 m s^{-1}. It has been suggested that the slower phase speed of the MJO results from the coupling of deep convection to the Kelvin wave circulation, which reduces its vertical wavelength and thus slows its eastward propagation speed.

Although the mechanism for the slow eastward propagation of the MJO may be accounted for, the trigger which quasi-periodically initiates the MJO in the Indian Ocean remains unclear. This study may point to a mechanism for such a trigger. If the MJO is indeed composed of a convectively-coupled Kelvin wave, it might be triggered most strongly by intense, short timescale, equatorially-centered convection. The results from the shallow water model simulations point to the emergence of the strongest Kelvin wave response when convection is forced on a 2–3 day timescale. (This result depends on the equivalent depth of the fluid. More discussion on this topic will be presented in Section 5.3.4.) If convection in the Indian Ocean became short-lived, intense, and episodic like this forcing, it could trigger a strong Kelvin wave response, which could then couple with the convection and propagate eastward at the theoretically-predicted coupled speed.

Further substantiating this hypothesis are the coupled ocean-atmosphere general circulation model results of Wang and Schlesinger (1999). The signal of the Madden-Julian Oscillation is the strongest in this model when a high critical relative humidity is implemented in the convective parameterization scheme. This mechanism effectively suppresses convection until the cloud layer mean relative humidity reaches a certain critical value, for example, 90%. A high critical humidity value thus allows energy to store up for longer time periods before convection is allowed to occur. When convection does occur, it should be more intense, or explosive. In the model simulations in which a high critical relative humidity is implemented, the strength of the MJO signal is greatly increased. The Kelvin wave mechanism presented here may account for these model results.

5.3 A nondivergent approximation to the shallow water model

The dynamics of the nonlinear, divergent barotropic model can sometimes be difficult to interpret because of the complexity and interdependence of the underlying equations. In order to more fully understand the results of the simulations presented above, it will be helpful to consider a linearized, nondivergent approximation to the shallow water model equations. Through this method, the shallow water set of three equations can be collapsed into a single equation, which will be analytically solvable. Analysis of this nondivergent analytical solution will assist in understanding the relationship between the frequency of convection and the associated extratropical response in the divergent model. Results will then be shown to be applicable to the stratified primitive equations.

An abbreviated derivation is given below. The full derivation is contained in Appendix A.

5.3.1 Derivation

With several approximations, the absolute vorticity equation in the shallow water system can be solved analytically in spectral space. To begin, the absolute vorticity conservation equation in the shallow water model is:

$$\frac{\partial \eta}{\partial t} + u\frac{\partial \eta}{a\cos\phi\partial\lambda} + v\frac{\partial \eta}{a\partial\phi} + \eta\delta = 0, \tag{5.1}$$

where η is the absolute vorticity and δ is the divergence. The first approximation in deriving the nondivergent analytical solution is applied to the continuity equation:

$$\frac{\partial h'}{\partial t} + \frac{\partial (h'u)}{a\cos\phi\partial\lambda} + \frac{\partial (h'v\cos\phi)}{a\cos\phi\partial\phi} + H\delta = Q(\lambda, \mu, t), \tag{5.2}$$

where h' is the deviation of the fluid depth from the mean depth H, and the mass source/sink Q is given as in equation (3.10). Suppose that this equation can be simplified to:

$$H\delta = Q. \tag{5.3}$$

This approximation neglects the effects of the local time rate of change of the fluid depth and the horizontal advection of mass, and assumes that the mean depth of the fluid is much larger than the deviations. The shallow water model results show this approximation to be reasonable. When (5.3) is substituted into (5.1), the shallow water system is collapsed down to one prognostic equation for u and v.

Further simplifying the system by linearizing about a basic state zonal wind of constant angular velocity $\bar{\omega}$ and constraining the winds to be nondivergent, the vorticity equation can then be expressed entirely in terms of the nondivergent streamfunction:

$$\frac{\partial}{\partial t}(\nabla^2\psi) + \bar{\omega}\frac{\partial}{\partial\lambda}(\nabla^2\psi) + \frac{2\Omega}{a^2}\frac{\partial\psi}{\partial\lambda} = -\frac{2\Omega\mu\tilde{h}}{H}\tfrac{1}{2}\alpha^3 t^2 e^{-\alpha t}. \tag{5.4}$$

The vorticity evolution is controlled by the temporal and spatial forcing when it is active. When the forcing ends, Rossby waves propagate freely on the sphere.

When the above equation is transformed into spectral space, an analytical solution can be derived for $\psi_n^m(t)$, the spectral transform of the physical space streamfunction $\psi(\lambda, \mu, t)$:

$$\psi_n^m(t) = \frac{\alpha^3}{(\alpha + i\nu_n^m)^3} S_n^m \frac{a^2}{n(n+1)} e^{i\nu_n^m t}\{1 - [1 + (\alpha + i\nu_n^m)t + \tfrac{1}{2}(\alpha + i\nu_n^m)^2 t^2] e^{-(\alpha + i\nu_n^m)t}\}, \tag{5.5}$$

where ν_n^m, the spectral frequency, is defined as:

$$\nu_n^m = m\left[\frac{2\Omega}{n(n+1)} - \bar{\omega}\right], \tag{5.6}$$

and S_n^m is the spectral transform of the spatial forcing function $S(\lambda, \mu)$, given by:

$$S(\lambda, \mu) = \frac{2\Omega\mu\tilde{h}(\lambda, \mu)}{H}. \tag{5.7}$$

The notation in the above solution can be simplified by considering the case of very large α, or impulsive forcing. This limiting case approaches an initial value problem. When α is very large, the solution reduces to:

$$\psi_n^m(t) = S_n^m \frac{a^2}{n(n+1)} e^{i\nu_n^m t}. \tag{5.8}$$

The first factor, S_n^m, is dependent only on the spatial distribution of the forcing. The second factor, $a^2/n(n+1)$, is the spectral space inverse Laplacian operator, which tends to smooth out the physical space field by damping the high wavenumber components. The third factor, $e^{i\nu_n^m t}$, is the time-dependent part of the solution, which controls the propagation of Rossby waves. This three-component solution is the simplest case of equation (5.5).

When α is smaller, representing forcing on a finite timescale, the remaining factor in (5.5) becomes significant. This factor is renamed $T_n^m(t)$, signifying the timescale-dependent part of the solution:

$$T_n^m(t) = \frac{\alpha^3}{(\alpha + i\nu_n^m)^3}\{1 - [1 + (\alpha + i\nu_n^m)t + \tfrac{1}{2}(\alpha + i\nu_n^m)^2 t^2]e^{-(\alpha + i\nu_n^m)t}\}. \tag{5.9}$$

With this simplification, (5.5) is rewritten:

$$\psi_n^m(t) = S_n^m T_n^m(t) \frac{a^2}{n(n+1)} e^{i\nu_n^m t}. \tag{5.10}$$

Thus the analytical solution for the streamfunction in spectral space at any time t can be written as the product of four factors: the spatial forcing, the timescale forcing, the inverse Laplacian, and the exponential Rossby wave propagation factor.

5.3.2 Generalization to the stratified primitive equations

The form of the analytical solution derived above is based on the derivation in Silva Dias et al. (1983) for the full set of shallow water equations on an equatorial β-plane. The following nondimensionalized system of equations is solved:

$$\frac{\partial \mathbf{W}}{\partial t} + \mathbf{L}\mathbf{W} = \tilde{\mathbf{W}} \frac{1}{2}\alpha^3 t^2 e^{-\alpha t}, \tag{5.11}$$

where $\tilde{\mathbf{W}}$ represents the spatial dependence of the forcing, and:

$$\mathbf{W} = \begin{pmatrix} u \\ v \\ h \end{pmatrix}, \qquad \tilde{\mathbf{W}} = \begin{pmatrix} \tilde{u} \\ \tilde{v} \\ \tilde{h} \end{pmatrix}, \qquad \mathbf{L} = \begin{pmatrix} 0 & -y & \frac{\partial}{\partial x} \\ y & 0 & \frac{\partial}{\partial y} \\ \frac{\partial}{\partial x} & \frac{\partial}{\partial y} & 0 \end{pmatrix}. \tag{5.12}$$

Note that the time-dependence of the forcing is identical to that in the shallow water simulations described previously.

The solution of this system of equations is:

$$\begin{aligned} W_{m,r}(k,t) &= \frac{\alpha^3}{(\alpha + i\nu_{m,r})^3} \tilde{W}_{m,r}(k) \frac{a^2}{n(n+1)} e^{i\nu_{m,r}t} \times \\ &\quad \{1 - [1 + (\alpha + i\nu_{m,r})t + \tfrac{1}{2}(\alpha + i\nu_{m,r})^2 t^2] e^{-(\alpha + i\nu_{m,r})t}\}, \end{aligned} \tag{5.13}$$

where $W_{m,r}(k,t)$ is the spectral transform of the vector $\mathbf{W}(x,y,t)$. The form of the solution in (5.13) is analogous to (5.5). Thus the nondivergent analytical solution to the approximated shallow water equations is directly analogous to the solution for the full shallow water equations. Since the superposition of the full set of shallow water equations corresponds to the linearized primitive equations for a continuously stratified fluid, the conclusions drawn in the following sections can also apply to a stratified fluid.

5.3.3 Application to divergent model simulations

The dependence on the timescale of the forcing, α, is entirely contained within the $T_n^m(t)$ term in the nondivergent analytical solution [see equation (5.10) and the definition of $T_n^m(t)$ in (5.9)]. The first factor in $T_n^m(t)$, given by $\alpha^3/(\alpha + i\nu_n^m)^3$, represents a filtering on the Rossby wave solution by the timescale of the forcing. Since this factor contains imaginary components, the absolute value is taken:

$$\left| \frac{\alpha^3}{(\alpha + i\nu_n^m)^3} \right| = \left[1 + \frac{(\nu_n^m)^2}{\alpha^2} \right]^{-\frac{3}{2}}. \tag{5.14}$$

This expression is plotted as a function of frequency in Figure 5.13 for two values of α: 0.91 (9-day forcing) and 3.22 (3-day forcing). When α is small, representing forcing on a long

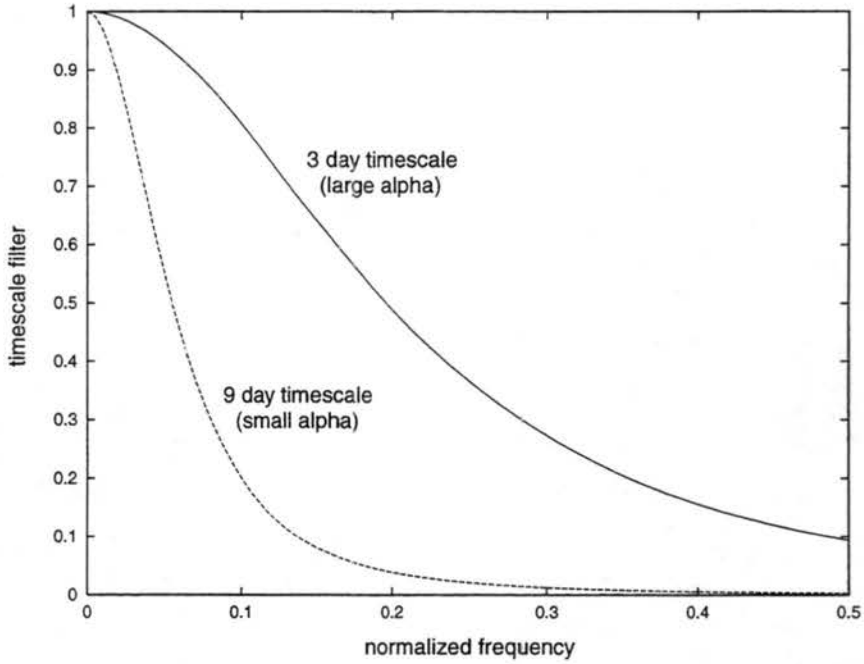

Figure 5.13: Timescale filter in equation (5.14) as a function of normalized frequency $\nu_n^m/2\Omega$ for $\alpha = 0.91$ and 3.22, corresponding to forcing on 9- and 3-day timescales, respectively.

timescale, the filtering function falls off quickly to zero at low frequencies. This represents a strong damping of high frequency Rossby waves by the timescale of the forcing. When α is large, representing short timescale forcing, the filtering function falls off more slowly with frequency. This allows Rossby waves of higher frequencies to be excited at larger amplitudes.

The timescale filter, derived for a nondivergent approximation to one particular set of the shallow water equations, is identical to the filter in Silva Dias et al.'s (1983) solution for the full shallow water equations in (5.13). The filter depends only on the value of α and the frequency of a given wave, ν_n^m, not on the equivalent depth of the fluid. Thus a direct comparison can be made between the timescale filter and the Rossby wave modes in the divergent barotropic wavenumber-frequency diagram.

The effect of the timescale filter is first considered for longer forcing timescales, of 6 days or greater. The 50% line of the timescale filter for 6-, 9-, and 18-day forcing is plotted onto the divergent wavenumber-frequency diagram in Figure 5.14. To the right of

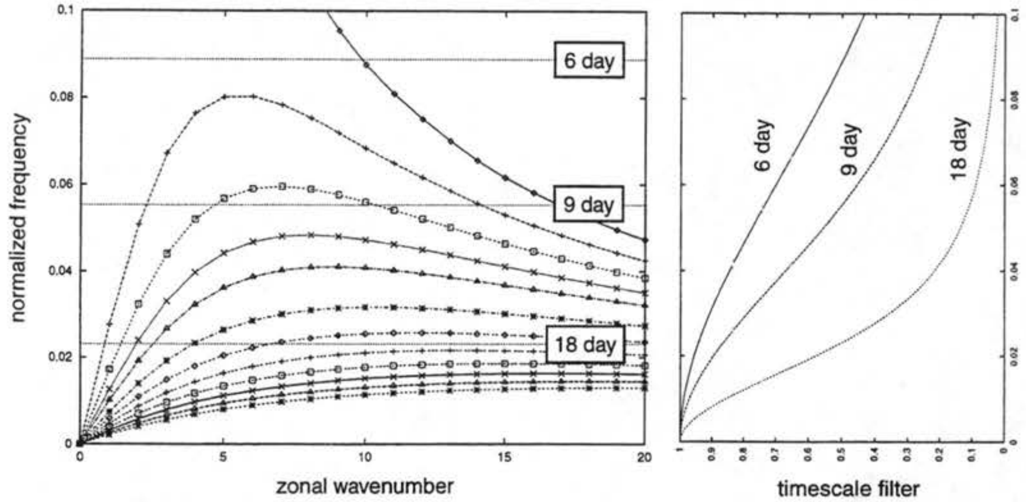

Figure 5.14: Left: Wavenumber-frequency diagram for the divergent barotropic equations of mean depth 608 m, with 50% lines of the timescale filter in (5.14) for 6-, 9-, and 18-day forcing. Curves are arranged by $n - m$ from 0 (top, the mixed Rossby-gravity wave) to 4, then from 6 to 18 in increments of 2. Right: Timescale filter as a function of frequency for 6-, 9-, and 18-day forcing.

the wavenumber-frequency plot is the full timescale filter for these three timescales, so that a direct comparison can be made.

When the forcing lasts for 6 days, all of the pure Rossby modes are forced at greater than 50% of their maximum response. The only waves which are strongly affected by the filter are the longer wavelength mixed Rossby-gravity waves ($n - m = 0$), which are not excited by equatorially-symmetric heating. As the forcing timescale increases to 9 days, the low meridional nodal number Rossby waves become more strongly damped. Many of these filtered waves have large eastward group velocities, especially those of smaller zonal scale (larger m). Thus the filter damps the eastward dispersion of energy into short Rossby waves when the timescale becomes longer than 6 days. This result is clearly seen in the shallow water model simulations, as the circulations to the east of the initial anticyclones are stronger in the 6-day forcing case (Figure 5.5) than in the 9-day forcing case (Figure 5.6).

As the forcing timescale becomes even longer, up to 18 days, the filter has an even stronger effect. The waves which exist at greater than 50% of their peak response are all high meridional nodal number waves with westward or zero group velocities. In the 18-day forcing shallow water model simulation, the response is very zonal in character, which corresponds to low zonal wavenumber (low m), high meridional nodal number (high $n-m$) Rossby waves.

Note also that the timescale filter is independent of zonal wavenumber, so that as the forcing timescale increases, it first filters out the mid-range zonal wavenumber Rossby modes for a given meridional nodal number. This provides a strong scale distinction between the westward-dispersing long waves and the eastward-dispersing short waves. In addition, the shape of the Rossby wave curves in the wavenumber-frequency diagram (steeper positive slopes than negative slopes) allows more of the waves with eastward group velocities than westward group velocities to be damped for a given timescale.

On timescales shorter than 6 days, gravity waves become more important in the response of the fluid. The shallow water model results for very short timescale forcing presented in Section 5.2.1 showed that the Rossby and Kelvin wave responses are overtaken by a strong gravity wave response as the forcing timescale is shortened to one day. This result can be explained by examining Figure 5.15, another wavenumber-frequency diagram for the shallow water equations of mean depth 608 m. This diagram shows all of the equatorial waves predicted by Matsuno (1966), including the Rossby, Kelvin, inertia-gravity, and mixed Rossby-gravity waves. Since the analytical solution for the full shallow water equations derived by Silva Dias et al. (1983) contains the same timescale filter as the non-divergent Rossby wave solution, the filter can be used to interpret the responses of gravity and Kelvin waves as well as Rossby waves. The 50% lines of the timescale filter for 1-, 2-, 3-, and 6-day forcing are plotted in Figure 5.15.

On a timescale of 6 days, all of the Rossby waves can exist at greater than 50% of their peak response. As the timescale becomes shorter, the Rossby waves are less damped by the timescale filter, and thus can exist at larger amplitudes. The Kelvin wave is also affected by the filter, such that as the timescale decreases, waves of shorter zonal wavelength

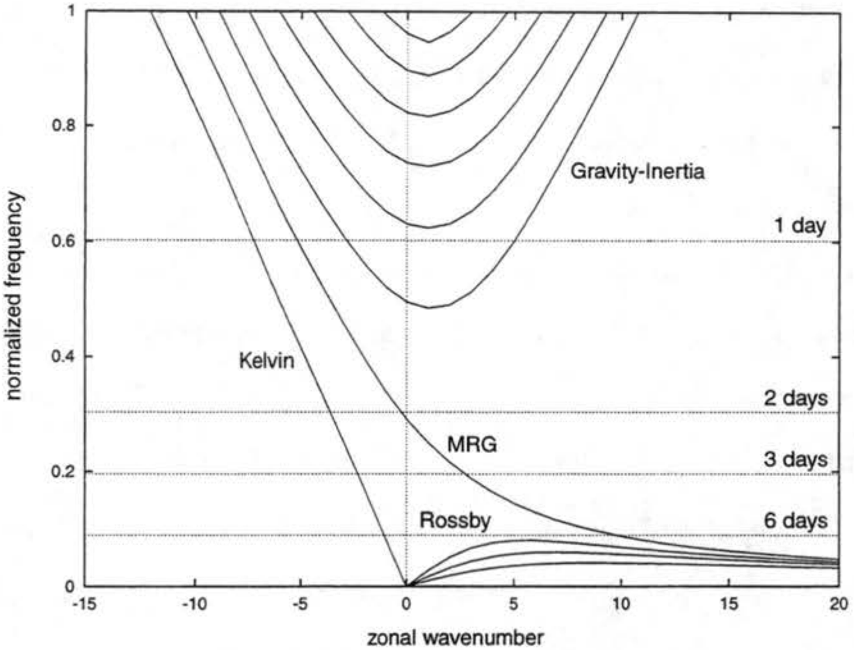

Figure 5.15: Wavenumber-frequency diagram for the divergent barotropic equations of mean depth 608 m with 50% lines of the timescale filter for 1-, 2-, 3-, and 6-day forcing. Positive zonal wavenumbers represent westward phase propagation and negative zonal wavenumbers represent eastward propagation. All wave frequency data provided by Akira Kasahara at NCAR.

can be excited by the forcing. However, the Kelvin wave line on the wavenumber-frequency diagram is so steep that even on a 2-day forcing timescale, only Kelvin waves of zonal wavenumber less than 4 can be excited at more than 50% response. This result helps to explain why only very long Kelvin waves are observed in the upper troposphere.

When the timescale is decreased to 1 day, the 50% line of the filter begins to intersect the gravity wave curves. Thus for 1-day forcing, gravity waves of long zonal and meridional wavelengths can be excited, as seen in the shallow water model results. In addition, Kelvin waves of even shorter zonal wavelength can be excited.

In general, the types of waves which emerge as solutions to the primitive equations depend on the timescale of the forcing. Slow forcing tends to produce a balanced, Rossby wave response, whereas fast forcing triggers a divergent, gravity wave response. The frequency filter presented here simply quantifies this general idea.

5.3.4 Implications for the full stratified atmosphere

For a particular α, corresponding to one specific timescale, the shape of the timescale filter with respect to frequency is fixed. The actual frequencies of the equatorial waves, however, depend on the equivalent depth of the fluid. For a given zonal wavenumber, larger equivalent depths correspond to larger wave frequencies, and smaller depths to smaller frequencies. Since the timescale filter itself does not depend on the equivalent depth of the fluid, it affects the waves associated with each equivalent depth differently. The summation of the responses corresponding to each equivalent depth then approximates the solution to the fully stratified primitive equations.

To compare the frequency curves for different equivalent depths, the approximate Rossby and gravity-inertia wave frequencies ν_r and ν_g, and the exact Kelvin wave frequencies, ν_k, are calculated from the divergent β-plane dispersion relations (Gill 1982):

$$\nu_r \approx \frac{-\beta k}{k^2 + (2n+1)\frac{\beta}{c}}, \tag{5.15}$$

$$\nu_g \approx \pm[(2n+1)\beta c + k^2 c^2]^{\frac{1}{2}}, \tag{5.16}$$

$$\nu_k = kc, \tag{5.17}$$

where k is the dimensional zonal wavenumber, n is analagous to $n - m$ on the sphere, and $c = \sqrt{gH}$. The Rossby wave β-plane formula tends to underestimate the wave frequencies for zonal wavenumbers greater than 5 by about 10% in a 608 m fluid compared to the spherical data of Kasahara. The gravity wave frequencies are slightly underestimated at low zonal wavenumbers and overestimated at high zonal wavenumbers, also by about 10%.

In Figure 5.16, frequency curves for the $n-m=1$ Rossby, gravity-inertia, and Kelvin waves for equivalent depths corresponding to the external and first four internal modes of a stratified fluid are presented. The equivalent depth for each vertical mode was calculated from the phase speeds given in Fulton and Schubert (1985). The Rossby wave portion of this figure is enlarged in Figure 5.17.

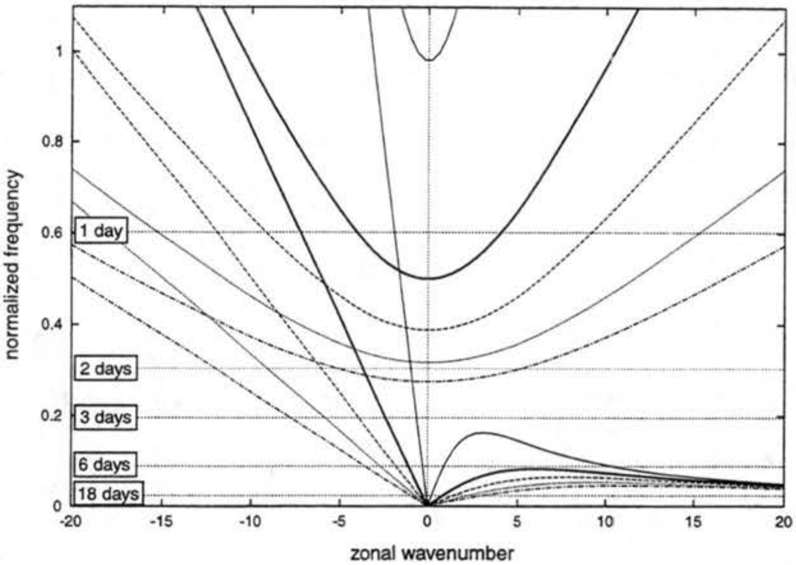

Figure 5.16: Wavenumber-frequency diagram comparing the $n - m = 1$ Rossby, gravity-inertia, and Kelvin wave curves for mean fluid depths of 8970 m (solid lines), 608 m (dark solid), 222 m (dashed), 98 m (dotted), and 56 m (dot-dash), representing the external mode and the first four internal baroclinic modes of a stratified fluid, respectively. Horizontal lines represent the 50% lines of the timescale filter for forcing timescales of 1, 2, 3, 6, and 18 days.

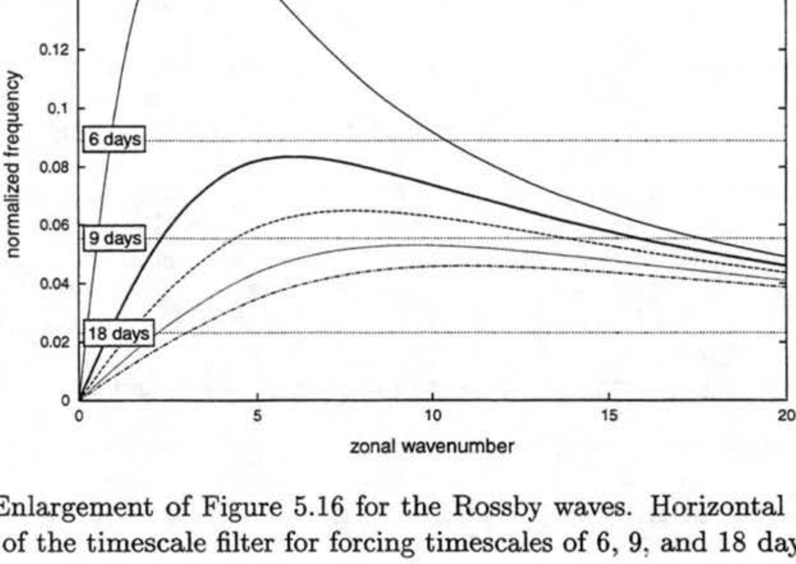

Figure 5.17: Enlargement of Figure 5.16 for the Rossby waves. Horizontal lines represent the 50% lines of the timescale filter for forcing timescales of 6, 9, and 18 days.

In terms of the actual frequencies of the waves, the equivalent depth of the fluid affects the gravity and Kelvin wave curves more strongly than the Rossby wave curves (Figure 5.16). This result can also be seen in the dependence of the wave frequencies on c in the dispersion relations (5.15)–(5.17). Since Rossby waves are nearly nondivergent, the equivalent depth of the fluid does not affect the frequencies as strongly as in the more divergent gravity and Kelvin waves.

In relation to the timescale filter, however, the equivalent depth significantly affects all three types of waves. For example, when the timescale of the forcing is longer than two days, the majority of the gravity wave response is suppressed in the larger equivalent depth fluids. In the shallower fluids, however, the low zonal wavenumber gravity waves can exist. In other words, a small equivalent depth fluid can support gravity waves on a longer forcing timescale than a large equivalent depth fluid. The forcing timescale also determines the maximum zonal wavenumber of the gravity waves. For example, when the timescale is decreased to one day, only the longest gravity waves can exist in deeper fluids, whereas shallower fluids can support much shorter waves.

The effect of the timescale filter on Rossby waves depends most strongly on the equivalent depth when the forcing timescale lies between 6 and 18 days. The filter again suppresses more of the wave spectrum at a given forcing timescale when the equivalent depth is large. Referring to Figure 5.17, a forcing timescale of 9 days will allow the third and higher internal modes to be forced at greater than 50% of their peak response, but will filter out much of the external mode and first two internal modes.

The Kelvin wave's dependence on the timescale filter and equivalent depth determines the maximum zonal wavenumber which can be forced in the fluid on a given timescale. In deeper fluids, only the longest Kelvin waves can be excited, in a similar manner to the gravity waves. As the fluid becomes shallower, shorter wavelength Kelvin waves can be excited by the forcing.

In the 608 m equivalent depth simulations, the maximum Kelvin wave response was shown to exist for the 2- to 3-day forcing timescale. This frequency band lies in the region on the wavenumber-frequency diagram above the 50% filter for the first internal mode Rossby waves, and below the 50% filter for the first internal mode gravity-inertia waves. It is possible that forcing on this particular timescale appropriates the maximum amount of wave energy to the Kelvin modes because it lies in between the Rossby and gravity modes. As the equivalent depth becomes smaller, this frequency band which lies between the Rossby and Kelvin waves becomes narrower, and exists at longer forcing timescales. The maximum Kelvin wave response may therefore exist at longer timescales for smaller equivalent depth fluids. Thus the dominant vertical structure of the forcing may determine the timescale at which Kelvin waves can be most efficiently excited.

Since the linearized stratified atmosphere corresponds to the summation of all of these shallow water modes, the total response in a stratified atmosphere will be influenced both by the timescale of convection and its dominant vertical mode. The timescale filter presented here suggests that very long timescale heating in the atmosphere should not efficiently excite low vertical mode responses (i.e., the external mode, the first baroclinic mode). Short timescale heating, on the other hand, can excite large equivalent depth Rossby waves as well as small equivalent depth Rossby and gravity waves. However, it is important to remember that the total response of the atmosphere depends also on the imposed vertical structure of the forcing, which is determined by the vertical profile of heating by both deep and shallow tropical convection.

5.4 Conclusions

The simulations in the previous chapter illustrated that the shape and location of convective forcing localize the wave response of the atmosphere to a certain region of the wavenumber-frequency diagram. Zonally-elongated forcing pushes the response toward the lower left of the diagram, where the group velocities are westward, whereas meridionally-elongated forcing pushes the response toward the upper right, where the group velocities are eastward. The results in Chapter 5 have now shown that the timescale of the forcing also tries to localize the response on the wavenumber-frequency diagram. Long timescale forcing pushes the response toward the bottom of the diagram, to the low-frequency waves. Shorter timescale forcing allows the response to broaden into the higher frequency Rossby waves and gravity waves. In a continuously stratified atmosphere, the response also depends on the dominant vertical mode of the forcing. It is the combination of these three different factors, the shape of the convection, its timescale, and its vertical structure, which produce the final response seen in the atmosphere.

Chapter 6

BAROTROPIC INSTABILITY OF THE ITCZ

Often during the Northern Hemisphere summer, a number of Pacific tropical cyclones form in the vicinity of the ITCZ in a short time frame, on the order of a week. Ferreira and Schubert (1997) proposed that this observation could be explained by the barotropic instability of an off-equatorial, lower tropospheric ITCZ. They suggest that ITCZ convection itself creates the environment for its own breakdown into individual tropical cyclones.

This argument implies that ITCZ convection creates a very dynamically active lower troposphere, with significant PV mixing as a result of the barotropic instability process. The question then arises, is the same true of the upper troposphere? Deep convection in the tropics removes mass from the lower troposphere and deposits in the upper troposphere, thus providing an equal but opposite forcing on these two levels in the atmosphere. We wish to determine whether the upper tropospheric flow will break down through barotropic instability in a similar manner to the lower troposphere.

We then combine these barotropic instability concepts with the convective shape experiments presented in Chapter 4 to investigate a localized phenomenon in the Western North Pacific. Lander (1996) observes that tropical cyclones in the Western North Pacific preferentially move on northward and S-shaped tracks during episodes of a "reverse monsoon trough," when the trough is oriented from southwest to northeast. We propose that the formation of these tropical cyclones can be explained by the barotropic instability and axisymmetrization of a localized convective region, and that their subsequent propagation direction depends on the orientation of the monsoon trough.

6.1 Lower and upper tropospheric instability

6.1.1 Background

Ferreira and Schubert (1997, hereafter referred to as FS) show through both free and forced shallow water model simulations that a lower tropospheric, off-equatorial ITCZ can break down into a number of tropical cyclone-like vortices through the barotropic instability mechanism. In the free (initial condition) experiments, the model is initialized with a zonally symmetric strip of high absolute vorticity, centered at 10°N. Observationally, lower tropospheric regions of high (potential) vorticity similar to this are documented in the Northern Hemisphere summer over the Caribbean, in the Eastern Pacific, and over continental Africa, extending westward into the Eastern Atlantic (Molinari et al. 1997). The model then calculates the nonlinear balanced wind and mass fields from this vorticity profile, which creates an initial shear layer. This horizontal shear profile represents the zonal mean ITCZ winds, with easterlies (tradewinds) to the north and westerlies to the south. The shear across the ITCZ is approximately 15 m s^{-1}. The vorticity strip is then perturbed with a weak wavenumber 13 disturbance, since wavenumber 13 was found by FS to be the most unstable mode in a nondivergent, linear normal mode stability analysis. The shear layer breaks down into distinct, coherent cyclonic vortices by Day 15.

The mechanism for the breakdown of the initial shear layer is barotropic instability. The high vorticity strip creates a negative meridional gradient of absolute (and potential) vorticity on its poleward side, which satisfies both the Rayleigh-Kuo necessary condition for barotropic instability in a nondivergent flow and Ripa's (1983) analogous condition for divergent flow. The initial perturbations to the strip then grow by extracting energy from the mean flow. The rate of breakdown of the vorticity strip is shown to be dependent on the intensity of the added vorticity, and the zonal wavelength of the unstable mode is dependent on the width of the strip.

Since the ITCZ is in general not zonally symmetric, but instead consists of several distinct regions of frequent deep convection (e.g., Africa, the Western and Eastern Pacific), FS also ran forced shallow water simulations to determine whether a localized ITCZ could break down into individual tropical cyclones. The shallow water model was forced in a similar manner to the convective shape simulations in Chapter 4, with an elliptical, zonally-elongated, off-equatorial mass sink (dimensions are 100° × 8°, centered at 10°N) which acts for 5 days. As in the initial condition experiments, the forced ITCZ also breaks down into distinct cyclones.

In the forced case, a reversal in the meridional gradient of PV is created on the poleward side of the mass sink. According to the PV conservation equation (4.1), a mass sink located entirely within the Northern Hemisphere will produce a positive PV anomaly. On the poleward edge of the mass sink region, then, the PV gradient becomes negative, and the flow again satisfies the necessary condition for barotropic instability.

6.1.2 Initial condition experiments: zonally symmetric ITCZ

Ferreira and Schubert (1997) considered the effect of ITCZ convection on the lower tropospheric circulation. Here we investigate the question: can the same mechanism for breakdown act in the upper troposphere?

Initial condition experiments are run for both lower and upper tropospheric cases. The vorticity strip is centered at 10°N, is 4.5° latitude in width, and has an intensity of 3.0×10^{-5} s^{-1}. The vorticity in the strip is added to the basic state absolute vorticity in the lower tropospheric simulation, and subtracted in the upper troposphere. The vorticity jump at the edges of the strip is smoothed by the same exponential function as in the convective shape experiments, given by (3.16), with $\gamma = 200$. Figures 6.1 and 6.2 show these initial vorticity profiles. Although the initial absolute vorticity in the upper tropospheric case dips below zero, inertial instability does not occur in the model simulations. (A simulation in which the vorticity strip is moved to 15°N (not shown), so that the vorticity remains positive

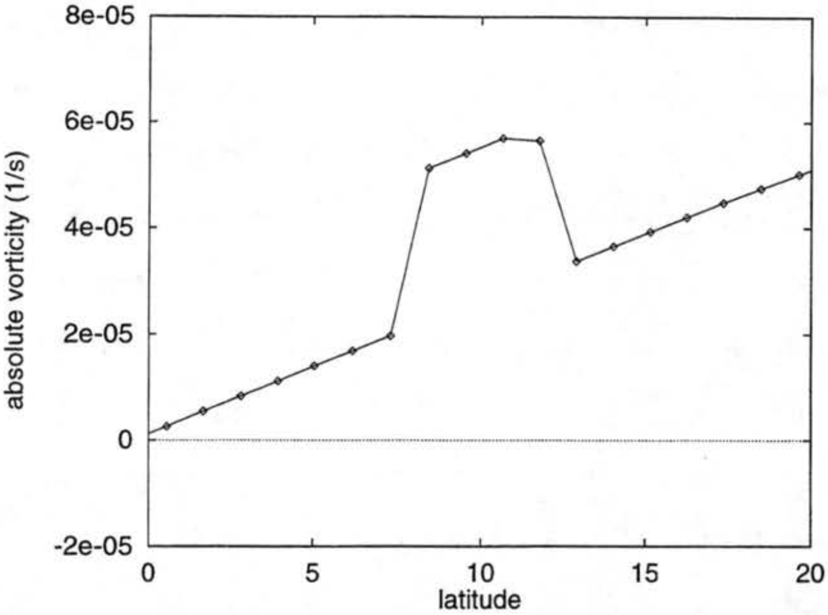

Figure 6.1: Initial profile of absolute vorticity in the lower tropospheric initial condition barotropic instability experiment. Points are the Gaussian latitudes in the spectral model.

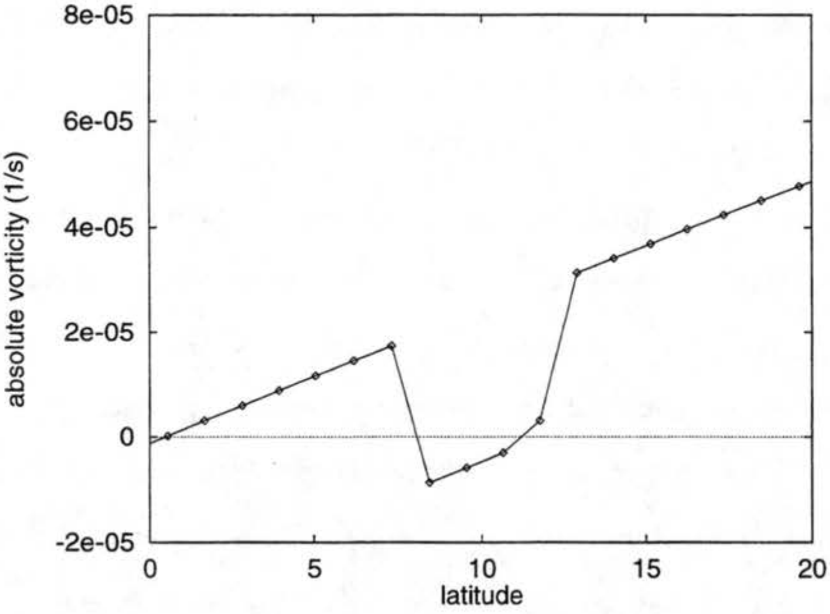

Figure 6.2: Same as Figure 6.1 but for the upper tropospheric experiment.

in the Northern Hemisphere, produces qualitatively similar results.) The magnitude of the shear in both cases is approximately 15 m s^{-1}.

The initial shear layers break down in both the lower and the upper tropospheric simulations. Figures 6.3 and 6.4 show the height/wind fields on Day 15, after the vortices have grown considerably from the initial perturbations. Two distinguishing features are immediately apparent: 1) the vortices have larger height perturbations in the lower troposphere than in the upper troposphere, and 2) the flow has a larger meridional component (is "wavier") to the south of the vortices in the lower troposphere, and to the north of the vortices in the upper troposphere.

The cyclonic and anticyclonic winds around the vortices in the lower and upper troposphere, respectively, are of approximately the same magnitude, since the magnitude of the shear is the same in both simulations. Gradient wind balance around a single vortex predicts that the height gradient will be larger for a cyclonic vortex than for an anticyclonic vortex. Thus the cyclonic vortices require a larger height perturbation to sustain the circulation imposed by the breakdown of the shear region.

To explain the second feature, FS present an analytical solution to an idealized approximation of the vorticity strip. They conclude that the absolute value of the meridional vorticity gradient determines the amplitude of the Rossby wave solution. In the lower troposphere, the meridional gradient of absolute vorticity is larger on the southern edge of the strip than on its northern edge. Of the two sets of Rossby waves which counterpropagate along these two strong vorticity gradients, the amplitude of the westward-propagating waves along the southern edge of the strip are larger. Thus the induced flow fields are "wavier," i.e., they include larger meridional wind components, to the south of the strip. In the upper troposphere, by analogy, the waves on the northern edge of the strip will have larger amplitudes, since the meridional vorticity gradient is larger there. Thus in the upper troposphere, the flow fields are wavier to the north of the strip.

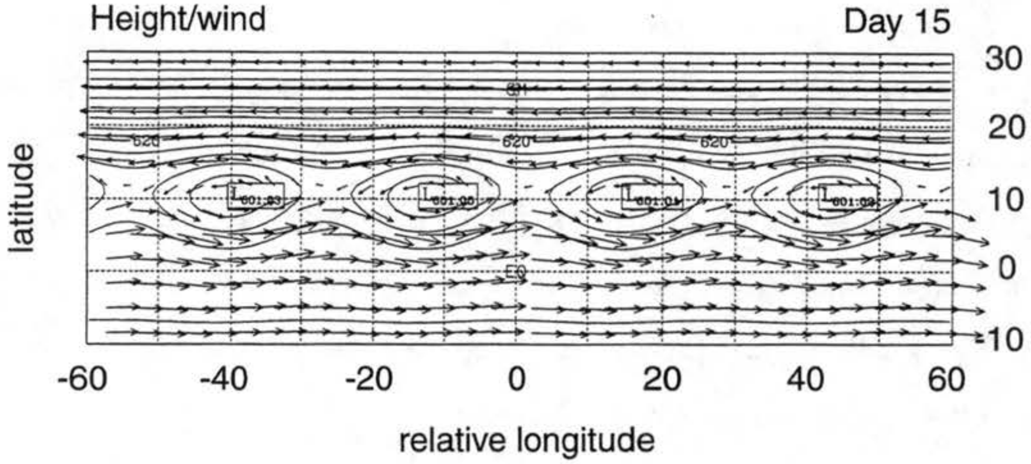

Figure 6.3: Height/wind on Day 15 for the lower tropospheric initial condition barotropic instability experiment. Height contour is 4 m. Vector winds are scaled such that a vector 10° in length represents a 10 m s^{-1} wind.

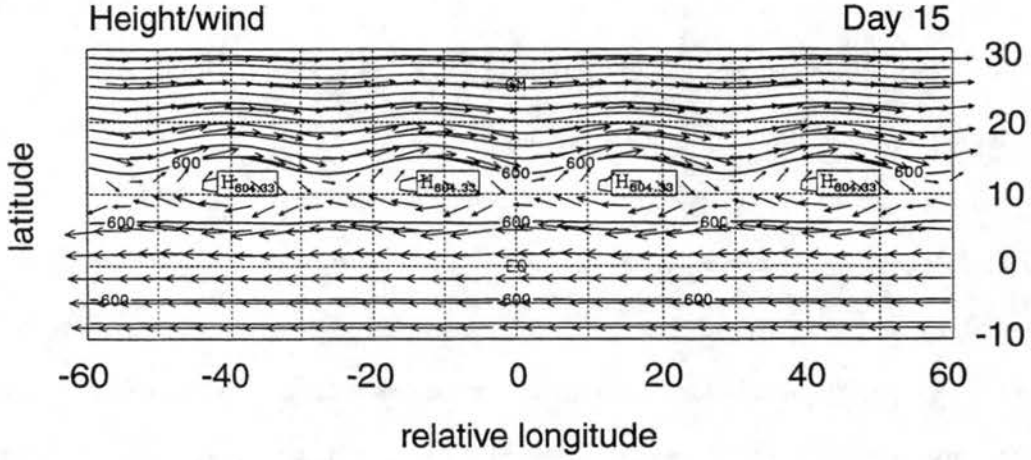

Figure 6.4: Same as Figure 6.3 but for the upper troposphere.

Kuo (1973) predicted theoretically that the phase speeds and growth rates for disturbances growing from the breakdown of a barotropically unstable shear layer should be independent of the sign of the shear. The nonlinear results presented here, however, disagree with this prediction. Although the growth rates seem to be comparable in magnitude (this is difficult to determine from the model output), the phase speeds of the unstable modes are not equal. The upper tropospheric waves propagate westward at approximately 4 m s^{-1}, whereas the lower tropospheric waves propagate westward at about half that speed, 2 m s^{-1}.

6.1.3 Forced experiments: localized ITCZ

Tropical convection does not realistically occur in a zonally symmetric strip around the entire tropical troposphere, but is localized into smaller longitudinal bands of convection. To simulate this more localized convection, FS force the shallow water model with a mass sink, in a similar manner as the model runs presented in Chapter 4. The particular forcing shape and size chosen are intended to represent convection over the Pacific basin.

To compare the results of forced lower and upper tropospheric simulations in the shallow water model, the FS lower tropospheric simulation is first rerun with the model parameters changed to be consistent with the rest of the simulations in this study. The mean depth is changed from 222 m (FS) to 608 m. The mass forcing is given by (3.10), where h_0 is -700 m, or approximately 7K day^{-1}. This value of h_0 gives approximately the same maximum forcing, scaled by the mean depth of the fluid, as in FS. The timescale of forcing is changed to 6 days, or $\alpha = 1.46$ days^{-1}. The spatial forcing remains the same: the mass sink is elliptical, with half-widths in the zonal and meridional directions of 60° and 5°, respectively.

Results from this simulation are similar to the results in FS. A meridional reversal in the PV gradient is produced on the poleward edge of the mass sink, satisfying the necessary condition for barotropic instability. By Day 4, a broad cyclonic circulation has formed

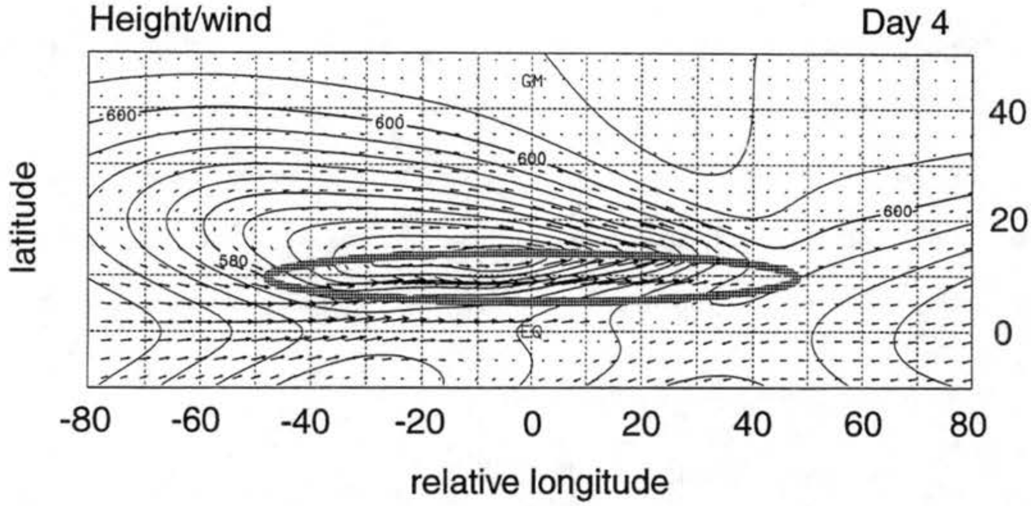

Figure 6.5: Height/wind field on Day 4 for the forced lower tropospheric ITCZ experiment. Height contour is 4 m. Vector winds are scaled such that a vector 5° in length represents a 10 m s^{-1} wind. Scaling remains the same for all forced barotropic instability simulations.

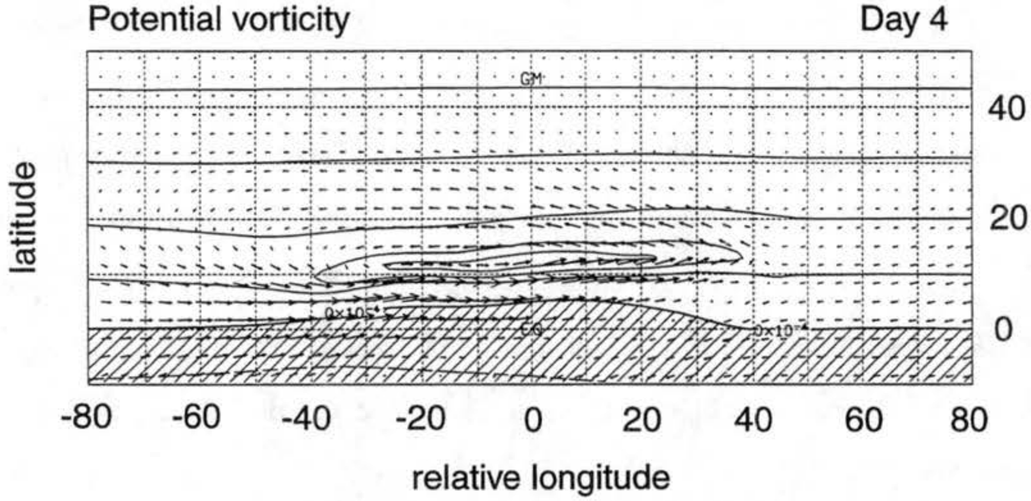

Figure 6.6: Potential vorticity field on Day 4. Contour interval is 2.5×10^{-5} s^{-1}.

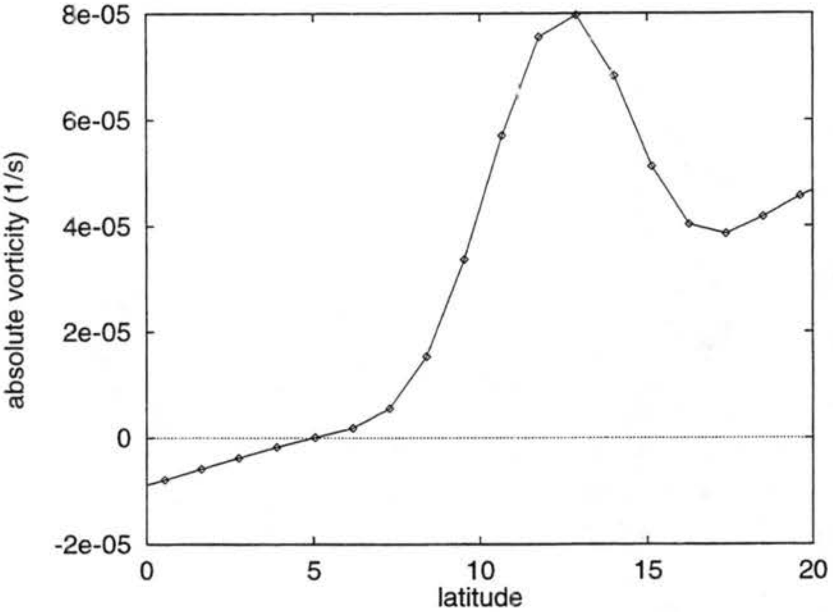

Figure 6.7: Meridional profile of absolute vorticity (in s^{-1}) at 0° relative longitude on Day 4 for the forced lower tropospheric ITCZ experiment.

(Figure 6.5), with easterlies to the north and westerlies to the south of the forcing. This creates a shear zone surrounding the region of the forcing. A region of high PV, with a negative meridional gradient on its poleward side, is located in the region of the mass sink (Figure 6.6). The meridional profile of absolute vorticity for the forced experiment is similar in shape and magnitude to that prescribed in the initial condition experiment (Figure 6.7).

By Day 10, barotropic instability has created three distinct cyclonic circulations from the initially broad shear zone (Figure 6.8). These intense circulation centers are produced as the PV field redistributes itself through the barotropic instability process, pooling the high PV into small regions (Figure 6.9). The high PV in these regions mixes with the lower PV in the surroundings, such that the meridional gradient of PV eventually becomes single-signed.

These model cyclonic vortices can be thought of as analogous to tropical disturbances or tropical depressions, i.e., the precursors to tropical cyclones, which are constrained mainly to the lower troposphere. Although the model does not produce full-fledged tropical storms

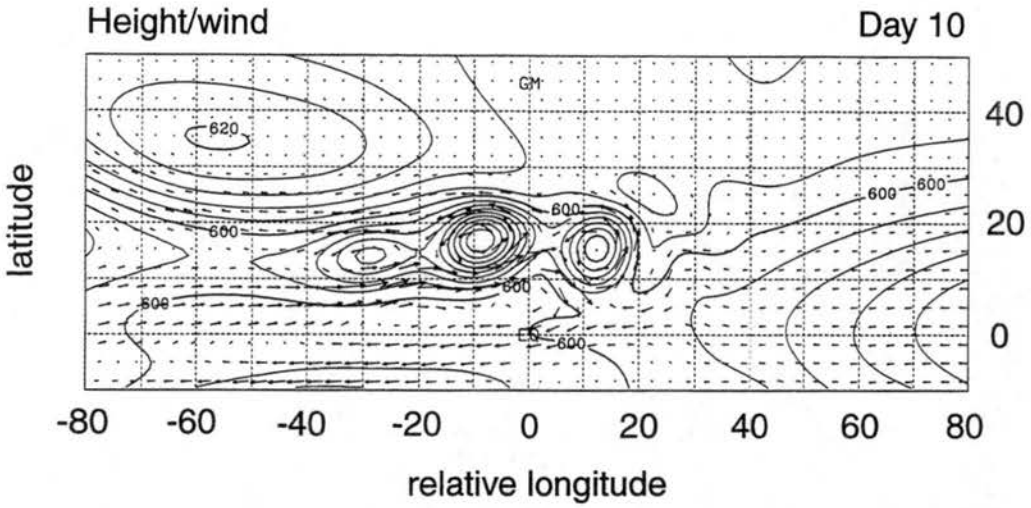

Figure 6.8: Height/wind field on Day 10 for the forced lower tropospheric ITCZ experiment.

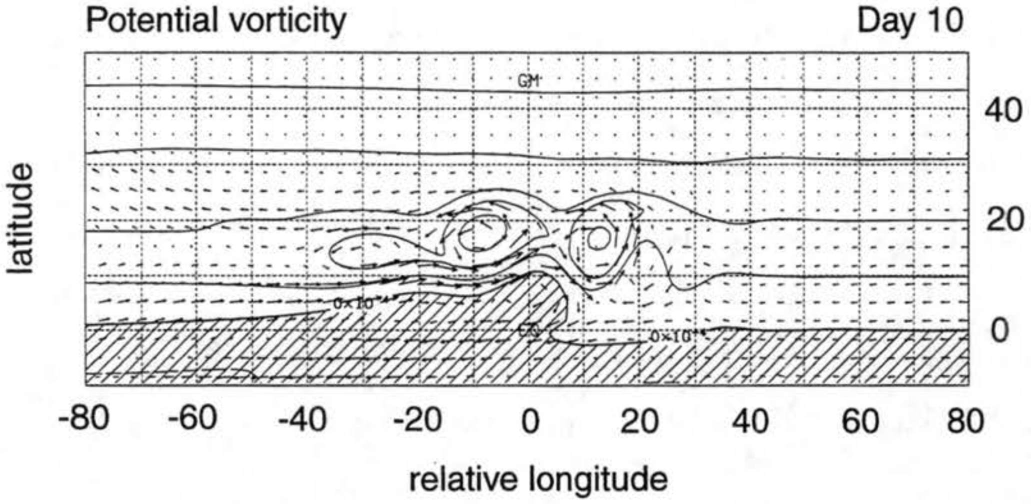

Figure 6.9: Potential vorticity field on Day 10. Contour interval is 2.5×10^{-5} s^{-1}.

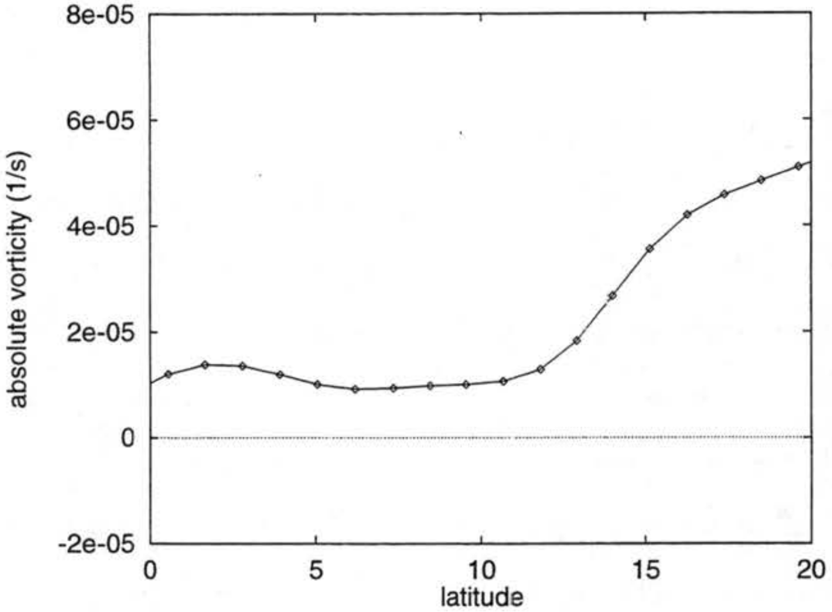

Figure 6.10: Meridional profile of absolute vorticity (in s^{-1}) at 0° relative longitude on Day 4 for the forced upper tropospheric ITCZ experiment.

(cyclonic winds in the model cyclones reach only 10 m s^{-1}), it provides a mechanism by which these initial cyclonic vortices can form. In the real atmosphere, these vortices can then grow in strength through moist physical processes, which are not included in the model.

A similar experiment is then run to simulate the effect of ITCZ convection on the circulation of the upper troposphere. All parameters are identical to the lower tropospheric simulation, except that the spatial forcing constant h_0 is positive instead of negative, representing a mass source instead of a mass sink.

The results in the upper troposphere are drastically different from those in the lower troposphere. By Day 4, the mass source has produced only a very weak negative vorticity gradient at 5°N (Figure 6.10), far from the large gradient prescribed in the initial condition experiment. From this result alone, one would expect barotropic instability in the forced simulation to be very weak or nonexistent. By Day 6 the low PV region develops localized minima, indicative of the barotropic instability process. These centers of low PV are very small and weak, however, and induce only weak anticyclonic circulations in the wind/height field. Figures 6.11 and 6.12 show these small circulation centers and the corresponding PV anomalies on Day 10.

As was discussed in Chapter 4, the mass source cannot produce a large PV anomaly (and thus a large meridional absolute vorticity gradient) because it becomes less "efficient" with time [see equation (4.13)]. The fact that the mass source becomes less efficient with time means that the flow must be forced more strongly in the upper troposphere to produce the same shear magnitude as in the lower troposphere. In addition, no matter how strong the forcing in the upper troposphere becomes, the absolute vorticity in the region of the mass source will never become negative. As Q increases, the PV decreases toward zero more quickly in time, but it will never drop below zero. Thus the barotropic instability process simulated in the upper tropospheric initial condition experiment is not a realistic depiction of the effects of convection on the upper troposphere. The shear magnitude initialized in the model is impossible to create with a mass source placed at 10°N, since the forcing cannot create a negative PV anomaly in the Northern Hemisphere.

The forced shallow water model experiments, as the more realistic of the two sets of experiments, have shown that ITCZ convection produces a very dynamically active lower troposphere, with intense cyclones produced by barotropic instability. The same forcing, however, produces a less dynamically active upper troposphere, with much weaker circulation features. Thus although barotropic instability is a realistic mechanism for PV mixing and redistribution in the upper troposphere, it will not produce circulations comparable in magnitude to those produced in the lower troposphere.

6.1.4 Discussion of initial condition vs. forced experiments

The above results impose a very clear caveat on initial condition simulations. The zonally symmetric experiments led us to believe that barotropic instability could occur in a similar manner in the upper troposphere as in the lower troposphere. The forced experiments, however, tell a different story. One reason for this difference is that the

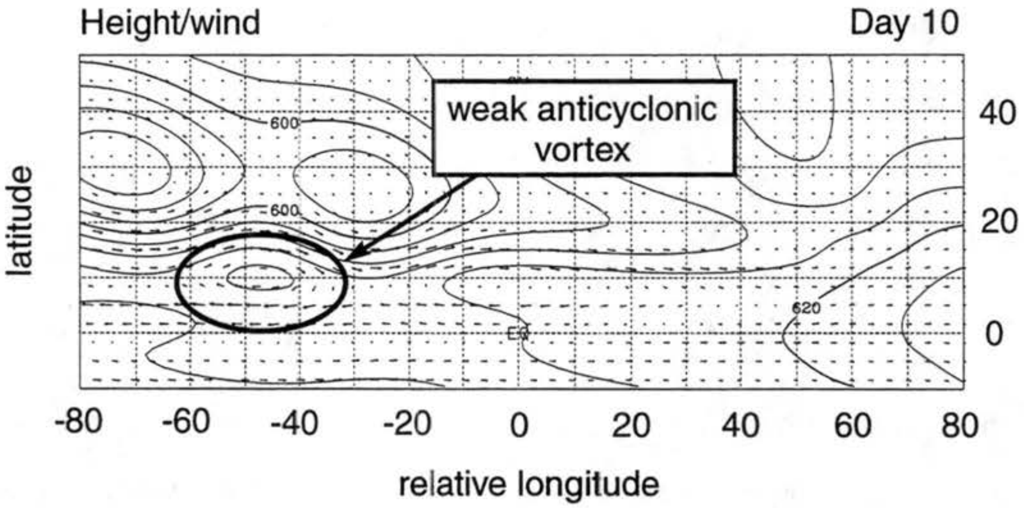

Figure 6.11: Height/wind field on Day 10 for the forced upper tropospheric ITCZ experiment.

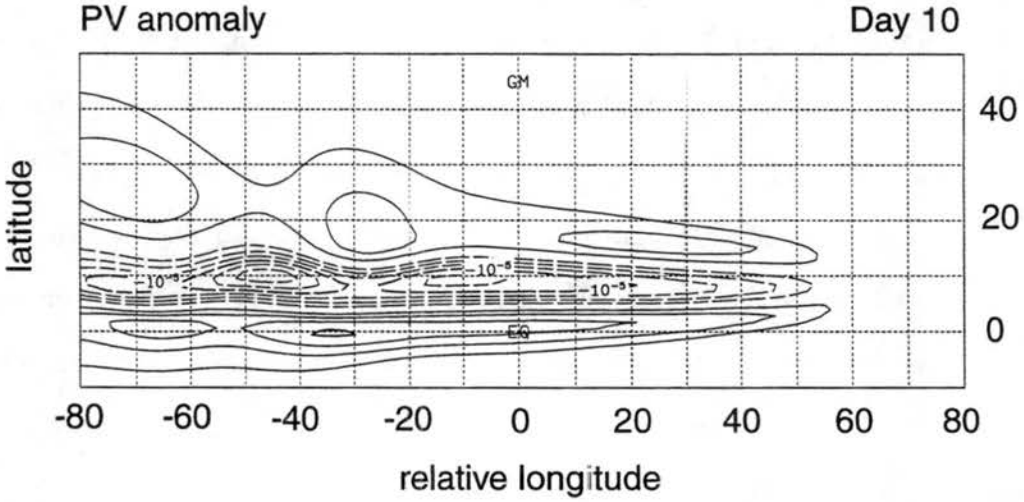

Figure 6.12: PV anomaly field on Day 10. Contour interval is 2.5×10^{-6} s^{-1}.

initial condition experiments prescribe an initial vorticity profile representative of a shear layer in the atmosphere, whereas the forced experiments let the forcing itself determine this vorticity profile. Because the mass source in the upper troposphere is inefficient at producing large PV anomalies, the vorticity profile prescibed in the initial condition experiment can never be reached by the forced simulation. The initial condition vorticity profile is perhaps unrealistic, then, since the forcing itself cannot produce it.

6.2 Application to the Western North Pacific monsoon trough

The barotropic instability simulations presented thus far have shown that the breakdown of a localized convective region in the lower troposphere is one possible explanation for the observed clustering of tropical cyclones in space and time. In addition, the simulations in Chapter 4 showed that the shape, location, and orientation of a convective region can have a large influence on the large-scale flow patterns in its vicinity. A natural question which then emerges from these two sets of experiments is whether the orientation of a barotropically unstable ITCZ region (which must be of a certain shape and in a certain location to be barotropically unstable) can affect the large-scale circulation so as to influence the tracks of the tropical cyclones generated by its breakdown. Lander (1996) provides observational evidence to motivate these simulations: he notes that tropical cyclones forming from convection in the Western North Pacific monsoon trough tend to more frequently follow northward or S-shaped tracks during episodes of a "reverse monsoon trough," when tropical convection is oriented from southwest to northeast. When the monsoon trough is in its "normal" orientation, from northwest to southeast, tropical cyclones tend to initially follow more northwestward tracks. We propose that these observations can be explained through the barotropic dynamics of the shallow water model.

6.2.1 Observations

The climatological summer monsoon trough in the Western North Pacific extends southeastward from east Asia (approximately 20°N, 110°E) past Guam to approximately 10°N, 150°E. In general, tropical disturbances which eventually evolve into tropical storms originate along the axis of this monsoon trough. The majority of these tropical cyclones move west-northwestward at low latitudes (south of 15°N), then either continue on a straight northwestward track or recurve to the east when they reach the midlatitude westerlies (Lander 1996).

Occasionally, however, the axis of the monsoon trough extends from southwest to northeast, in an opposite sense to the climatological trough orientation. This "reverse" orientation of the monsoon trough tends to recur approximately once per Northern summer, although in some years it is not seen at all and in others it occurs on several occasions. During instances of the reverse monsoon trough, 80% of tropical cyclones which form within the trough move on "northward" tracks (Lander 1996). Tracks which are classified as "northward" include several different types: 1) straight northward with little meandering; 2) eastward; and 3) S-shaped. In general, the tracks which are classified as northward stray far from the climatological track of west-northwest motion at low latitudes.

The 1994 typhoon season in the Western North Pacific saw repeated instances of a reverse monsoon trough. On 19 September 1994, as shown in Figure 6.13, convection is oriented from southwest to northeast, extending from 110° to 170°E. By 23 September, three tropical cyclones have formed from this monsoon trough: Orchid, Ruth, and Pat (Figure 6.14, from left to right). The tracks of these three tropical cyclones are plotted in Figure 6.15. All three storms move on northward or S-shaped tracks. Typhoon Orchid initially tracks eastward along the axis of the trough, then makes an abrupt turn to the north by 20 September, when Pat begins to organize into a tropical depression. Orchid then tracks to the northwest and then the northeast, forming an S-shaped track and intensifying to a supertyphoon by 25 September. Pat attains tropical storm status by 22 September,

Figure 6.13: GMS IR image of a reverse monsoon trough in the Western North Pacific on 19 September 1994.

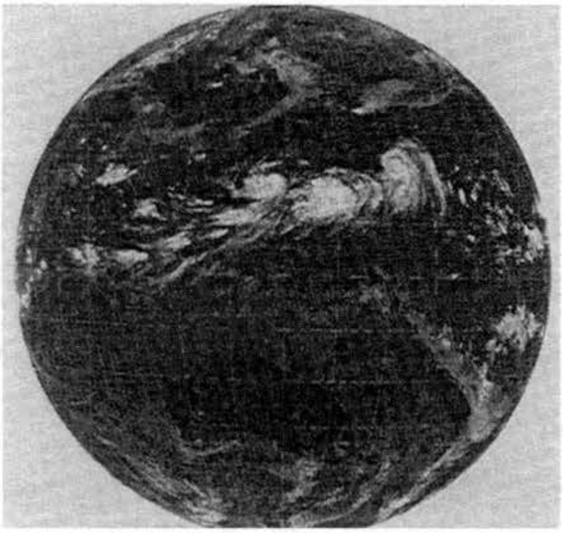

Figure 6.14: GMS IR image on 23 September 1994. Three tropical storms are visible: Orchid, Ruth, and Pat (from left to right).

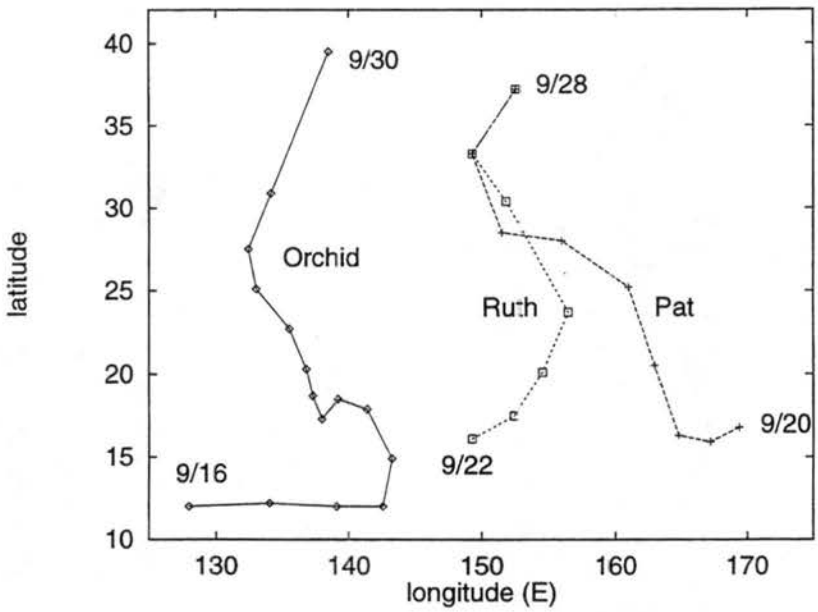

Figure 6.15: Joint Typhoon Warning Center best tracks of Supertyphoon Orchid, Tropical Storm Ruth, and Typhoon Pat in September 1994.

at the same time that Ruth is noted as a tropical depression. TS Pat initially moves on a north-northwestward track, and TD Ruth on a northeastward track. Ruth becomes a tropical storm on 24 September, at which time the two storms begin to interact. Ruth and Pat then become indistinguishable by 27 September.

6.2.2 Model results

Three shallow water simulations were run to test the hypothesis that the orientation of convection in the monsoon trough can influence the tracks of tropical cyclones. The model is forced by a mass sink, as in the forced barotropic instability simulations in Section 6.1.3. In each case, the forcing is the same zonally-elongated shape and size, approximately 48 degrees by 8 degrees, representing the approximate size and shape of summer monsoon convection in the Western North Pacific. The orientation of this forcing, however, differs between simulations. In the control simulation, the forcing is oriented straight east-west along 15°N, representing a zonally-elongated summer ITCZ structure. In the "normal"

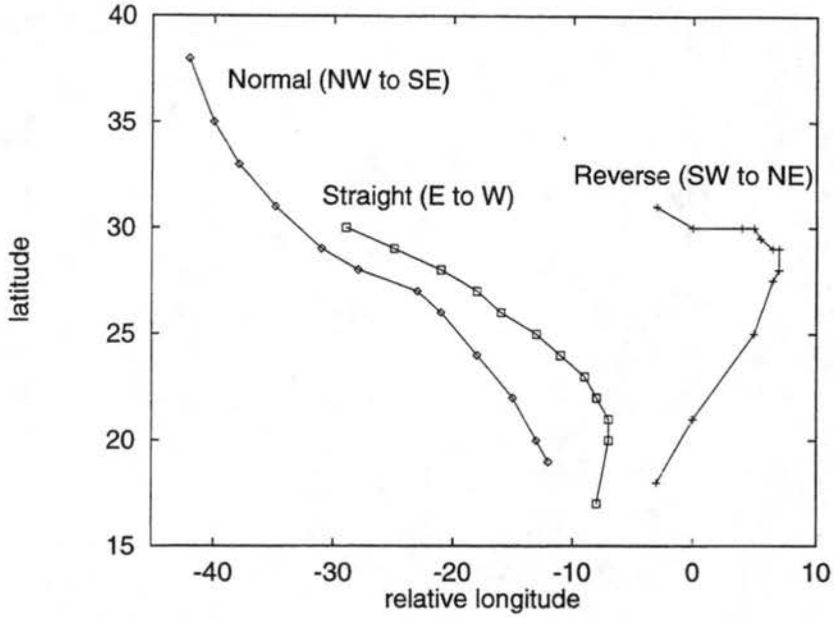

Figure 6.16: Tracks of cyclones in normal, east-west, and reverse monsoon trough experiments centered at 15°N. Points represent central location of model cyclones every 24 hours from Day 4 to Day 15.

monsoon trough simulation, the forcing is rotated 12° clockwise so that it extends from 20°N at its western end to 10°N at its eastern end. In the "reverse" monsoon trough simulation, the forcing is rotated in the opposite direction, 12° counterclockwise.

In each simulation, the forced monsoon trough becomes barotropically unstable and breaks down into one or more cyclonic vortices. The straight east-west forcing produces two cyclones, one slightly stronger than the other. The normally-oriented forcing also produces two cyclones, but one is significantly stronger than the other. The reverse monsoon trough rolls up into one dominant cyclone. In the normal and reverse trough simulations, the strongest cyclone is produced at the end of the forcing region which extends to the higher latitude.

The tracks of the cyclones in each simulation are presented in Figure 6.16. (The stronger of the two cyclones in both the east-west and normal trough simulations are plotted.) As the forcing is rotated counterclockwise from normal to straight to reverse, the amount of initial northeastward propagation of the cyclone increases. The normal trough cyclone tracks to the northwest only, while the straight trough cyclone initially tracks slightly northeastward, then turns to a northwestward track by Day 7. The reverse trough cyclone travels northeastward until Day 8, then drastically slows in speed as it turns north and then northwest. Finally, by Day 14, the track of the reverse trough cyclone begins to parallel the west-northwest tracks of the cyclones in the other two simulations.

The differences in the initial tracks of the cyclones result from differences in the preferential direction of Rossby wave energy dispersion from the forcing region. As in the convective shape simulations in Chapter 4, the circulation patterns to the west of the cyclones, produced by westward Rossby wave dispersion, are similar for all orientations of the monsoon trough. However, the energy dispersion to the east of the cyclones depends highly on the orientation of the forcing. When the forcing is oriented from northwest to southeast, in the "normal" manner, energy disperses preferentially to the northeast of the cyclone, producing a ridge which advects the cyclone to the northwest (Figure 6.17). A weak ridge initially forms to the southwest and tries to pull the cyclone to the northeast, which is manifest in the initially north-northwestward track. This ridge weakens and expands to the west after the forcing ends, and the track is finally determined only by the interaction between the cyclone and the strong ridge to its northeast. The northwestward drift of a cyclonic vortex caused by its interaction with the anticyclonic vortex it induces to its northeast by short Rossby wave dispersion is called β-drift.

In the case of the straight east-west monsoon trough, energy initially disperses slightly more strongly to the southeast than to the northeast (Figure 6.18). This energy dispersion induces a ridge to the southeast of the cyclone, which pushes the cyclone to the northeast. After the forcing ends, energy begins to preferentially disperse to the northeast, as in the normal monsoon trough simulation, and the cyclone's northwestward track approximately parallels that of normal trough cyclone.

The reverse-oriented monsoon trough initially disperses almost all of its short Rossby wave energy to the southeast, producing a strong ridge which advects the cyclone to the

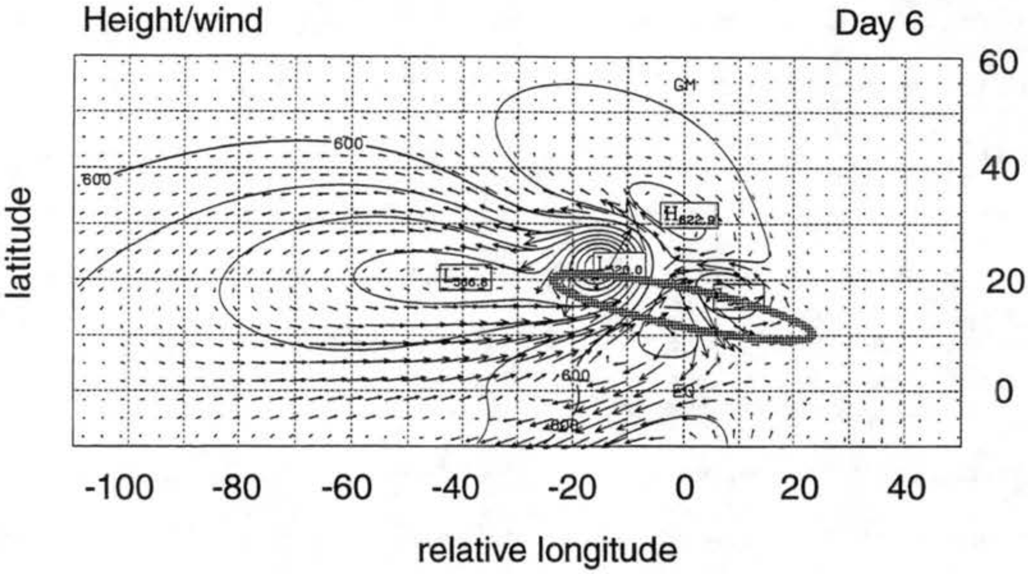

Figure 6.17: Height/wind field for the normal monsoon trough simulation centered at 15°N. Contour interval is 10 m. Vector winds are scaled such that a vector 10° in length represents a 10 m s^{-1} wind.

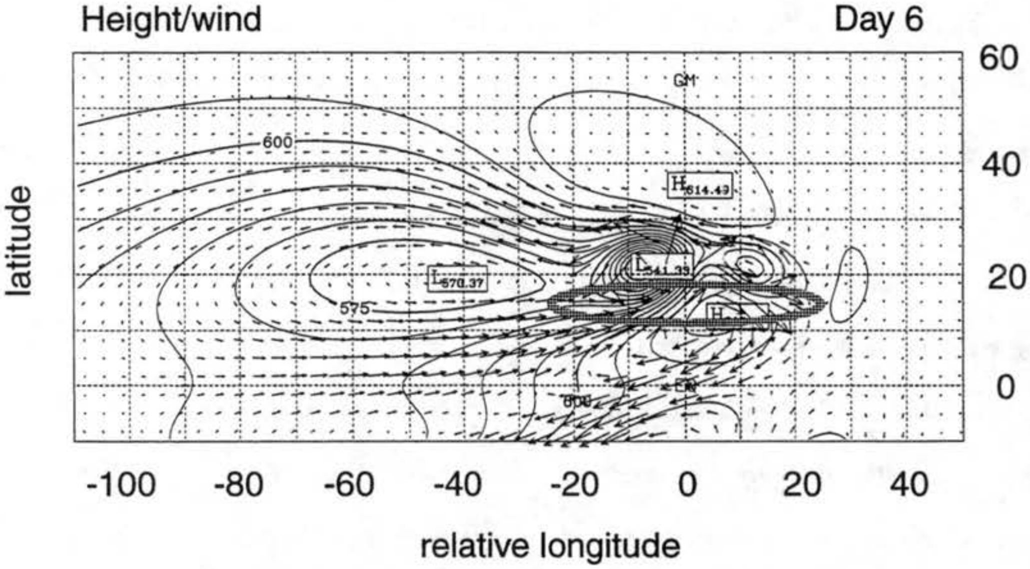

Figure 6.18: Height/wind field for the east-west monsoon trough simulation centered at 15°N. Height contour interval is 5 m.

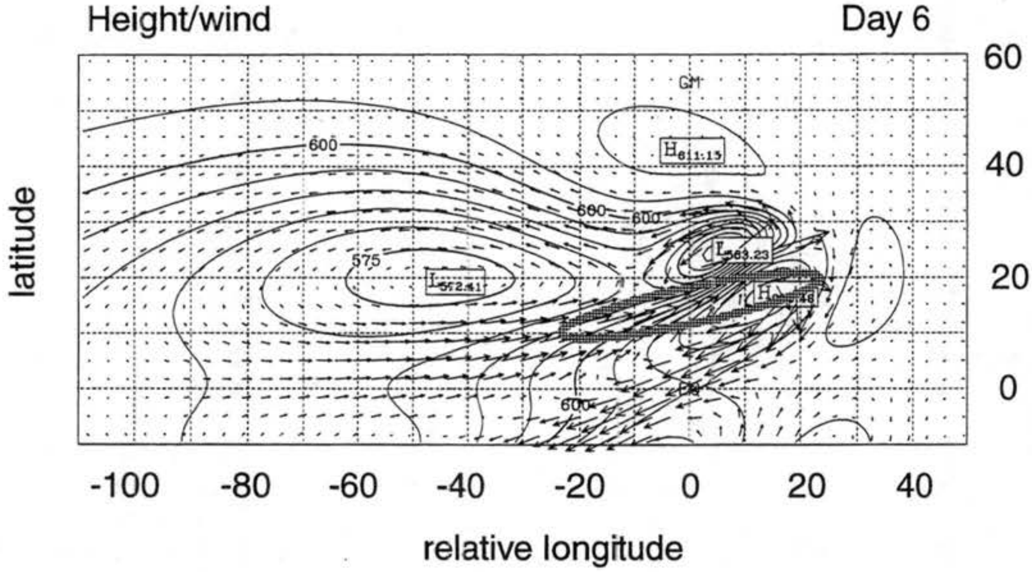

Figure 6.19: Height/wind field for the reverse monsoon trough simulation centered at 15°N. Height contour interval is 5 m.

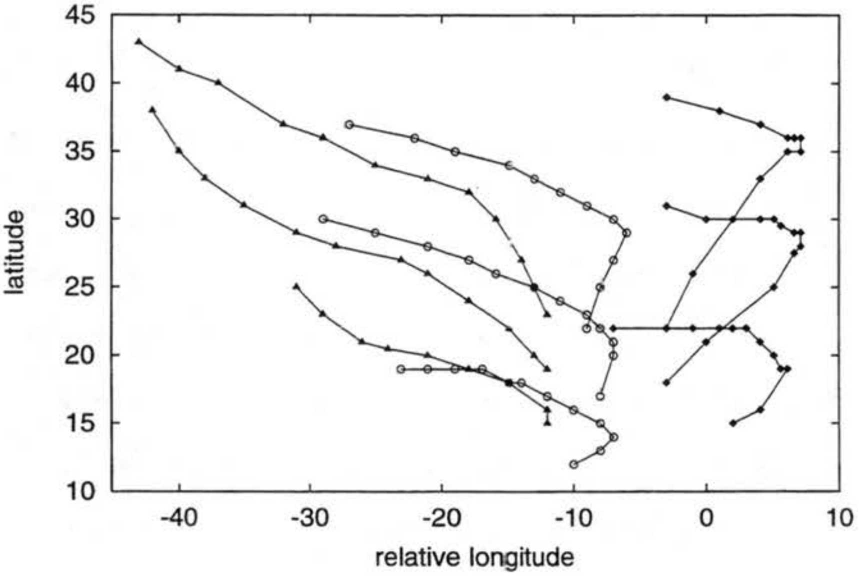

Figure 6.20: Tracks of cyclones produced by normal (triangles), east-west (circles), and reverse (diamonds) forcing at 10°, 15°, and 20°N. Points represent central location of model cyclones every 24 hours from Day 4 to Day 15.

northeast for 4 days (Figure 6.19). Carr et al. (1997) provide observational evidence for the existence of this ridge to the southeast of tropical cyclones oriented in a "reverse" manner. After the forcing in the model ends, the cyclone stalls between Days 8 and 12, as the ridge to its southeast erodes. The cyclone itself then begins to disperse energy to the northeast, and finally tracks to the northwest. Note that the track produced by the reverse monsoon trough cyclone could easily be extended into an "S-shaped" track if the model included midlatitude westerlies; this result corresponds nicely to Lander's observations of "S-shaped" tracks during episodes of the reverse monsoon trough.

Additional simulations illustrate that these results can be generalized to forcing at different latitudes. Figure 6.20 shows the tracks of cyclones produced when the monsoon trough forcing is centered at 10°, 15°, and 20°N for normal, east-west, and reverse-oriented troughs. The PV anomalies produced by the forcing depend on the latitude of the forcing, such that the higher latitude mass sink produces stronger PV anomalies, which then break down into more intense cyclones.

6.2.3 Other studies

Carr and Ellsberry (1995) and Carr et al. (1997) propose related mechanisms to explain sudden changes in tropical cyclone motion in the Western North Pacific. Occasionally, tropical cyclones which initially track to the northwest suddenly change direction and track almost straight northward, as in Typhoons Hal in September 1988 and Tip in September 1989. Carr and Ellsberry (1995) show through a nondivergent barotropic model simulation that such motions can be produced by the binary interaction between a tropical cyclone and a monsoon gyre. When these two features coalesce, a strong ridge forms to the southeast through Rossby wave dispersion and steers the entire system to the north.

Carr et al. (1997) propose that these northward-oriented track changes can be explained in a reverse monsoon trough situation by the coalescence of the peripheral anticyclones associated with two interacting tropical cyclones into a large ridge to the southeast of these cyclones. This ridge then steers at least the eastern cyclone in a more northward-oriented direction.

As these mechanisms were proposed to explain sudden tropical cyclone track changes, they assume that one or more tropical cyclones already exist before these steering influences become well-established. The forced shallow water model simulations presented here, on the other hand, provide a mechanism which simultaneously explains the generation of one or more tropical disturbances and predicts the large-scale flow features which direct their propagation. Both processes are simply a response of the atmosphere to the large-scale convective forcing in the Western North Pacific.

Chapter 7

SUMMARY AND CONCLUSIONS

The shallow water model simulations presented in this study have shown that the global atmospheric circulation is sensitive to both the horizontal and temporal distribution of tropical convective forcing. The horizontal shape, location, and orientation of the forcing determine the strength and stability of the response, the proportion of energy transferred into eastward- and westward-dispersing modes, and the exact direction of energy propagation. The timescale of the forcing determines the distribution of energy into Rossby, Kelvin, and gravity waves through a filtering of the wave spectrum.

In the upper troposphere, large-scale forcing which produces a barotropically stable response generally contains this response within a linear regime. Energy dispersion generates long Rossby waves to the west and short waves to the east of the forcing. When the forcing extends away from the Equator into higher latitudes, the response is significantly stronger than when the forcing is limited to low latitudes. This result is interpreted in terms of the potential vorticity conservation equation, which states that a mass source will produce larger PV anomalies where the ambient value of PV is higher.

The horizontal distribution of the forcing also influences the preferential direction of energy dispersion. When the forcing is meridionally elongated, more of the energy produced by the forcing is dispersed to the east in short Rossby waves. When the forcing is zonally elongated, the response is dominated by long Rossby waves which result from westward dispersion. This result is determined by the distribution of the vorticity forcing in spectral space. The wavenumber-frequency diagram for the divergent barotropic equations accurately predicts the strength of the westward- and eastward-dispersing modes based upon the spectral breakdown of the forcing.

In the lower troposphere, equal but opposite forcing to the upper tropospheric case produces a more complex response. Since the mass sink is more "efficient" in the lower troposphere, it generates larger PV anomalies and shifts the flow within the immediate vicinity of the forcing into a nonlinear regime. Very strong cyclonic vortices are produced in this region by the nonlinear flow, while the broad-scale response remains similar (but opposite in sign) to the upper tropospheric case. The comparison of the upper and lower tropospheric responses helps to explain why tropical convection produces strong low-level cyclonic vortices and broader, weaker upper-level anticyclones.

The response of the atmosphere to tropical convection of a specific shape and intensity also depends on the location of the convection with respect to the Equator. When the forcing is moved away from the Equator, a significant cross-equatorial flow is produced. Although the forcing may be located entirely within one hemisphere, the cross-equatorial divergent wind creates a Rossby wave source which produces an additional response in the opposite hemisphere. This response becomes even stronger, and the cross-equatorial flow longer-lasting, when the forcing is rotated such that its eastern end is poleward of its western end. The preferential direction of eastward Rossby wave dispersion is shown to be roughly perpendicular to the major axis of the elliptical forcing.

When the shape, location, and orientation of the model forcing are held fixed while the timescale is changed, the response of the atmosphere can also vary significantly. Forcing on a short timescale (e.g., 3 days) produces stronger Rossby and Kelvin wave responses than forcing on a long timescale (e.g., 18 days). The Rossby and Kelvin modes continue to become stronger as the timescale of the forcing decreases, until a certain timescale limit is reached and the gravity wave response becomes dominant.

The dominant modes of response for a given forcing timescale are shown to be predictable by considering the analytically-derived timescale filter. When the forcing timescale is long, most of the frequency spectrum is filtered out. Only the low zonal wavenumber Rossby waves with westward energy propagation remain. When the forcing timescale becomes shorter, less of the frequency spectrum is filtered, such that higher zonal wavenumber, eastward-dispersing Rossby waves can exist. For very short timescale forcing, the filter allows even the long gravity waves to be included in the response.

The results from the above experiments can be summarized in the context of the divergent barotropic wavenumber-frequency diagram. Forcing of a certain horizontal shape, size, location, and orientation corresponds to a specific weighting of the spectral coefficients, which localizes the response of the atmosphere to a certain region of the diagram. The timescale of convection then further modulates this response by filtering the wave modes in frequency. The final response in a barotropic atmosphere then depends on both the spatial and temporal distribution of the forcing.

In a continuously stratified atmosphere, the response becomes more complex. Since the response in a stratified atmosphere corresponds to the summation of the responses in all of the barotropic modes, the total response depends not only on the spatial and temporal characteristics of the forcing, but also on the weighting of each vertical mode. The timescale filter projects differently onto each vertical mode, such that the Rossby waves in one mode may be suppressed while those in another vertical mode may be allowed to exist at a large amplitude. The total response of the stratified atmosphere therefore depends not only on the horizontal and temporal distribution of the forcing, but also its vertical structure.

The barotropic atmosphere was then shown to exhibit a potential forced barotropic instability, both in the lower and upper troposphere. When the shallow water model is forced with an off-equatorial mass sink of low zonal and high meridional wavenumber, a reversed meridional gradient of PV is generated. Barotropic instability then occurs, producing a number of tropical cyclone-like vortices. The upper troposphere, however, only very weakly breaks down when it is subjected to the same forcing. The difference between the upper and lower troposphere is again due to the difference in the efficiency of the mass forcing in the shallow water model. From these simulations we conclude that tropical convection produces a much more dynamically active lower troposphere than upper troposphere, with significant PV mixing by barotropic instability.

This barotropic instability mechanism is then combined with the concepts from the earlier forcing shape experiments to propose a mechanism for the preponderance of northward and S-shaped tropical cyclone tracks during episodes of a "reverse monsoon trough" in the Western North Pacific. Off-equatorial convective forcing in the model leads to the creation of one or more tropical cyclone-like vortices by the unstable breakdown of the flow. These cyclones then propagate away from the forcing region in a direction which is shown to depend on the orientation of the forcing. When the forcing is oriented from northwest to southeast, as in a "normal" monsoon trough in the Western North Pacific, Rossby wave energy disperses preferentially to the northeast of the forcing, producing a ridge which advects the cyclones to the northwest. When the forcing is oriented from southwest to northeast, however, as in a "reverse" monsoon trough, Rossby wave energy disperses preferentially to the southeast. This produces a ridge to the southeast of the forcing and steers the cyclone to the northeast. These simulations provide a simple explanation for Lander's (1996) observation that the majority of tropical cyclones which form in a reverse monsoon trough in the Western North Pacific propagate in a northward direction.

From the simulations presented in this study, we conclude that the horizontal and temporal distribution of large-scale tropical convection can have a large effect on the response of the global circulation. Even though this study considered only the effects of idealized convective forcing on a model atmosphere with no vertical structure, no basic state winds, and no moist physics, the responses are still complex. Perhaps this study points to a need for a fuller understanding of the basic dynamics controlling the relationship between convection and circulation.

An obvious extension of this study would be to include the basic state winds in the forced simulations. Additionally, it would be interesting to construct some sort of simple feedback between the forcing and the wind fields to study the effect of equatorial waves on the production of new convection. Another extension of this work might be to force a linear baroclinic model with observed vertical profiles of tropical heating, then decompose the response into the different shallow water modes to determine which are dominant. The concepts developed in this present study would be applicable to any of these more complex topics.

REFERENCES

Ambrizzi, T., and B. J. Hoskins, 1995: Rossby wave propagation and teleconnection patterns in the austral winter. *J. Atmos. Sci.*, **52**, 3661–3672.

Bjerknes, J., 1969: Atmospheric teleconnections from the equatorial Pacific. *Mon. Wea. Rev.*, **97**, 163-172.

Blackmon, M. L., Y.-H. Lee, and J. M. Wallace, 1984: Horizontal structure of 500 mb height fluctuations with long, intermediate, and short time scales. *J. Atmos. Sci.*, **41**, 961–979.

Carr, L. E., M. A. Boothe, and R. L. Ellsberry, 1997: Observational evidence for alternate modes of track-altering binary tropical cyclone scenarios. *Mon. Wea. Rev.*, **125**, 2094–2111.

Carr, L. E., and R. L. Ellsberry, 1995: Monsoonal interactions leading to sudden tropical cyclone track changes. *Mon. Wea. Rev.*, **123**, 265–289.

Davidson, N. E., and H. H. Hendon, 1989: Downstream development in the Southern Hemisphere monsoon during FGGE/WMONEX. *Mon. Wea. Rev.*, **117**, 1458–1470.

Ferreira, R. N., and W. H. Schubert, 1997: Barotropic aspects of ITCZ breakdown. *J. Atmos. Sci.*, **54**, 261–285.

Ferreira, R. N., and W. H. Schubert, 1999: On the role of tropical cyclones in the formation of tropical upper tropospheric troughs. *J. Atmos. Sci.*, **56**, in press.

Ferreira, R. N., W. H. Schubert, and J. J. Hack, 1996: Dynamical aspects of twin tropical cyclones associated with the Madden-Julian Oscillation. *J. Atmos. Sci.*, **53**, 929–945.

Fulton, S. R., and W. H. Schubert, 1985: Vertical normal mode transforms: theory and application. *Mon. Wea. Rev.*, **113**, 647–658.

Gill, A. E., 1980: Some simple solutions for heat-induced tropical circulation. *Quart. J. Roy. Meteor. Soc.*, **106**, 447–462.

Gill, A. E., 1982: *Atmosphere-Ocean Dynamics.* Academic Press, 662 pp.

Hack, J. J., and R. Jakob, 1992: Description of a global shallow water model based on the transform method. NCAR Tech. Note NCAR/TN-343+STR, 39 pp. [Available from Climate and Global Dynamics Division, NCAR, P.O. Box 3000, Boulder, CO 80307.]

Hack, J. J., W. H. Schubert, D. E. Stevens, and H.-C. Kuo, 1989: Response of the Hadley circulation to convective forcing in the ITCZ. *J. Atmos. Sci.*, **46**, 2957–2973.

Horel, J. D., and J. M. Wallace, 1981: Planetary-scale atmospheric phenomena associated with the Southern Oscillation. *Mon. Wea. Rev.*, **109**, 813–829.

Kiladis, G. N., 1998: Observations of Rossby waves linked to convection over the eastern tropical Pacific. *J. Atmos. Sci.*, **55**, 321-339.

Kiladis, G. N., G. A. Meehl, and K. M. Weickmann, 1994: Large-scale circulation associated with westerly wind bursts and deep convection over the western equatorial Pacific. *J. Geophys. Res.*, **99**, 18,527–18,544.

Kiladis, G. N., and K. M. Weickmann, 1992: Circulation anomalies associated with tropical convection during Northern winter. *Mon. Wea. Rev.*, **120**, 1900–1923.

Kiladis, G. N., and K. M. Weickmann, 1997: Horizontal structure and seasonality of large-scale circulations associated with submonthly tropical convection. *Mon. Wea. Rev.*, **125**, 1997–2013.

Knutson, T. R., and K. M. Weickmann, 1987: 30–60 day atmospheric oscillations: Composite life cycles of convection and circulation anomalies. *Mon. Wea. Rev.*, **115**, 1407–1436.

Kuo, H. L., 1973: Dynamics of quasigeostrophic flows and instability theory. *Adv. Appl. Mech.*, **13**, 247-330.

Lander, M. A., 1996: Specific tropical cyclone track types and unusual tropical cyclone motions associated with a reverse-oriented monsoon trough in the Western North Pacific. *Wea. Forecasting*, **11**, 170–186.

Lau, K.-M., and H. Lim, 1984: On the dynamics of equatorial forcing of climate teleconnections. *J. Atmos. Sci.*, **41**, 161–176.

Lau, K.-M., and L. Peng, 1987: Origin of low-frequency (intraseasonal) oscillations in the tropical atmosphere. Part I: Basic theory. *J. Atmos. Sci.*, **44**, 950–972.

Lau, K.-M., and T. J. Phillips, 1986: Coherent fluctuations of extratropical geopotential height and tropical convection on intraseasonal time scales. *J. Atmos. Sci.*, **43**, 1164–1181.

Lim, H., and C.-P. Chang, 1983: Dynamics of teleconnections and Walker circulations forced by equatorial heating. *J. Atmos. Sci.*, **40**, 1897–1915.

Lin, X., and R. H. Johnson, 1996: Heating, moistening, and rainfall over the Western Pacific Warm Pool during TOGA COARE. *J. Atmos. Sci.*, **53**, 3367–3383.

Matsuno, T., 1966: Quasi-geostrophic motions in the equatorial area. *J. Meteor. Soc. Japan*, **44**, 25–42.

Meehl, G. A., G. N. Kiladis, K. M. Weickmann, M. Wheeler, D. S. Gutzler, and G. P. Compo, 1996: Modulation of equatorial subseasonal convective episodes by tropical-extratropical interaction in the Indian and Pacific Ocean regions. *J. Geophys. Res.*, **101**, 15,033–15,049.

Molinari, J., D. Knight, M. Dickinson, D. Vollaro, and S. Skubis, 1997: Potential vorticity, easterly waves, and Eastern Pacific tropical cyclogenesis. *Mon. Wea. Rev.*, **125**, 2699–2708.

Nitta, T., 1987: Convective activities in the tropical Western Pacific and their impact on the Northern Hemisphere summer circulation. *J. Meteor. Soc. Japan*, **65**, 373-390.

Nogues-Paegle, J., and K. C. Mo, 1988: Transient response of the Southern Hemisphere subtropical jet to tropical forcing. *J. Atmos. Sci.*, **45**, 1493–1508.

Ripa, P., 1983: General stability conditions for zonal flows in a one-layer model on the β-plane or the sphere. *J. Fluid Mech.*, **126**, 463–489.

Sardeshmukh, P. D., and B. J. Hoskins, 1988: The generation of global rotational flow by steady idealized tropical divergence. *J. Atmos. Sci.*, **45**, 1228–1251.

Silva Dias, P. L., W. H. Schubert, and M. DeMaria, 1983: Large-scale response of the tropical atmosphere to transient convection. *J. Atmos. Sci.*, **40**, 2689–2707.

Simmons, A. J., J. M. Wallace, and G. W. Branstator, 1983: Barotropic wave propagation and instability, and atmospheric teleconnection patterns. *J. Atmos. Sci.*, **40**, 1363–1392.

Swatztrauber, P. N., and A. Kasahara, 1985: The vector harmonic analysis of Laplace's tidal equations. *SIAM J. Sci. Stat. Comput.*, **6**, 464–491.

Tyrrell, G. C., D. J. Karoly, and J. L. McBride, 1996: Links between tropical convection and variations of the extratropical circulation during TOGA COARE. *J. Atmos. Sci.*, **53**, 2735–2748.

Vincent, D. G., K.-C. Ko, and J. M. Schrage, 1997: Subtropical jet streaks over the South Pacific. *Mon. Wea. Rev.*, **125**, 438–447.

Wallace, J. M., and D. S. Gutzler, 1981: Teleconnections in the geopotential height field during the Northern Hemisphere winter. *Mon. Wea. Rev.*, **109**, 784–812.

Wang, W., and M. E. Schlesinger, 1999: The dependence on convection parameterization of the tropical intraseasonal oscillation simulated by the UIUC 11-layer atmospheric GCM. Submitted to *J. Climate*.

Webster, P. J., and H.-R. Chang, 1988: Equatorial energy accumulation and emanation regions: Impacts of a zonally varying basic state. *J. Atmos. Sci.*, **45**, 803–829.

Wheeler, M., and G. N. Kiladis, 1999: Convectively-coupled equatorial waves: Analysis of clouds and temperature in the wavenumber-frequency domain. Submitted to *J. Atmos. Sci.*

Yanai, M., B. Chen, and W. Tung, 1999: The Madden-Julian Oscillation (MJO) observed during the TOGA-COARE IOP: Global view. Submitted to *J. Atmos. Sci.*

Yanai, M., J.-H. Chu, T. E. Stark, and T. Nitta, 1976: Response of deep and shallow tropical maritime cumuli to large-scale processes. *J. Atmos. Sci.*, **33**, 976–991.

Zhang, C., and P. J. Webster, 1989: Effects of zonal flows on equatorially trapped waves. *J. Atmos. Sci.*, **46**, 3632–3652.

APPENDIX A

ANALYTICAL SOLUTION TO THE DIVERGENT BAROTROPIC ABSOLUTE VORTICITY EQUATION

The equation for the conservation of absolute vorticity, η, in a shallow water system is:

$$\frac{\partial\eta}{\partial t} + \frac{\partial(\eta u)}{a\cos\phi\partial\lambda} + \frac{\partial(\eta v\cos\phi)}{a\cos\phi\partial\phi} = 0. \tag{A.1}$$

An alternate form of this equation is:

$$\frac{\partial}{\partial t}(\nabla^2\psi) + u\frac{\partial}{a\cos\phi\partial\lambda}(\nabla^2\psi) + v\frac{\partial}{a\partial\phi}(2\Omega\sin\phi + \nabla^2\psi) + \eta\delta = 0, \tag{A.2}$$

where the definitions of absolute vorticity and divergence have been used:

$$\eta = 2\Omega\sin\phi + \nabla^2\psi, \tag{A.3}$$

$$\delta = \frac{\partial u}{a\cos\phi\partial\lambda} + \frac{\partial(v\cos\phi)}{a\cos\phi\partial\phi}. \tag{A.4}$$

This equation will be analytically solvable in spectral space if several simplifying assumptions are made. The first simplification involves the continuity equation, given here in full form:

$$\frac{\partial h'}{\partial t} + \frac{\partial(h'u)}{a\cos\phi\partial\lambda} + \frac{\partial(h'v\cos\phi)}{a\cos\phi\partial\phi} + H\delta = Q(\lambda,\mu,t), \tag{A.5}$$

where h' is the deviation of the fluid depth from H, the global mean depth. The mass source/sink Q is defined as the product of separable functions of space and time, as in the divergent model:

$$Q(\lambda,\mu,t) = \tilde{h}(\lambda,\mu)\tfrac{1}{2}\alpha^3t^2e^{-\alpha t}. \tag{A.6}$$

Now suppose that (A.5) can be approximated by the simplified form:

$$H\delta = Q(\lambda, \mu, t). \tag{A.7}$$

When the continuity equation is approximated by (A.7), equation (A.2) simplifies to:

$$\frac{\partial}{\partial t}(\nabla^2\psi) + u\frac{\partial}{a\cos\phi\partial\lambda}(\nabla^2\psi) + v\frac{\partial}{a\partial\phi}(2\Omega\sin\phi + \nabla^2\psi) = -\frac{\eta\tilde{h}}{H}\tfrac{1}{2}\alpha^3t^2e^{-\alpha t}. \tag{A.8}$$

The flow is then linearized about a basic zonal flow $\bar{u}$, which is dependent only on latitude:

$$\bar{u}(\phi) = \bar{\omega}a\cos\phi, \tag{A.9}$$

where $\bar{\omega}$ is a constant. Equation (A.8) can then be rewritten as:

$$\frac{\partial}{\partial t}(\nabla^2\psi) + \bar{\omega}\frac{\partial}{\partial\lambda}(\nabla^2\psi) + \frac{2\Omega v\cos\phi}{a} = -\frac{2\Omega\sin\phi\tilde{h}}{H}\tfrac{1}{2}\alpha^3t^2e^{-\alpha t}. \tag{A.10}$$

In order for this equation to be analytically solvable in terms of ψ, a further assumption is invoked, that of nondivergence. This allows the velocity component v to be rewritten in terms of ψ:

$$v\cos\phi = \frac{\partial\psi}{a\partial\lambda}. \tag{A.11}$$

The vorticity equation can then be expressed entirely in terms of the nondivergent streamfunction:

$$\frac{\partial}{\partial t}(\nabla^2\psi) + \bar{\omega}\frac{\partial}{\partial\lambda}(\nabla^2\psi) + \frac{2\Omega}{a^2}\frac{\partial\psi}{\partial\lambda} = -\frac{2\Omega\mu\tilde{h}}{H}\tfrac{1}{2}\alpha^3t^2e^{-\alpha t}. \tag{A.12}$$

The above equation is then transformed into spectral space. Each term in (A.12) is multiplied by $Y_n^{m*}(\lambda,\mu)$, the complex conjugate spherical harmonic function, defined by:

$$Y_n^{m*}(\lambda,\mu) = P_n^m(\mu)e^{-im\lambda}, \tag{A.13}$$

where $P_n^m(\mu)$ is the associated Legendre polynomial. This equation is then integrated over the sphere in λ and μ:

$$\begin{aligned}\frac{\partial}{\partial t}\int_{-1}^{1}\int_{0}^{2\pi}(\nabla^2\psi)Y_n^{m*}d\lambda d\mu \quad &+ \quad \bar{\omega}\int_{-1}^{1}\int_{0}^{2\pi}\frac{\partial}{\partial\lambda}(\nabla^2\psi)Y_n^{m*}d\lambda d\mu + \frac{2\Omega}{a^2}\int_{-1}^{1}\int_{0}^{2\pi}\frac{\partial\psi}{\partial\lambda}Y_n^{m*}d\lambda d\mu \\ &= \quad -\tfrac{1}{2}\alpha^3t^2e^{-\alpha t}\int_{-1}^{1}\int_{0}^{2\pi}\frac{2\Omega\mu\tilde{h}}{H}Y_n^{m*}d\lambda d\mu. \end{aligned} \tag{A.14}$$

To simplify, the spatial derivatives in the above equation are shifted from ψ onto the spherical harmonic functions, since these functions are easily differentiable. Integrating the second and third terms in (A.14) by parts and using the general relation:

$$\iint F\nabla^2 G d\lambda d\mu = \iint G\nabla^2 F d\lambda d\mu, \tag{A.15}$$

equation (A.14) becomes:

$$\begin{aligned} \frac{\partial}{\partial t}\iint \psi\nabla^2 Y_n^{m*} d\lambda d\mu \quad &- \quad \bar{\omega}\iint \psi\nabla^2\left(\frac{\partial Y_n^{m*}}{\partial\lambda}\right) d\lambda d\mu - \frac{2\Omega}{a^2}\iint \psi\frac{\partial Y_n^{m*}}{\partial\lambda} d\lambda d\mu \\ &= \quad -\tfrac{1}{2}\alpha^3 t^2 e^{-\alpha t}\iint S(\lambda,\mu) Y_n^{m*} d\lambda d\mu, \end{aligned} \tag{A.16}$$

where $S(\lambda,\mu)$ is defined as:

$$S(\lambda,\mu) = \frac{2\Omega\mu\tilde{h}(\lambda,\mu)}{H}, \tag{A.17}$$

and the limits of integration have been dropped for convenience.

Since the spherical harmonic functions Y_n^{m*} are composed of separable functions of longitude and latitude, they can be easily differentiated:

$$\frac{\partial Y_n^{m*}}{\partial\lambda} = -imY_n^{m*}, \tag{A.18}$$

$$\nabla^2 Y_n^{m*} = -\frac{n(n+1)}{a^2} Y_n^{m*}. \tag{A.19}$$

Substituting these definitions into (A.16), and then simplifying by using the general definition of a spherical harmonic transform:

$$A_n^m(t) = \tfrac{1}{4\pi}\iint A(\lambda,\mu,t) Y_n^{m*}(\lambda,\mu) d\lambda d\mu, \tag{A.20}$$

the spectral space representation of the nondivergent, linearized vorticity equation can be written as:

$$\frac{d\psi_n^m(t)}{dt} - im\left[\frac{2\Omega}{n(n+1)} - \bar{\omega}\right]\psi_n^m(t) = S_n^m\frac{a^2}{n(n+1)}\tfrac{1}{2}\alpha^3 t^2 e^{-\alpha t}. \tag{A.21}$$

Now define a spectral frequency, ν_n^m:

$$\nu_n^m = m\left[\frac{2\Omega}{n(n+1)} - \bar{\omega}\right], \tag{A.22}$$

such that (A.21) can be rewritten as:

$$\frac{d\psi_n^m(t)}{dt} - i\nu_n^m \psi_n^m(t) = S_n^m \frac{a^2}{n(n+1)} \tfrac{1}{2}\alpha^3 t^2 e^{-\alpha t}. \tag{A.23}$$

To solve this equation, first multiply through by $e^{-i\nu_n^m t}$ and rearrange:

$$\frac{d}{dt}\{\psi e^{-i\nu_n^m t}\} = S_n^m \frac{a^2}{n(n+1)} \tfrac{1}{2}\alpha^3 t^2 e^{-(\alpha + i\nu_n^m)t}. \tag{A.24}$$

Now integrate from 0 to t:

$$\int_0^t \frac{d}{dt'}\{\psi e^{-i\nu_n^m t'}\} dt' = \int_0^t S_n^m \frac{a^2}{n(n+1)} \tfrac{1}{2}\alpha^3 (t')^2 e^{-(\alpha + i\nu_n^m)t'} dt'. \tag{A.25}$$

Integrating the right hand side by parts twice, and assuming that $\psi(0) = 0$, we arrive at the final solution for $\psi_n^m(t)$:

$$\psi_n^m(t) = \frac{\alpha^3}{(\alpha + i\nu_n^m)^3} S_n^m \frac{a^2}{n(n+1)} e^{i\nu_n^m t}\{1 - [1 + (\alpha + i\nu_n^m)t + \tfrac{1}{2}(\alpha + i\nu_n^m)^2 t^2] e^{-(\alpha + i\nu_n^m)t}\}. \tag{A.26}$$

The final solution $\psi_n^m(t)$ can be calculated at any time t from (A.26) with the knowledge of only three parameters: S_n^m, α, and $\bar{\omega}$. The solution in spectral space can then be transformed back into physical space by the following transform:

$$\psi(\lambda, \mu, t) = \sum_{m=-M}^{M} \sum_{n=|m|}^{M} \psi_n^m(t) P_n^m(\mu) e^{im\lambda}. \tag{A.27}$$